Defect Localization and Modulation Indices Separation in Aluminum Structures using Vibro-Acoustic Modulation

Dissertation (monograph) approved by

the Doctoral Degree Committee of
Hamburg University of Technology
in pursuit of the academic degree of

Doktor-Ingenieur (Dr.-Ing.)

written by
Mohammad M. Bazrafkan

from
Shiraz, Iran

2026

List of reviewers:
Prof. Dr.-Ing habil. Marcus Rutner
Prof. Dr. rer. nat. habil. Norbert Hoffmann

Date of oral examination:
29.04.2026

DOI: https://doi.org/10.15480/882.17170

ORCID: Mohammad M. Bazrafkan
https://orcid.org/0009-0003-7774-0664

HAMBURG UNIVERSITY OF TECHNOLOGY

Abstract

Defect Localization and Modulation Indices Separation in Aluminum Structures using Vibro-Acoustic Modulation

by Mohammad Bazrafkan

This study addresses two significant and interconnected challenges: (1) enhancing the mathematical description of the Vibro-Acoustic Modulation (VAM) response in order to separate modulation indices (MIs), and (2) developing a robust, baseline-free, and experimentally validated method for the localization of real cracks in plate-like aluminum structures. By combining theoretical formulations, simulation models, and experimental validation, this dissertation advances understanding and practical application of VAM techniques for damage detection and localization.

In the first part of the study, the limitations of conventional methods for MI estimation, such as Hilbert Transform (HT) and Sweeping Phase Homodyne Separation (SPHS), are examined in the context of real-world applications where the presence of a Non-Modulated Carrier (NMC) signal and environmental noise can significantly affect measurement accuracy.

To overcome these limitations, an analytical framework is proposed that models nonlinear signal interaction using multiple modulation types. The amplitude-frequency-phase modulation (AFPM) model is being introduced and analyzed for the first time in this dissertation. The AFPM model theoretically shows that the phase shifts of different frequency components in the VAM response change with variations in MIs. Furthermore, the relative sensitivity analysis of phase shifts and the damage modulation index (DMI) theoretically indicates that phase shifts are more sensitive to changes in MIs than the DMI. Despite the potential for early damage detection via phase shifts, small amplitude or phase changes can be masked by noise or measurement errors.

Subsequently, MI separation algorithms based on the ratios of the amplitudes and powers of the first and second sidebands are introduced and validated via numerical simulations in MATLAB. Experimental validation is conducted using aluminum specimens under controlled fatigue loading, with piezoelectric actuators and sensors to measure system response. The experimental results also revealed changes in the phase shifts of the frequency components, as predicted by the AFPM model. Additionally, comparing the slopes of changes in the DMI and phase shift curves shows that at some frequencies, the phase shift curve reveals changes earlier than the DMI curve. The findings demonstrate that incorporating phase variation analysis can enhance sensitivity to structural changes, often revealing variations more prominently than an amplitude-based approach alone.

The second part of the thesis addresses the challenge of crack localization. Traditional localization methods often rely on baseline signals (especially in Lamb wave localization) and dense sensor arrays, which limit practical deployment (dense sensor arrays require complex hardware). In contrast, this work presents a novel short-time VAM-based localization algorithm that does not require a baseline measurement, enabling localization with the minimum number of required receivers. Theoretically, at least three receivers are required for signal source localization.

The method utilizes the simultaneous excitation of a continuous, low-frequency (LF) S0-mode Lamb wave and a tone-burst, high-frequency (HF) A0-mode Lamb wave. The interaction of these two signals at the defect site generates modulation sidebands. The first upper sideband, at $\omega + \Omega$, is used for crack localization due to its higher amplitude than the other sideband frequencies. The sideband signal is then extracted using Short-Time Fourier Transform (STFT) and mapped spatially through a Delay-and-Sum (DAS) damage imaging method.

The experimental setup for localization consists of aluminum plates with fatigue-induced cracks, piezoelectric actuators for high- and low-frequency excitation, and four piezoelectric sensors as receivers. Experimental results demonstrate that the nonlinear sideband generated by the crack exhibits directional scattering, behaving as a new wave source. This property allows localization of the crack, even when it is positioned outside the sensor array, by tracking the time-domain evolution of the sideband amplitude. The influence of tone burst duration is also investigated, revealing that durations as short as 50 μs are sufficient for accurate localization. Longer durations may enhance image intensity but may reduce spatial resolution by identifying a wider area as the likely location of the defect due to increased signal overlap. Importantly, the method proves effective regardless of whether the sensor arrangement is symmetric or asymmetric, thereby increasing its practical applicability. The proposed method is demonstrated to produce highly accurate and repeatable localization results across various sensor configurations and signal durations. These results confirm the possibility of baseline-free defect localization using minimal sensors in real-world conditions.

Keywords:
Vibro-Acoustic Modulation (VAM), Modulation Indices (MIs), Amplitude-Frequency-Phase Modulation (AFPM), Crack Detection, Short-Time Fourier Transform (STFT), Delay-and-Sum (DAS), Structural Health Monitoring (SHM), Nonlinear Ultrasonics, Lamb Waves, Defect Localization, Baseline-Free Methods.

Table of Contents

List of acronyms

AFM	amplitude-frequency modulation
AFPM	amplitude-frequency-phase modulation
AMI	amplitude modulation index
DAS	delay and sum
DI	dagame index
FFT	fast Fourier transform
FMI	frequency modulation Index
HF	high frequency
HHT	Hilbert-Huang transform
HT	Hilbert transform
IQHS	in-phase quadrature homodyne separation
LF	low frequency
NDE	nondestructive evaluation
NMC	non-modulated carrier
PMI	phase modulation index
SA	sideband amplitude
SHM	structure health monitoring
STFT	short-time Fourier transform
SUT	structure under test
TOF	time of flight
VAM	vibro-acoustic modulation

List of symbols

Ω	low-frequency (angular)	*rad/s*
f_Ω	low-frequency	*Hz*
ω	high-frequency (angular)	*rad/s*
f_ω	high-frequency	*Hz*
X_Ω	low-frequency signal (probe signal)	
X_ω	high-frequency signal (pump signal)	
A_Ω	amplitude of the low-frequency signal	
A_ω	amplitude of the high-frequency signal	
$2h$	thickness of a plate	*mm*
c_L	longitudinal wave speed	*mm/s*
c_T	shear wave speed	*mm/s*
c_g	group velocity	*mm/s*
m_a	amplitude modulation index	
m_f	frequency modulation index	
m_p	phase modulation index	
ϕ_ω	initial phase shift of the high-frequency signal	*rad*
ϕ_Ω	initial phase shift of the low-frequency signal	*rad*
$J_n(x)$	the Bessel functions of the first kind	

Chapter 1

Introduction and literature review

1.1 Problem Statement

Vibro-Acoustic Modulation (VAM) has evolved into a powerful and effective technique in nondestructive evaluation (NDE), particularly for detecting and characterizing defects in metallic structures [1, 2]. Traditional ultrasonic methods rely on linear wave propagation; however, once a crack or other nonlinearity is introduced, new phenomena such as wave modulation, higher harmonic generation, and sidebands become detectable [1, 3]. In the context of metal-based components widely used in civil infrastructure, early detection and accurate localization of cracks and other defects are crucial to ensure structural integrity and enhance long-term performance [4, 5]. Consequently, methods that are robust, economical, and capable of enhancing component lifetime while quickly evaluating their condition and reducing resource consumption and test time are needed.

A key advantage of VAM lies in its ability to exploit both high-frequency (HF) and low-frequency (LF) excitations. A defect induces modulation effects that are absent or negligible in pristine materials [1, 3, 6]. The HF signal is modulated by the LF signal, which can be detected through signal processing techniques such as the Fast Fourier Transform (FFT) or time-frequency analysis, including the short-time Fourier transform (STFT) [7, 8]. These modulated features, especially sidebands around the carrier frequency, offer highly sensitive indicators of structural nonlinearity. However, capturing subtle variations and isolating the modulation index (MI) from measurement noise remains challenging, especially in complex geometries or in weakly coupled systems [9].

In defect detection, some researchers have focused on establishing relationships between modulation parameters and defect size [2, 10]. One area of active investigation involves defining dimensionless parameters linking crack growth to sample lifetime, enabling prognostic estimation of structural health [11]. Building on foundational work by Donskoy et al. [1, 3] and further developed by researchers like Klepka and Staszewski [2, 9], modern approaches are advancing models that account for amplitude, frequency, and phase modulation simultaneously. By modeling these combined modulation effects, researchers aim for more precise parameter estimation to quantify crack size and growth rates [12, 13].

Despite progress in detection, defect localization remains critical for practical application. Guided wave methods, particularly Lamb waves, have been integrated with the VAM technique to improve localization capabilities [4, 5, 14]. Lamb waves can propagate over long distances in plate-like structures with relatively low attenuation, but their multimodal nature (A_n and S_n modes) introduces complexity in signal interpretation [4, 14]. Methods such as Delay-and-Sum (DAS) damage imaging have been adapted for use with VAM, providing a method to reconstruct spatial maps of nonlinear sources [15, 16]. By analyzing arrival times and amplitudes of modulated components across multiple sensors, DAS algorithms can pinpoint defect locations with high accuracy[1]. For a baseline-required method, environmental changes, boundary conditions, and material variability can mask or mimic defect signatures, thereby complicating the reliable detection of defects [8, 10]. A baseline-free method is highly desirable for in situ monitoring, where recalibration is impractical.

Sensor arrangement remains a practical consideration for real-world applications. Industries often seek to minimize added weight and complexity. Strategies involving multifunctional sensors or minimal sensor arrays can lower costs and structural modifications while maintaining diagnostic capability [9, 17].

In summary, this thesis addresses the development and validation of advanced Vibro-Acoustic Modulation (VAM) techniques for detecting and localizing defects in aluminum structures. The research aims to:

- Enhance existing modulated signal models to incorporate simultaneous amplitude, frequency, and phase modulation.
- Develop algorithms for separating modulation indices and signal phase shifts.
- Investigate the capability of these parameters in the early-stage damage detection.
- Integrate advanced guided wave techniques (Lamb waves) and the DAS damage imaging method for baseline-free, high-accuracy defect localization, using the short-time VAM technique.
- Demonstrate practical solutions using minimal sensor arrays as well as different sensor arrangements suitable for field applications.
- Experimental validation of algorithms using non-complex structures.

Through these objectives, this thesis aims to close existing gaps in NDE and structural health monitoring, delivering practical tools for industries that rely on the integrity of metallic structures. Expected outcomes include an experimentally validated modeling framework and localization techniques suitable for real-world applications.

1.2 Motivation

Ensuring the integrity and safety of structures remains a vital concern in modern engineering, particularly in sectors where failure can result in severe economic losses or risk to human life, such as aerospace, civil infrastructure, and energy systems [18, 19]. Structural health monitoring (SHM) has therefore become an essential discipline, providing methods for detecting damage before it progresses to a critical state. However, conventional SHM techniques, including linear ultrasonic inspection and vibration analysis, often need baseline measurements and struggle to identify early-stage or nonlinear defects [1, 20].

Vibro-acoustic modulation (VAM) offers a compelling alternative due to its ability to exploit the nonlinear response of damaged materials. This technique involves the interaction between a low-frequency vibration and a high-frequency ultrasonic wave, generating modulation sidebands that act as sensitive indicators of contact-type or closed cracks [1, 21]. Unlike purely linear methods, VAM does not always require a reference state, making it more practical in field conditions where baseline data may be unavailable or unreliable. Recent

---

[1] See subsection 1.3.2

experimental research has demonstrated the feasibility of combining VAM with guided waves for enhanced detection and localization performance [22-24].

Despite its promise, VAM still faces important limitations. Accurately quantifying crack severity from modulation indices remains challenging—even robust baseline-free methods depend on modeling power-law behaviors in damage evolution [24]. Moreover, distinguishing damage-induced nonlinearity from effects like sensor placement and modal shape requires sophisticated signal separation techniques [25]. While localization in complex geometries has been demonstrated via simulations, performance depends heavily on precise geometry modeling and crack characterization. The method's sensitivity to contact and fatigue cracks, especially in steel structures, underscores its potential, but also highlights the need for improved processing methods to isolate defect signals accurately [26].

This research is motivated by the potential of the VAM technique to enhance structural integrity assessment significantly. This research is focused on two major topics: (1) enhancing the Modulation Index (MI) separation using models that can simultaneously describe amplitude, frequency, and phase modulation, mathematically and experimentally. (2) developing a novel approach for defect localization using the VAM technique. These methodologies are validated experimentally using aluminum specimens, bridging the gap between theoretical developments and practical applications.

1.3 Literature review

1.3.1 Vibro-Acoustic Modulation and MI Separation

Donskoy et al. [1] discussed the nonlinear interaction between ultrasonic waves and low-frequency vibrations at contact interfaces containing defects, such as cracks and delamination, using the VAM technique. By modulating an HF ultrasonic wave with LF vibrations, defect-induced signals can be distinguished from linear acoustic reflections, allowing more sensitive detection. The authors highlight the challenge of differentiating integrity-reducing flaws from other inhomogeneities using linear acoustics. Their work demonstrates how observing sideband spectral components enhances defect identification and may provide insights into defect size and bonding strength.

Zaitsev et al. [27] introduced a nonlinear-modulation acoustic technique for crack detection based on cross-modulation between a pump and a probe signal. Their results showed that higher harmonics generation methods are affected by initial nonlinear distortions, and the need for intensive pump action complicates the practical application. The authors proposed a flexible approach to utilize sample resonance frequencies for enhancing small crack detection, which is also unaffected by initial nonlinear distortions in the electronics.

Duffour et al. [28] examine the effectiveness of VAM for crack detection in metals, focusing on the amplitude modulation of ultrasonic waves (HF signal) by LF vibrations. The authors investigated the relationship between crack size and modulation strength, noting that the correlation is poor due to the sensitivity of the technique to initial crack states and setup conditions. They identified several areas for further refinement of the VAM technique. Enhancing sensitivity by understanding the influence of crack morphology and initial crack openness on modulation strength. Additionally, improving robustness by determining the minimum LF strain necessary for reliable crack detection under varying industrial conditions is suggested. Moreover, the authors highlighted the importance of identifying optimal ultrasonic frequencies to maximize sensitivity, as significant variability in sideband amplitudes was observed across frequencies.

Zaitsev et al. [29] addressed the physical factors governing the minimal detectable crack size and compared nonlinear modulation techniques with linear frequency-shift approaches. Results showed that while nonlinearity can significantly increase sensitivity, intrinsic atomic nonlinearities in intact materials impose fundamental limits on detection. The authors suggest exploring higher-order nonlinear effects to enhance detection.

In another work, Donskoy [30] emphasized that linear methods often miss subtle damage in structures. Nonlinear methods, including harmonic distortion and modulation techniques, exploit stress-strain nonlinearities that become more pronounced in the vicinity of defects such as cracks or delamination. The challenge lies in differentiating incipient damage from inherent material features and establishing reliable references for background nonlinearity. However, the high sensitivity to flaws with nonlinear properties makes these methods promising for long-term structural health monitoring.

Aymerich and Staszewski [31] explored cross-modulation vibro-acoustic techniques for detecting impact damage in composite laminates. A slow, amplitude-modulated pumping wave is paired with a constant-amplitude probing wave, producing modulation effects that indicate the presence of damage. The study demonstrated how sidebands in the power spectrum of the probing wave correlate with the severity of barely visible impact damage. Despite boundary condition challenges, the authors validate the flexibility and effectiveness of the technique for early-stage damage detection.

In 2010, Hu et al. [32] investigated nonlinear VAM for crack detection using piezoceramic transducers, focusing on separating amplitude and frequency modulations via the Hilbert-Huang transform (HHT). Their findings show that amplitude modulation correlates more reliably with crack severity than frequency modulation, underscoring the limitations of relying solely on frequency analysis. The authors provided a clear indication of damage progression by isolating the amplitude component.

Klepka et al. have conducted significant research on employing nonlinear acoustics for damage detection, particularly focusing on fatigue cracks in aluminum plates and impact-induced defects in composite materials. In 2011 [2], they investigated the role of low-frequency vibration modes in enhancing modulation intensity. Their results highlighted that energy dissipation is the primary contributor to nonlinear modulations rather than the traditional crack opening-closing mechanism. This fact helps the detection of early-stage cracks, even when strain fields are relatively weak. In subsequent research [33], they extended their work to composite materials, targeting barely visible impact damage using nonlinear VAM. By combining LF modal excitations with HF ultrasonic waves, their method produced prominent modulation sidebands in damaged areas, revealing hidden structural defects. This study highlighted the importance of understanding acoustic interactions with defects and emphasized the potential of VAM for effective early-stage damage identification in composites. Later in 2013 [34], they investigated the effect of different LF excitations on the VAM response. The study introduced broadband and aperiodic LF excitations, eliminating the need for preliminary modal testing typically required in traditional VAM techniques.

Specifically, they proposed chirp signals combined with wavelet-based filtering to effectively isolate modulation sidebands without performing initial modal analyses. They demonstrated the critical impact of carefully selecting vibration modes and ultrasonic excitation frequencies to detect barely visible impact damage in laminated composites in 2014 [35]. Results showed that modulation intensities were significantly increased by focusing on out-of-plane motions and leveraging local defect resonance frequencies.

Hong Su et al. [36] introduced a nonlinear acoustic modulation technique for crack detection using cross-modulation between the HP pump and LF probe signals. The method enhances detection sensitivity by exploiting sample resonances, showing superior sensitivity to small cracks and reduced susceptibility to electronic distortions.

The necessary conditions (NCs) for generating nonlinear ultrasonic modulation are investigated by Lim et al. in 2017 [37]. The results revealed that: (1) the localized nonlinearity requires a crack perturbation at the anti-nodes position for both high and low frequency excitations. (2) Transient wave inputs prove more effective than stationary vibrations, especially when the crack location is unknown. However, distinguishing between distributed nonlinearity and localized sources remains challenging, prompting exploration of various frequency combinations to avoid spurious modulation from intrinsic material features.

An algorithm for separating amplitude and frequency modulations in steel components during fatigue damage progression was proposed by Donskoy et al. [38, 39] in 2019. Early micro-crack stages exhibit mostly frequency modulation, while amplitude modulation becomes pronounced during the formation of macro-cracks. This research offers a potential method for early crack detection and life prediction.

Klepka et al. [40] examined nonlinear modulation effects in vibro-acoustic tests for detecting contact-type damage. They identified that modulation patterns, notably amplitude and frequency modulations, depend heavily on excitation amplitudes and interactions between low- and high-frequency signals with damaged surfaces.

In 2020, Opperman et al. [41] employed mathematical approaches to explain amplitude and phase modulation, utilizing a short-time Fourier transform (STFT) in their research to estimate amplitude and phase modulation separately. They noted that their results could not confirm whether either AM or PM/FM is a reliable index for revealing a defect.

The interaction of an ultrasound signal and two types of cracks, an inner and a surface defect, with different lengths, widths, angles, and numbers of defects, was investigated numerically by Zhan et al. [42] in different scenarios in 2021. The simulation results show that the nonlinear phenomenon strongly depends on the length and width of cracks. The second and third-order harmonics increase exponentially as the length of both cracks increases; however, they decrease with increasing crack width. With respect to the angle between the crack direction and the propagation path, the study indicates that the nonlinearity decreases with increasing angle.

1.3.2 Defect localization

Michaels et al. [43, 44] investigated the efficacy of four damage localization methods: (1) Time-of-Arrival (TOA), (2) Time-Difference-of-Arrival (TDOA), (3) Energy Arrival, and (4) Reconstruction Algorithm for the Probabilistic Inspection of Damage (RAPID) using sparse ultrasonic sensor arrays for structural health monitoring. These methods rely on differenced signals, calculated by comparing signals from damaged and undamaged (baseline) structures, to detect and localize damage. Results showed that the TOA method demonstrated the best balance of localization accuracy and signal-to-noise ratio, while the TDOA method was the most robust to group velocity errors. The Energy Arrival and RAPID methods, though strong in signal-to-mean-noise ratios, exhibited reduced performance in other areas, particularly under non-ideal conditions. The RAPID method, designed for larger transducer arrays, was notably less effective with fewer sensors. The discussion emphasizes that TOA offers the most reliable performance under both ideal and non-ideal conditions, while the TDOA method is more tolerant of parameter deviations.

The localization of defects using a single wave excitation (Lamb wave) has been investigated by researchers. A tone burst at a specific central frequency is excited by an actuator, and the responses are measured simultaneously at the receivers. By comparing the responses before (baseline) and after the damage, the location of the defect can be calculated using a damage image method, as explained in subsection 2.5.1 [43-62]. These methods require a baseline measurement for damage localization. Despite the baseline measurement requirement for traditional lamb wave localization, some researchers have suggested signal compensation techniques that can be applied after the response measurement to localize damage using a one-time measurement [63-68].

Li et al. [69] investigated the localization of a 15 mm crack using an arrangement of twelve piezoelectric sensors, including six senders (actuators) and six receivers, attached along both sides of a rectangular plate. A LF continuous signal and an HF tone burst signal with a length of 600 μs were excited by one sender. The six receivers on the opposite side measured the signal simultaneously. The Short-Time Fourier Transform (STFT) with a window length of 600 μs was used to evaluate the measured signal. The signal amplitude at the sideband frequency is higher when the defect is positioned along the path between the sender and receiver. A probability damage imaging method was used for localization in this test. Defect localization was possible with acceptable accuracy. However, successful measurement requires an array of sensors, and further, the defect was positioned within the array of piezoelectric sensors.

Pieczonka et al. [70] used harmonic and sideband image mapping by applying the VAM technique. Low and high-frequency signals were excited by two different piezoelectric sensors, and a laser vibrometer measured the system response. Three methods, (1) the vibrothermography, (2) the higher harmonics imaging, and (3) the sideband imaging method, were used for defect localization within a comparative study. In the vibrothermography method, a tone burst signal was excited by a piezoelectric sensor, and a thermographic camera measured the surface temperature of the plate. The surface temperature distribution indicated the areas where energy is converted to heat. The area adjacent to the crack revealed a higher temperature than remote locations on the plate. In the higher harmonics imaging method, a single frequency signal was excited by a piezoelectric sensor, and the amplitude of the measured signal at the first harmonic was used for localization. For the sideband imaging method, low- and high-frequency signals were excited by piezoelectric sensors. The sideband density, defined as the mean value of the first sideband amplitude, was used for damage imaging. The study concluded that the sideband imaging method produces more accurate results than the higher harmonics imaging method.

Xiao et al. [71] addressed the critical limitation of the VAM in localizing micro-cracks, despite its high sensitivity to these defects compared to linear acoustic methods. The authors proposed a novel combination of VAM with the Time Reversal (TR) technique. Theoretical studies using finite element (FE) simulations and experimental validation on an aluminum plate demonstrated that time-reversed nonlinear signals successfully focused around the crack, allowing for its localization and characterization.

The capability of the Lamb wave mixing method for localizing the defect was investigated by Aslam et al. [72] by evaluating the higher harmonics generated by a defect in a thin plate numerically and experimentally. Two signals at different frequencies were excited with a time delay, such that the two signals arrived at the defect simultaneously, and the Lamb wave mixing took place at the defect zone. The results showed that the higher harmonics and sideband frequency amplitudes were pronounced in the defect zone. However, in order to find the location of the defect in a plate-like component, this approach needs to be repeated for any potential defect zone in a checkerboard pattern.

Karve and Mahadevan [73] used VAM and a binary damage index for damage localization in a numerical concrete model. Low- and high-frequency signals were excited on the top side of the model, and signals were measured by sensors that were placed on the bottom side of the model. The sum of the first sideband amplitude was used as a damage index for localization. The simulation results showed that the sensor's proximity to the damage matters for defect localization. The sensor closer to the damage indicated a higher damage index value than the sensor further away from the damage location. The damage index was evaluated for all sensors in the damage localization process.

At another work, Aslam et al. [74] numerically investigated a new A0/S0 mode signal generated by a defect. Two signals at different frequencies were excited to study the Lamb wave mixing. A time delay between the signals controlled the Lamb mixing zone. A damage index (DI) was used to compare the results. The results showed that the DI increases and decreases with increased crack length and width, respectively.

The Lamb wave frequency-mixing method for localizing a crack in a thin plate using a 2D Finite Element model (2000 mm x 2 mm) was introduced by Wang et al. [75] An A0-mode LF and an S0-mode HF tone burst signal were excited by two piezoelectric sensors on the same side of the sample. A new A0-mode was generated by the defect when both tone bursts arrive at the same time at the location of the defect. This simultaneous arrival at the defect location was controlled by a time delay of one of the signals. The newly generated A0-mode signal at frequency ω-Ω propagated in the opposite direction and was measured by the receivers. The generated A0-mode at ω-Ω was extracted from the measured signal by using the Pulse Inverse Technique and a bandpass filter. The time of flight of this extracted signal revealed the defect location within a numerical assessment.

Miele et al. [76] employed machine learning (ML) methods for localization using the VAM technique, using a FE model. Two neural networks, a regression model to estimate damage depth, and a classifier for detecting crack presence, achieve around 60–64% accuracy.

1.4 Thesis structure

In this chapter, several published articles related to defect detection using the VAM technique and defect localization using the Lamb waves and the VAM technique are reviewed. The following points can be highlighted as key aspects regarding MI separation in this section:

- The published results demonstrated the capability of the VAM technique in detecting small-sized defects (on the millimeter scale).
- The amplitude and frequency modulation indices can serve as indicators of crack growth in the SUT; however, the precise relationship between these parameters and the crack still requires further investigation.
- Despite the introduction and application of various techniques for separating MIs in the response signal, a detailed mathematical analysis of different modulation models is still required to overcome computational limitations, such as the potential occurrence of the nonmodulated carrier in the measured response.

The following points can be highlighted as key aspects regarding localization in this section:

- The first sideband is of particular interest because (1) it shows the nonlinear behavior of a crack, and (2) its amplitude is larger than that of higher-order sidebands.
- The applied HF signal duration appears to be an important parameter for avoiding signal overlap. However, the effect of signal duration on covering the information about the defect location still requires further investigation.
- The review of the literature demonstrates extensive results regarding the application of the VAM technique for defect localization. However, most of these results have been derived from numerical simulations. There is a clear need for the development of algorithms capable of identifying real defect locations on a plate under practical conditions, accounting for factors such as the nonlinear effects of measurement devices and noise.
- The possibility of defect localization using the minimum number of sensors, particularly in cases where the defect is located outside the sensor arrangement, needs more investigation.

In this dissertation, efforts have been made to build upon the findings of previous researchers and to address the identified shortcomings, aiming to advance the possibility of defect localization with minimal measurements and maximum accuracy using the VAM technique. Furthermore, as a second focus of this dissertation, an attempt has been made to examine existing models for the MI separation from both mathematical and signal processing perspectives, exploring the potential for early defect detection through variable separation. In the following chapter, the fundamental concepts utilized in this research are briefly introduced and discussed.

Chapter 2 begins with a brief introduction to Lamb waves and the VAM method. In the remainder of this chapter, various categorized signal models are introduced, and their differences in phase shift are examined with respect to changes in modulation indices. The mathematical description presented in this chapter will be used in the subsequent chapter to separate modulation indices. Additionally, the fundamental principles of localization using Lamb waves are introduced.

Chapter 3 introduces the methodology employed in this study. As the first study, the MIs separation methods employed by various researchers are first introduced, along with a discussion of their potential limitations. Subsequently, new approaches have been proposed to mitigate these shortcomings and enhance the separation of MIs. Additionally, a combined modulation model is introduced, which can explain the change in phase shift of sidebands resulting from changes in MIs. Furthermore, the sensitivity analysis of the phase shifts and damage modulation index is mathematically discussed in this chapter. Defect localization using the VAM technique is introduced in this chapter as the second main topic investigated in this dissertation. This chapter explains how the combination of conventional Lamb wave-based defect detection methods with the VAM theory, which involves generating a modulated signal by a nonlinear source, can assist in defect localization.

The algorithms introduced in this study have been experimentally evaluated, and their results are presented in Chapter 4. In the MI separation section, the results obtained from the AFM model are compared with those from the SPHS method. Subsequently, to facilitate the application of the newly proposed AFPM model, its validity is assessed by examining the phase shift variations of the signal at the first sideband frequencies, $\omega \pm \Omega$. Finally, the results of MI separation using this approach are presented. In the defect localization section, the detection of a crack in the test specimen is investigated under conditions where the HF signal is excited as a tone burst. It is experimentally demonstrated that the presence of a nonlinear source, here a real crack, can modulate the signal that passes through it, while leaving unaffected the portions that do not propagate through the crack. The frequency component generated by the crack propagates independently at a different speed. Furthermore, the effects of varying signal lengths and different sensor configurations are examined under various conditions.

Finally, Chapter 5 discusses research summary, outcomes, and some additional possible areas for further investigation.

Chapter 2

Theoretical Background

This chapter provides a comprehensive theoretical foundation for understanding and employing Lamb waves and vibro-acoustic modulation (VAM) techniques in structural health monitoring (SHM) and nondestructive testing (NDT). Initially, the principles and mathematical frameworks underpinning Lamb wave propagation in thin plate-like structures are discussed. Emphasis is placed on symmetric and antisymmetric modes, and the significance of dispersion curves, along with their dependence on material properties, plate thickness, and frequency, is explained.

Subsequently, the chapter explores the nonlinear ultrasonic methodology of vibro-acoustic modulation, detailing its unique advantages in defect detection. The roles and interactions of low-frequency (LF) and high-frequency (HF) signals, as well as the types of excitation, are also discussed in the following sections.

For a clear understanding of modulation models, different combinations of modulation, such as amplitude, frequency, and phase, for a single tone signal, are mathematically introduced. The separation of modulation indices is discussed at the end of this section.

At the end of the chapter, the theory of defect localization using Lamb waves is presented, with a focus on the Delay-and-Sum (DAS) damage imaging method. The theoretical framework and application of the DAS algorithm for accurately locating structural defects through wave propagation analysis are discussed. This foundational knowledge sets the stage for the subsequent experimental validation and application of these theoretical insights in practical scenarios, which are represented in the following chapters.

2.1 Lamb Waves and Their Role in NDT

Lamb waves were first theoretically described by Horace Lamb in 1917 [77]. They are a subset of guided waves in thin plate-like structures whose thickness is comparable to the acoustic wavelength. When an elastic wave propagates in a plate of finite thickness, the mechanical energy remains guided between the two free boundaries of the plate [78]. Since then, these waves have been widely applied in structural health monitoring, non-destructive testing, and other fields where thin-walled components, such as aircraft fuselages, pipelines, or plate-like structures, are examined [78].

Lamb waves have gained popularity in NDT due to their ability to travel long distances along thin structures, efficiently covering large areas [77, 79, 80]. In contrast to bulk waves, whose energy radiates throughout the entire volume, Lamb waves remain guided within the plate [77, 78]. They are easily affected by changes in thickness, material properties, and boundary conditions [78, 81, 82]. Choosing the proper mode and frequency can help detect specific types of damage more effectively, even with many wave modes (A and S) [78, 80, 83].

2.1.1 Symmetric and Antisymmetric Modes

In an isotropic plate of thickness $2h$, the displacement field $u(x, y, z, t)$ must satisfy both scalar (longitudinal), $\phi(x, y, z, t)$, and vector (shear), $\psi(x, y, z, t)$, wave equations that are represented in Equation 2.1, where c_L and c_T represent the longitudinal and shear wave velocities. c_L and c_T are material-related parameters, which are described in Equation 2.2, where E, ν and ρ denote the Young's Modulus, Density, and Poisson's ratio of the material [78].

$$\nabla^2\phi - \frac{1}{{c_L}^2}\frac{\partial^2\phi}{\partial t^2} = 0 \qquad \text{(a)}$$

$$\nabla^2\psi - \frac{1}{{c_T}^2}\frac{\partial^2\psi}{\partial t^2} = 0 \qquad \text{(b)}$$

$$u = \nabla\phi + \nabla \times \psi \qquad \text{(c)} \qquad (2.1)$$

$$c_L = \sqrt{\frac{E(1-\nu)}{\rho(1+\nu)(1-2\nu)}} \qquad \text{(a)}$$

$$c_T = \sqrt{\frac{E}{2\rho(1+\nu)}} \qquad \text{(b)} \qquad (2.2)$$

For Lamb waves, the top and bottom surfaces $z = \pm h$, are traction-free, as Equation 2.3 represents, where σ denotes the stress tensor. Applying these boundary conditions to the above equations leads us to the Rayleigh–Lamb frequency equations for symmetric (S mode) and antisymmetric (A mode) modes, which are illustrated in Equation 2.4. In this equation h, k, ω, and c_P are the half value of the plate thickness, wavenumber, wave circular frequency, and phase velocity, respectively [78].

$$\sigma_{zz} = 0, \qquad \sigma_{xz} = 0 \ \text{ at } \ z = \pm h \qquad (2.3)$$

$$\frac{\tan(qh)}{\tan(ph)} = -\frac{4k^2pq}{(k^2-q^2)^2} \qquad \text{Symmetric modes (S modes)}$$

$$\frac{\tan(qh)}{\tan(ph)} = -\frac{(k^2-q^2)^2}{4k^2pq} \qquad \text{Antisymmetric modes (A modes)} \qquad (2.4)$$

$$where\text{:} \quad p = \sqrt{\frac{\omega^2}{{c_L}^2} - k^2}\ , \quad q = \sqrt{\frac{\omega^2}{{c_T}^2} - k^2}$$

2.1.2 Dispersion Curve

The phase and group velocity values can be numerically calculated using Equation 2.4 by the following steps [78]:

- Calculate the value of c_L and c_T (The material parameters are considered known) using Equation 2.2.
- Select a frequency (f) and calculate the $\omega = 2\pi f$.
- Solve Equation 2.4 numerically to find the values of k , for A and S modes.
- Calculate the value of phase velocity (c_p) and group velocity (c_g) using Equation 2.5

$$c_p = \frac{\omega}{k} \qquad \text{(a)}$$
$$c_g = \frac{d\omega}{dk} \qquad \text{(b)} \qquad (2.5)$$

Figure 2.1 shows an example of MATLAB-simulated dispersion curves for an aluminum plate (AlMg3) with parameters listed in Table 2.1. As the results show, it is evident that phase velocity (c_P) and group velocity (c_g) are frequency-thickness-dependent , which means each frequency propagates with a different velocity. It is noticeable that the difference in propagation speed for frequencies has been used in the defect localization algorithm (see subsection 3.2.6).

Name	Sym	Simulated Value
Young's Modulus	E	$7 \times 10^{10} \frac{N}{m^2}$
Density	ρ	$2700 \frac{kg}{m^3}$
Material Thickness	$2h$	$2\ mm$
Poisson's Ratio	ν	0.33

Table 2.1: The parameter values of Aluminum (AlMg3)[1] used for the dispersion curve simulation using MATLAB

2.1.3 Interaction with Defects

The Lamb waves that interact with defects such as cracks, voids, and delaminations can be categorized into the following points:

---

[1] https://www.makeitfrom.com/material-properties/5754-AlMg3-3.3535-A95754-Aluminum

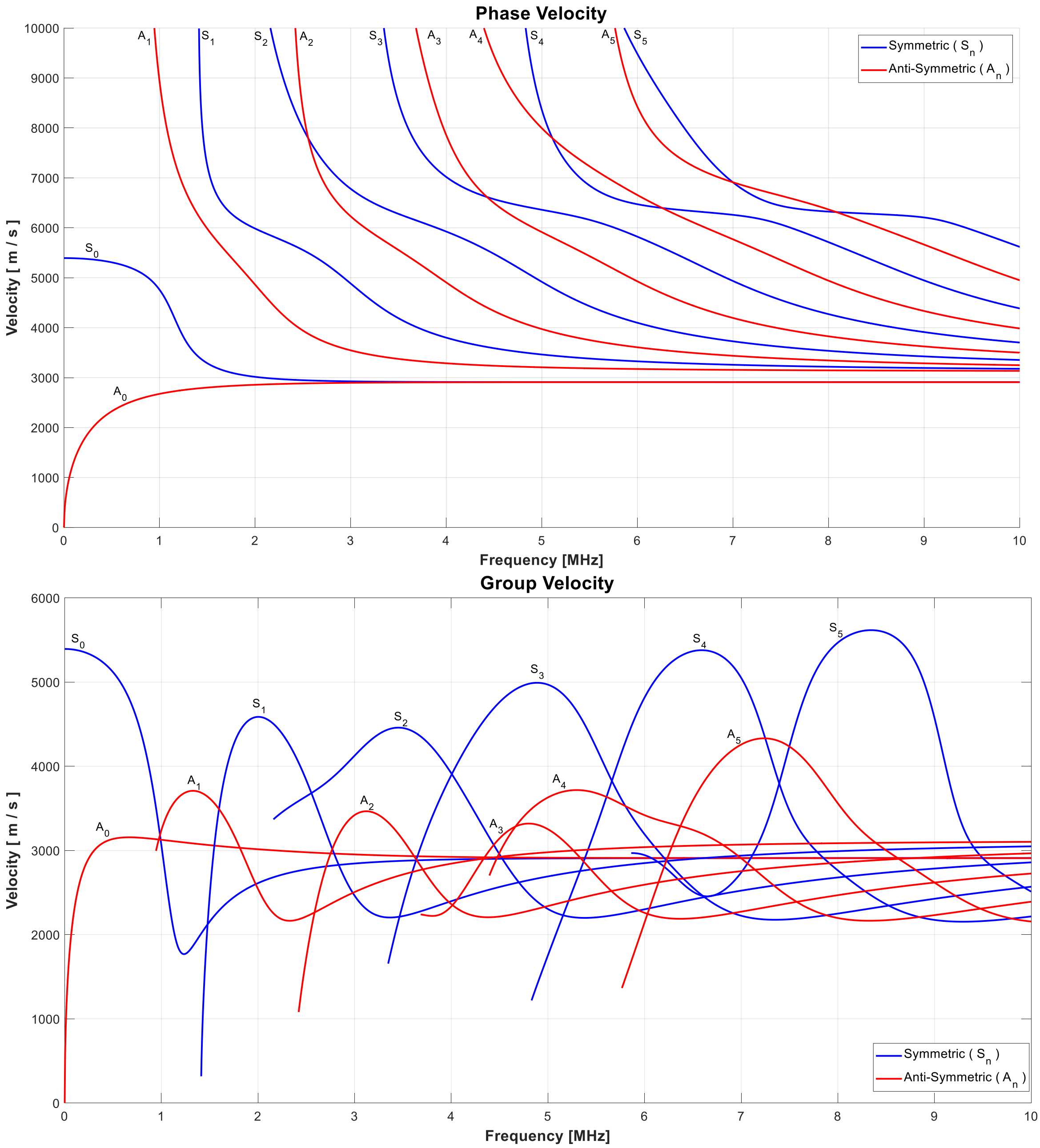

Figure 2.1: The phase and group velocity of A_n and S_n modes (n = 0, 1, …,5) simulated by MATLAB[1] for an Aluminum (AlMg3) with the parameters listed in Table 2.1.

- *Reflection and Mode Conversion:*

When a Lamb wave meets a defect, part of the wave is typically reflected to the receiver. Depending on the defect location, mode conversion can occur. In this situation, an S mode becomes an A mode or vice versa; sometimes, a new mode will be generated and propagated through the material [75, 78, 84-86].

---

[1] Using a 'MathWorks' function:
https://www.mathworks.com/matlabcentral/fileexchange/73050-lamb-wave-dispersion-curve

- *Scattering:*
When the defect size is on the order of the signal wavelength, the signal is scattered by the defect and can be measured by receivers. Research results confirm that the amplitude, direction, and mode content of scattered waves vary with the defect's geometry relative to the Lamb wave's wavelength [78, 81, 84, 87-89].

- *Resonance Effects:*
Defects such as delaminations and disbonds can behave as localized resonators, particularly when their dimensions match specific fractions of the Lamb wave wavelength. This resonant behavior can trap or reflect specific frequency components, resulting in notable modifications in the amplitude and phase of the transmitted or scattered wave [82, 90, 91].

- *Amplitude and Phase Changes:*
As Lamb waves propagate through a structure, defects such as cracks can reduce the amplitude of the transmitted wave and introduce a phase delay. These changes depend on the size and location of the defect [81, 84, 90-92].

2.2 An Introduction to Vibro-Acoustic Modulation

Vibro-acoustic modulation (VAM) is a powerful nonlinear ultrasonic method widely employed for detecting structural defects. This technique uses the nonlinear elastic properties of damaged materials by exciting two waves, low-frequency (LF) and high-frequency (HF) signals, known as pumping and probing waves, respectively [1, 2]. The interaction of these waves at a defect location generates individual modulation signatures that help as sensitive indicators of structural integrity [1, 24, 93]. This section explains the theoretical background, frequency selection, excitation types, and the roles of LF and HF waves in defect detection and localization.

2.2.1 Theoretical Background of VAM

Vibro-Acoustic Modulation (VAM), first introduced by Donskoy and Sutin in 1998, is a nonlinear ultrasonic technique used in NDE and SHM to detect and characterize damage in a wide range of materials and structural components [94]. Unlike conventional (linear) ultrasonic methods, which rely primarily on amplitude attenuation, phase shifts, or Time-Of-Flight (TOF) changes, VAM uses the interaction between two excitations with low and high frequencies [11, 94, 95]. In this method, two signals at low (Ω) and high (ω) frequencies, which are called X_{Ω} and X_{ω} as represented in Equation 2.6, are simultaneously excited to a structure under test (SUT). At the same time, another sensor (or sensors) measures a response signal, which is called $Y_i = F(X_{\omega}, X_{\Omega})$, where i represents the sensor's number. A and θ in Equation 2.6 represent the signal's amplitude and initial phase shift, respectively. Furthermore, the function $F(X_{\omega}, X_{\Omega})$ describe the behavior of SUT against X_{Ω} and X_{ω}.

$$\begin{aligned}
&\text{LF signal:} \quad X_\Omega(t) \equiv X_\Omega(A_\Omega\,,\Omega) = A_\Omega Cos(\Omega t + \theta_\Omega)\,, \Omega = 2\pi f_\Omega && \text{(a)} \\
&\text{HF signal:} \quad X_\omega(t) \equiv X_\omega(A_\omega, \omega) = A_\omega Cos(\omega t + \theta_\omega), \omega = 2\pi f_\omega && \text{(b)} \\
&\text{Measured signal:} \quad Y = F(X_\omega, X_\Omega) && \text{(c)} \quad (2.6)
\end{aligned}$$

Figure 2.2a illustrates the fundamentals of the VAM method. The behavior of the SUT can be described in two different situations:

- *A defect-free structure:*

When the structure is perfectly elastic and defect-free, its stress-strain relationship is well-approximated by a linear Hookean law $\sigma(\varepsilon) = E\,\varepsilon$, where σ, ε, and E represent stress, strain, and Young's Modulus, respectively. Under this condition X_Ω and X_ω do not significantly interact, and no sidebands are generated [1, 94]. Therefore, the frequency response of the measured signal reveals only frequency components at ω and Ω, as shown in Figure 2.2b.

- *A structure with a defect:*

A local defect, such as a crack, introduces a localized nonlinear stress-strain behavior. A simple nonlinear stress-strain can be written using a polynomial expansion, which is shown in Equation 2.7, where α and β are higher-order nonlinear coefficients related to microstructural or contact-type nonlinearity. Under this condition, the high-order polynomial terms in the nonlinear stress-strain expansion generate higher harmonics of X_Ω and X_ω and the sidebands at $\omega \pm n\Omega$ [1, 37, 94, 96]. Therefore, the frequency response of the measured signal reveals frequency components not only at ω and Ω, but higher harmonics of ω and Ω as well as $\omega \pm n\Omega$, as shown in Figure 2.2c.

$$\sigma(\varepsilon) = E\,\varepsilon + \alpha\,\varepsilon^2 + \beta\,\varepsilon^3 + \cdots \tag{2.7}$$

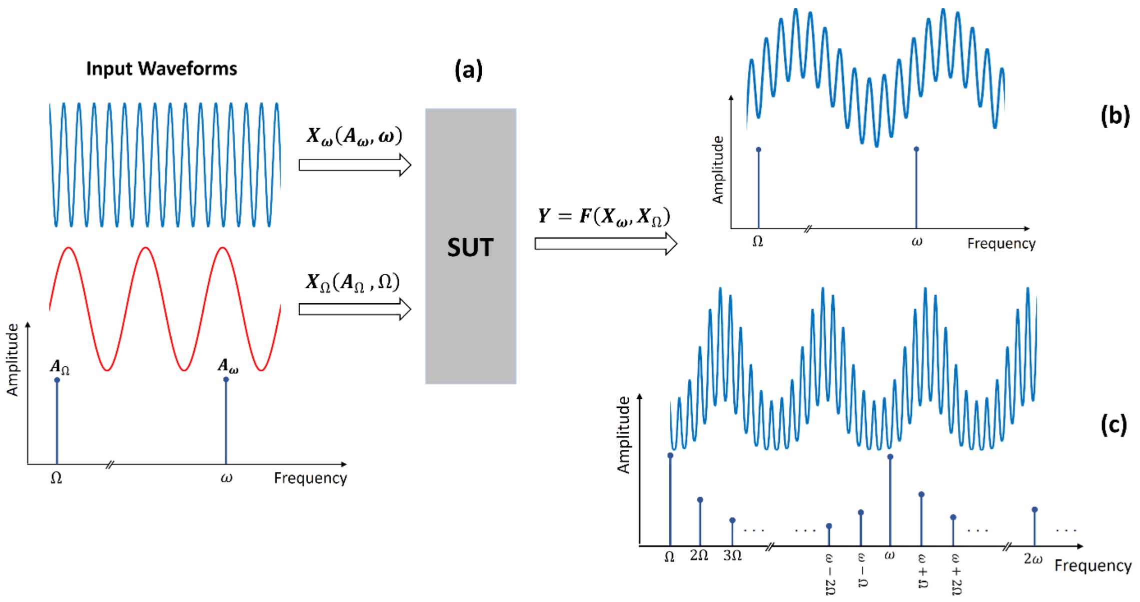

Figure 2.2: The fundamentals of the Vibro-Acoustic Modulation method – a test setup (**a**), the frequency component of the response, when SUT has no defect (**b**), and when SUT has a defect (**c**)

2.2.2 Frequency Selection in VAM

Research results show that VAM is a frequency-dependent method [25]. As shown before, the generation of sidebands depends on how low and high-frequency signals interact with the structure's dynamics and the damage. Therefore, choosing the appropriate low and high frequencies is crucial for maximizing VAM sensitivity and accuracy [25]. Some of the key considerations for frequency selection are the following:

- *Excitation of damage-sensitive modes*

  Experimental results have shown that LF signals play a key role in modulation strength [2, 25, 97]. Selecting a low frequency close to a structure's resonant modes enhances the opening-closing behavior of cracks (also known as "breathing"), making the nonlinear modulation effect stronger and easier to detect. Furthermore, the modulation can be measured strongly when a sideband frequency matches the structure's resonance [2, 97, 98]. Selecting a high range of frequencies for the HF signal provides a smaller wavelength, which means better spatial resolution (A wave with a smaller wavelength oscillates more rapidly in space and can interact with smaller defects) [78, 82, 99].

- *Avoiding interference or insensitivity due to modal nodes*

  When the mode shape of the selected frequencies exhibits minimal vibration or a node at the defect location, the nonlinear interaction between frequencies is significantly reduced, and the defect becomes extremely difficult to identify or even undetectable [37].

- *Separation of frequency bands*

  The low and high frequencies must be chosen to avoid the frequency overlapping between the primary frequencies, their harmonics, and their sidebands for better separation and filter design in the frequency domain [98, 99].

- *The frequency range of sensors*

  Each sensor has an optimal frequency range, known as the eigenfrequency range, which provides accurate and reliable measurements. In the case of using sensors as an actuator or receiver, the low and high frequencies must be chosen to ensure better excitation and measurement, considering the frequencies of the generated sideband.

2.2.3 Types of Excitations in VAM

Various excitation methods can be employed in VAM, each with its advantages and suitable applications. The classical approach utilizes a continuous single-tone sinusoidal waveform for low- and high-frequency signals. Alternatively, other methods use at least one signal as a short-time waveform (tone burst).

- *Continuous waveforms excitation*

  The most widely used form of VAM is to excite both signals as single-tone continuous sinusoidal waveforms to reach a steady-state condition [1-3, 8, 11, 38-41, 93, 96]. Since a single-tone waveform has a narrow band frequency spectrum, this excitation method generates a sharp and clear frequency analysis of the measured signal in the frequency domain.

- *Short-time waveforms (tone burst) excitation*

In this method, one of the low or high-frequency signals excites as a short-time signal (tone burst), while the other excites continuously. The frequency analysis of the measured signal is more advanced in this method because a tone burst signal has a wide-band frequency spectrum, and the energy of the excited signal is less than that of a continuous waveform. Also, this method requires measuring devices with a higher sampling frequency. Despite its challenges, this method is used in defect localization problems [63, 68-72, 74, 75].

2.3 Modulation Indices in VAM

As discussed in subsection 2.2.1, a source of nonlinearity modulates the high-frequency signal by the low-frequency signal, generating sidebands. The easiest way to mathematically visualize the modulation is to consider a single-tone HF signal (carrier) modulated (amplitude, phase, or frequency) by a single-tone LF signal.

A modulation index (MI) in VAM is a quantitative parameter that measures the intensity or degree of interaction between two signals of different frequencies within a material. Generally, two main types of modulation are employed: amplitude modulation (AM) and frequency modulation (FM) [32, 38-40]. Recently, studies have also begun exploring phase modulation (PM) as an additional indicator of nonlinearity [41]. A brief definition of different modulation types is given below, where the HF signal (carrier) and LF signal are defined in Equation 2.6.

Since the experimental results confirm the existence of two different modulation types, amplitude and frequency modulation, exist in the VAM-measured response [32, 38-40], combining different modulation types is described below to show the relationship between the modulation indices and the sideband's parameters (amplitude and phase shift) for the separation.

2.3.1 Amplitude Modulation (AM) model

In this modulation, the amplitude of the HF signal (known also as a carrier) changes based on the LF signal (known as a modulating signal or the data). The amplitude modulation index, AMI (m_a or μ_a), which is calculated using Equation 2.8, quantifies the amount of modulation. The frequency spectrum of the modulated signal always consists of only two symmetric sidebands, as illustrated in Figure 2.3a [100, 101]. Table 2.2 represents the amplitude and phase shift of the amplitude-modulated signal components after replacing $X_\Omega(t)$, defined in Equation 2.6, into the Equation 2.8.

$$A_\omega\big(1+2m_a g(t)\big)\,cos(\omega t+\phi_\omega) \qquad\qquad m_a=\frac{A_{+1}+A_{-1}}{2A_0} \tag{2.8}$$

Frequency (rad)	Amplitude	Phase shift
ω	$A_0 = A_\omega$	$\theta_0 = \phi_\omega$
$\omega + \Omega$	$A_{+1} = m_a A_\omega A_\Omega$	$\theta_{+1} = \phi_\omega + \phi_\Omega$
$\omega - \Omega$	$A_{-1} = m_a A_\omega A_\Omega$	$\theta_{-1} = \phi_\omega - \phi_\Omega$

Table 2.2: The amplitude and phase shift of different signal components in an amplitude-modulated signal when HF and LF signals are single-tone waveforms

2.3.2 Frequency Modulation (FM) model

In this modulation, the frequency of the HF signal changes based on the LF signal. The frequency modulation index, FMI (m_f or μ_f), which is calculated using Equation 2.9, quantifies the amount of modulation, where Δf represents the frequency deviation in the measured signal. This modulated signal theoretically has infinite sidebands in the frequency domain, as represented in Figure 2.3b [100, 101]. Table 2.3 represents the amplitude and phase shift of the frequency-modulated signal components after replacing $X_\Omega(t)$, defined in Equation 2.6, into the Equation 2.9.

$$A_\omega \, cos\left(\omega t + \phi_\omega + 2m_f \int g(t)dt\right) \qquad m_f = \frac{f_{Max} - f_{Min}}{2f_c} = \frac{\Delta f}{2f_c} \tag{2.9}$$

Frequency (rad)	Amplitude	Phase shift
ω	$A_0 = A_\omega J_0(2m_f A_\Omega)$	$\theta_0 = \phi_\omega$
$\omega + \Omega$	$A_{+1} = A_\omega J_1(2m_f A_\Omega)$	$\theta_{+1} = \phi_\omega + \phi_\Omega$
$\omega - \Omega$	$A_{-1} = -A_\omega J_1(2m_f A_\Omega)$	$\theta_{-1} = \phi_\omega - \phi_\Omega$
$\omega + n\Omega$	$A_{+n} = A_\omega J_n(2m_f A_\Omega)$	$\theta_{+n} = \phi_\omega + n\phi_\Omega$
$\omega - n\Omega$	$A_{-n} = A_\omega (-1)^n J_n(2m_f A_\Omega)$	$\theta_{-n} = \phi_\omega - n\phi_\Omega$

Table 2.3: Amplitudes and phase shifts for different signal components in a frequency-modulated signal when HF and LF signals are single-tone waveforms. $J_n(x)$ represents the Bessel function of the first kind, which is defined by Equation 2.10.

$$J_n(x) = \frac{x^n}{2^n n!} \sum_{k=0}^{\infty} \frac{(-1)^k x^{2k}}{k! \, 2^{2k} \prod_{j=1}^{k}(n+j)} \tag{2.10}$$

2.3.3 Phase Modulation (PM) model

In this modulation, the phase of the HF signal changes based on the LF signal. The phase modulation index, PMI (m_p or μ_p), which is calculated using Equation 2.11, quantifies the amount of modulation. Like the FM, this modulated signal has infinite sidebands in the frequency domain, as represented in Figure 2.3c [100, 101]. Table 2.4 represents the amplitude and phase shift of the phase-modulated signal components after replacing $X_{\Omega}(t)$, defined in Equation 2.6, into the Equation 2.11.

$$A_{\omega}\, cos\left(\omega t + \phi_{\omega} + 2m_p\, g(t)\right) \qquad m_p = \frac{\phi_{Max} - \phi_{Min}}{2} = \frac{\Delta\phi}{2} \tag{2.11}$$

Frequency (rad)	Amplitude	Phase shift
ω	$A_0 = A_{\omega} J_0(2m_p A_{\Omega})$	$\theta_0 = \phi_{\omega}$
$\omega + \Omega$	$A_{+1} = A_{\omega} J_1(2m_p A_{\Omega})$	$\theta_{+1} = \phi_{\omega} + \phi_{\Omega} + \frac{\pi}{2}$
$\omega - \Omega$	$A_{-1} = A_{\omega} J_1(2m_p A_{\Omega})$	$\theta_{-1} = \phi_{\omega} - \phi_{\Omega} + \frac{\pi}{2}$
$\omega + 2\Omega$	$A_{+2} = A_{\omega} J_2(2m_p A_{\Omega})$	$\theta_{+2} = \phi_{\omega} + 2\phi_{\Omega} - \pi$
$\omega - 2\Omega$	$A_{-2} = A_{\omega} J_2(2m_p A_{\Omega})$	$\theta_{-2} = \phi_{\omega} - 2\phi_{\Omega} - \pi$
$\omega \pm (2n+1)\Omega$	$A_{\pm(2n+1)} = A_{\omega} J_{2n+1}(2m_p A_{\Omega})$	$\theta_{\pm(2n+1)} = \phi_{\omega} \pm (2n+1)\phi_{\Omega} - tan^{-1}\left(\frac{(-1)^{n+1} J_{2n+1}(2m_p A_{\Omega})}{0}\right)$
$\omega \pm 2n\Omega$	$A_{\pm 2n} = A_{\omega} J_{2n}(2m_p A_{\Omega})$	$\theta_{\pm 2n} = \phi_{\omega} \pm 2n\phi_{\Omega} - tan^{-1}\left(\frac{0}{(-1)^{n} J_{2n}(2m_p A_{\Omega})}\right)$

Table 2.4: Amplitudes and phase shifts for different signal components in a phase-modulated signal when HF and LF signals are single-tone waveforms

Mathematically, for single-tone waveforms, the phase and frequency modulations can be converted to each other with a change in the LF signal's phase shift, as represented in Equation 2.12.

$$\begin{aligned} FM:\ & A_{\omega}\, cos\left(2\pi f_{\omega} t + \phi_{\omega} + 2m_f \int g(t)dt\right) \\ &= A_{\omega} \cos\left(\omega t + \phi_{\omega} + 2m_f A_{\Omega} \sin(\Omega t + \phi_{\Omega})\right) \\ &= A_{\omega} \cos\left(\omega t + \phi_{\omega} + 2m_f A_{\Omega} \sin(\Omega t + \phi_{\Omega})\right) \\ &= A_{\omega} \cos\left(\omega t + \phi_{\omega} + 2m_f A_{\Omega} \cos\left(\Omega t + \phi_{\Omega} - \frac{\pi}{2}\right)\right) \equiv PM \end{aligned} \tag{2.12}$$

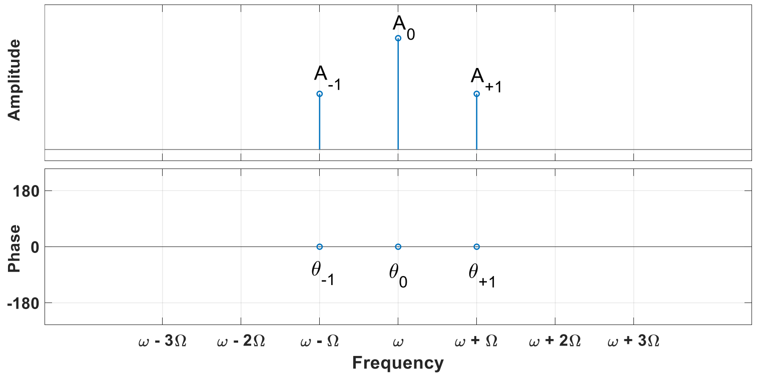

(**a**) An amplitude-modulated (AM) signal: only two sidebands appear in the frequency domain, and there is no change in the phase shift of the signals (see Table 2.2)

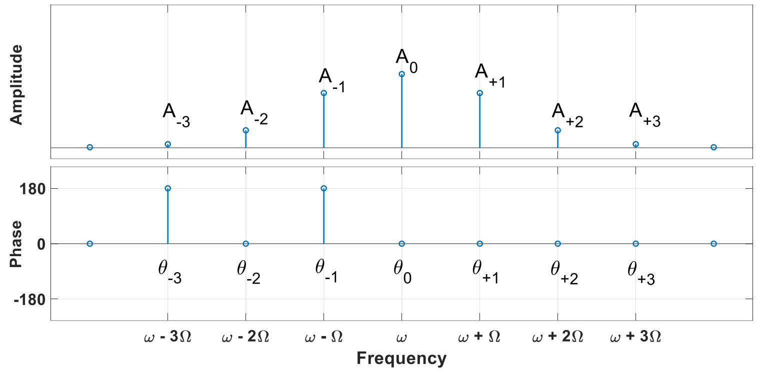

(**b**) a frequency-modulated (FM) signal: the number of sidebands that appear in the frequency domain is theoretically infinite, and there are changes (0 or π) in the phase shift of the signals (see Table 2.3)

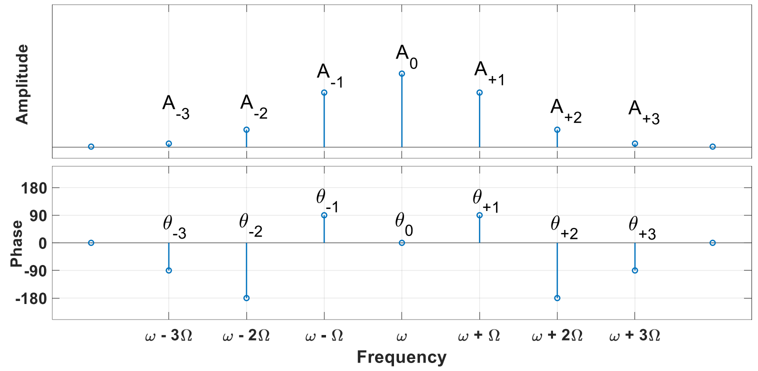

(**c**) a phase-modulated (PM) signal: the number of sidebands that appear in the frequency domain is theoretically infinite, and there are changes (0, $\pm\frac{\pi}{2}$, or π) in the phase shift of the signals (see Table 2.4)

Figure 2.3: The FFT spectrum of three different modulated signals simulated by MATLAB, where the carrier is $A_\omega Cos(2\pi\omega t)$, and the LF signal is $A_\Omega Cos(2\pi\Omega t)$

2.3.4 Amplitude-frequency modulation (AFM) model

In this modulation, both the amplitude and frequency of the HF signal change based on the LF signal, which is illustrated in Equation 2.13, where m_a and m_f quantify the amount of amplitude and frequency modulations, respectively. The number of sidebands in this model is also theoretically infinite, which is shown in Figure 2.4 [1, 2, 93, 94, 96, 100, 101]. Table 2.5 represents the amplitude and phase shift of the amplitude-frequency modulated signal components after replacing $X_\Omega(t)$, defined in Equation 2.6, into the Equation 2.13. As evident in Table 2.5, <u>the phase shifts of the signal components remain unchanged despite changes in the modulation indices</u> (see Figure 2.4b).

$$A_\omega\big(1 + 2m_a g(t)\big)\cos\left(\omega t + \phi_\omega + 2m_f \int g(t)dt\right) \tag{2.13}$$

Frequency (rad)	Amplitude	Phase shift
ω	$A_0 = A_\omega J_0(2m_f A_\Omega)$	$\theta_0 = \phi_\omega$
$\omega + \Omega$	$A_{+1} = A_\omega\Big(J_1(2m_f A_\Omega) + m_a A_\Omega J_0(2m_f A_\Omega) + m_a A_\Omega J_2(2m_f A_\Omega)\Big)$	$\theta_{+1} = \phi_\omega + \phi_\Omega$
$\omega - \Omega$	$A_{-1} = A_\omega\Big(-J_1(2m_f A_\Omega) + m_a A_\Omega J_0(2m_f A_\Omega) + m_a A_\Omega J_2(2m_f A_\Omega)\Big)$	$\theta_{-1} = \phi_\omega - \phi_\Omega$
$\omega + 2\Omega$	$A_{+2} = A_\omega\Big(J_2(2m_f A_\Omega) + m_a A_\Omega J_1(2m_f A_\Omega) + m_a A_\Omega J_3(2m_f A_\Omega)\Big)$	$\theta_{+2} = \phi_\omega + 2\phi_\Omega$

$\omega - 2\Omega$	$A_{-2} = A_{\omega}\left(J_2(2m_f A_{\Omega}) - m_a A_{\Omega} J_1(2m_f A_{\Omega}) - m_a A_{\Omega} J_3(2m_f A_{\Omega})\right)$	$\theta_{-2} = \phi_{\omega} - 2\phi_{\Omega}$
$\omega + n\Omega$	$A_{+n} = A_{\omega}\left(J_n(2m_f A_{\Omega}) + m_a A_{\Omega} J_{n-1}(2m_f A_{\Omega}) + m_a A_{\Omega} J_{n+1}(2m_f A_{\Omega})\right)$	$\theta_{+n} = \phi_{\omega} + n\phi_{\Omega}$
$\omega - n\Omega$	$A_{+n} = (-1)^n A_{\omega}\left(J_n(2m_f A_{\Omega}) - m_a A_{\Omega} J_{n-1}(2m_f A_{\Omega}) - m_a A_{\Omega} J_{n+1}(2m_f A_{\Omega})\right)$	$\theta_{-n} = \phi_{\omega} - n\phi_{\Omega}$

Table 2.5: The amplitude and phase shift for different signal components in an amplitude-frequency modulated (AFM) signal when HF and LF signals are single-tone waveforms

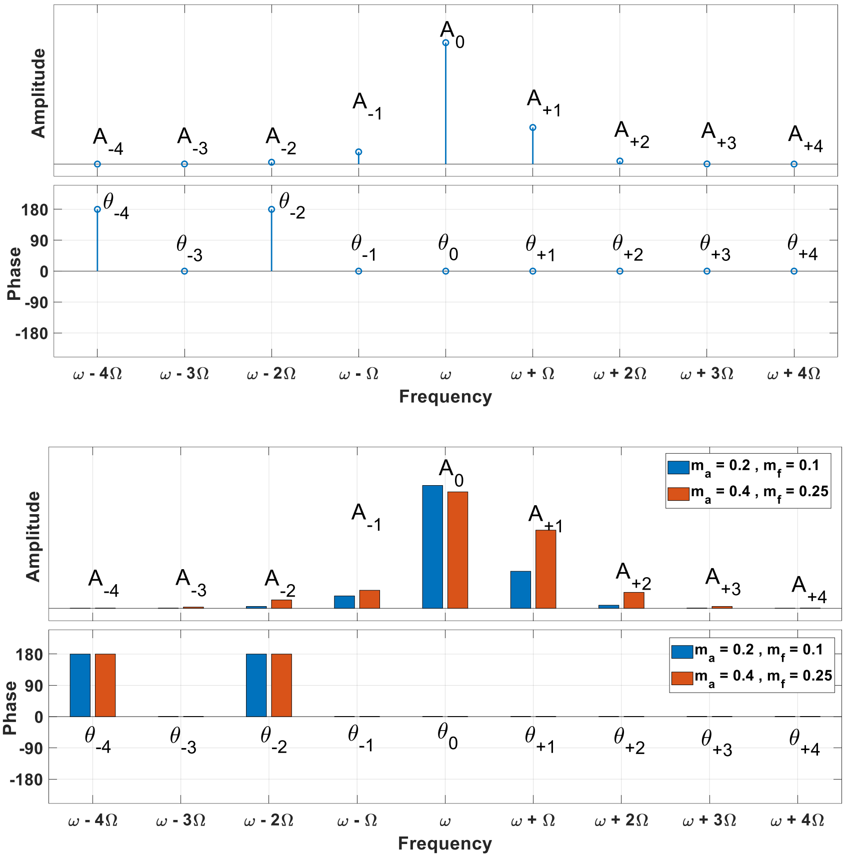

(**a**) an amplitude-frequency modulated (AFM) signal: the number of sidebands that appear in the frequency domain is theoretically infinite, and there are changes (0 or π) in the phase shift of the signals (see Table 2.5)

(**b**) The phase shift of the signal components remains unchanged despite changes in the modulation indices (see Table 2.5)

Figure 2.4: The FFT spectrum of a simulated Amplitude-Frequency Modulated signal using MATLAB

2.3.5 Amplitude-Phase Modulation (APM) model

In this modulation, both the amplitude and phase of the HF signal change based on the LF signal, which is illustrated in Equation 2.14, where m_a and m_p quantify the amount of amplitude and phase modulations, respectively. The number of sidebands in this model is also theoretically infinite, as shown in Figure 2.5. It is noticeable that due to the similarity of phase modulation to frequency modulation (see Equation 2.12), the mathematical description of this model is not directly presented in reference books; however, it can be calculated using some mathematical relations. Table 2.6 represents the amplitude and phase shift of the amplitude-phase modulated signal components after replacing $X_{\Omega}(t)$, defined in Equation 2.6, into equation 2.14. As evident in Table 2.6, the phase shifts of the signal components change with changes in the modulation indices (see Figure 2.5b-c) and the amplitude of the corresponding sidebands ($|A_{\pm n}|$) **are symmetric** in this model.

$$A_{\omega}\left(1+2m_a g(t)\right) cos\left(\omega t+\phi_{\omega}+2m_p\, g(t)\right) \tag{2.14}$$

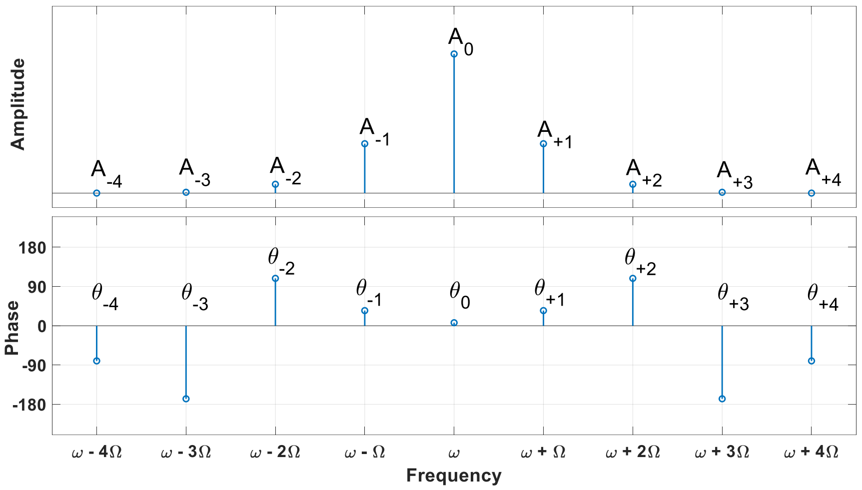

(**a**) an amplitude-phase modulated (APM) signal: the number of sidebands that appear in the frequency domain is theoretically infinite, and the phase shift of the signals changes based on Table 2.6

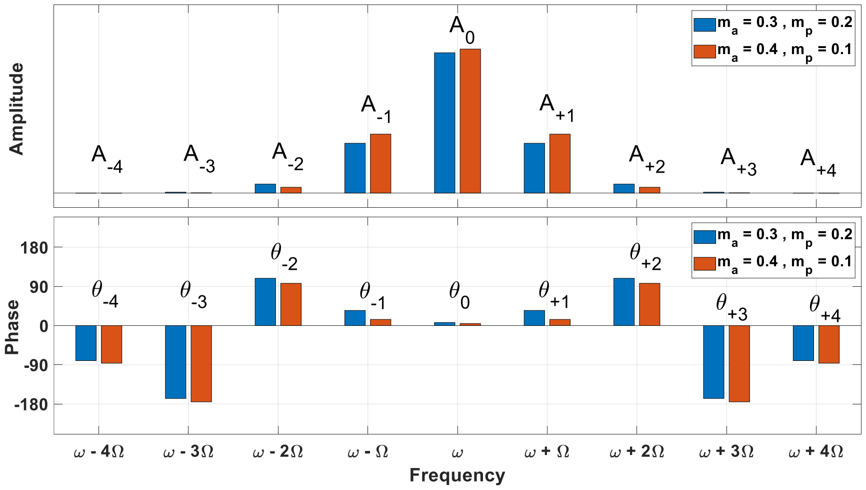

(**b**) phase shifts of the signal components vary with the change in the modulation indices (see Table 2.6)

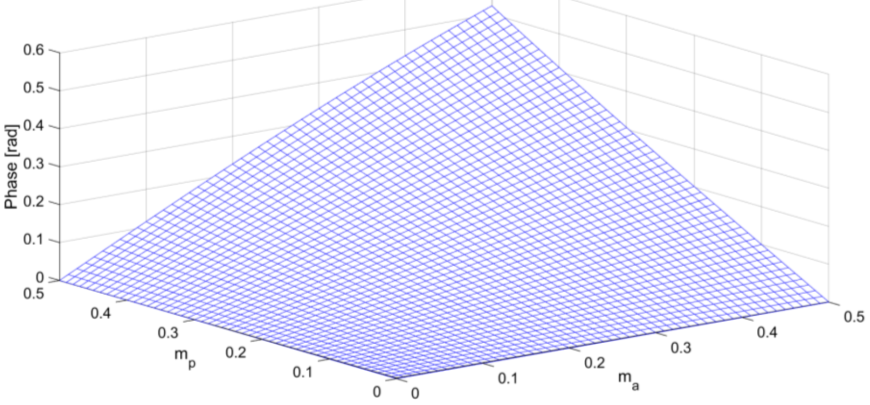

(**c**) A 3D plot of the phase shift of the primary frequency component, θ_0 , when m_a and m_p vary from 0 to 0.5 (see Table 2.6)

Figure 2.5: The FFT spectrum of a simulated Amplitude-Frequency Modulated signal using MATLAB.

Frequency (rad)	**Amplitude**	**Phase shift**
ω	$A_0 = A_\omega\sqrt{{J_0}^2(\tau) + \big(-2m_a A_\Omega J_1(\tau)\big)^2}$	$\theta_0 = \phi_\omega - tan^{-1}\left(\frac{-2m_a A_\Omega J_1(\tau)}{J_0(\tau)}\right)$
$\omega + \Omega$	$A_{+1} = A_\omega\sqrt{\big(m_a A_\Omega J_0(\tau) - m_a A_\Omega J_2(\tau)\big)^2 + \big(-J_1(\tau)\big)^2}$	$\theta_{+1} = \phi_\omega + \phi_\Omega - tan^{-1}\left(\frac{-J_1(\tau)}{m_a A_\Omega J_0(\tau) - m_a A_\Omega J_2(\tau)}\right)$
$\omega - \Omega$	$A_{-1} = A_\omega\sqrt{\big(m_a A_\Omega J_0(\tau) - m_a A_\Omega J_2(\tau)\big)^2 + \big(-J_1(\tau)\big)^2}$	$\theta_{-1} = \phi_\omega - \phi_\Omega - tan^{-1}\left(\frac{-J_1(\tau)}{m_a A_\Omega J_0(\tau) - m_a A_\Omega J_2(\tau)}\right)$
$\omega + 2\Omega$	$A_{+2} = A_\omega\sqrt{\big(-J_2(\tau)\big)^2 + \big(-m_a A_\Omega J_1(\tau) + m_a A_\Omega J_3(\tau)\big)^2}$	$\theta_{+2} = \phi_\omega + 2\phi_\Omega - tan^{-1}\left(\frac{-m_a A_\Omega J_1(\tau) + m_a A_\Omega J_3(\tau)}{-J_2(\tau)}\right)$
$\omega - 2\Omega$	$A_{-2} = A_\omega\sqrt{\big(-J_2(\tau)\big)^2 + \big(-m_a A_\Omega J_1(\tau) + m_a A_\Omega J_3(\tau)\big)^2}$	$\theta_{-2} = \phi_\omega - 2\phi_\Omega - tan^{-1}\left(\frac{-m_a A_\Omega J_1(\tau) + m_a A_\Omega J_3(\tau)}{-J_2(\tau)}\right)$
$\omega \pm (2n+1)\Omega$	$A_{\pm(2n+1)} = A_\omega\sqrt{\big((-1)^n m_a A_\Omega J_{2n}(\tau) + (-1)^{n+1} m_a A_\Omega J_{2n+2}(\tau)\big)^2 + \big((-1)^{n+1} J_{2n+1}(\tau)\big)^2}$	$\theta_{+n} = \phi_\omega \pm (2n+1)\phi_\Omega - tan^{-1}\left(\frac{(-1)^{n+1} J_{2n+1}(\tau)}{(-1)^n m_a A_\Omega J_{2n}(\tau) + (-1)^{n+1} m_a A_\Omega J_{2n+2}(\tau)}\right)$
$\omega \pm 2n\Omega$	$A_{2n} = A_\omega\sqrt{\big((-1)^n J_{2n}(\tau)\big)^2 + \big((-1)^n m_a A_\Omega J_{2n}(\tau) + (-1)^{n+1} m_a A_\Omega J_{2n+2}(\tau)\big)^2}$	$\theta_{+n} = \phi_\omega \pm 2n\theta - tan^{-1}\left(\frac{(-1)^n m_a A_\Omega J_{2n}(\tau) + (-1)^{n+1} m_a A_\Omega J_{2n+2}(\tau)}{(-1)^n J_{2n}(\tau)}\right)$
$\tau = 2m_p A_\Omega$		

Table 2.6: The amplitude and phase shift for different signal components in an amplitude-phase-modulated signal when HF and LF signals are single-tone waveforms, where $\tau = 2m_p A_\Omega$

2.3.6 Amplitude-Frequency-Phase Modulation (AFPM) model

The mathematical description of this model is not presented in reference books and is represented **for the first time** in this dissertation. In this model, the amplitude, frequency, and phase of the HF signal change based on the LF signal, which is illustrated in Equation 2.15, where m_a, m_f, and m_p , like the other models, they quantify the amplitude, frequency, and phase modulations, respectively. This model can be converted to an Amplitude-Phase modulated signal with a new modulation index by using some trigonometric identities illustrated in Equation 2.16. The number of sidebands in this model is also theoretically infinite, as shown in Figure 2.6. Table 2.7 represents the amplitude and phase shift of the amplitude-frequency-phase modulated signal components after replacing $X_\Omega(t)$, defined in Equation 2.6, into Equation 2.15. It is noticeable, that an AFPM model behaves like an AFM or APM model when $m_p = 0$ or $m_f = 0$, respectively.

As evident in Table 2.7, the phase shifts and the amplitude of the signal components vary with the change in the modulation indices (see Figure 2.6b,d), and the amplitude of the corresponding sidebands ($|A_{\pm \mathrm{n}}|$) are **not symmetric** in this model.

$$A_\omega\big(1 + 2m_a g(t)\big)\,cos\left(2\pi f_\omega t + \phi_\omega + 2m_p\, g(t) + 2m_f \int g(t)dt\right) \tag{2.15}$$

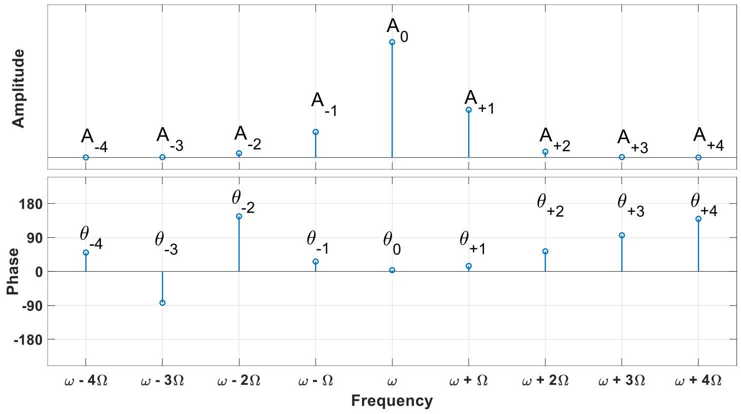

(**a**) An amplitude-frequency-phase modulated (AFPM) signal: the number of sidebands that appear in the frequency domain is theoretically infinite, and the phase shift of the signals changes based on Table 2.7

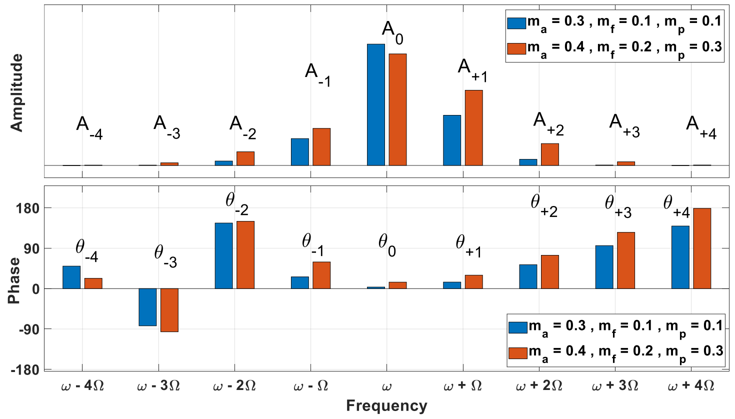

(**b**) phase shifts of the signal components vary with the change in the modulation indices (see Table 2.7)

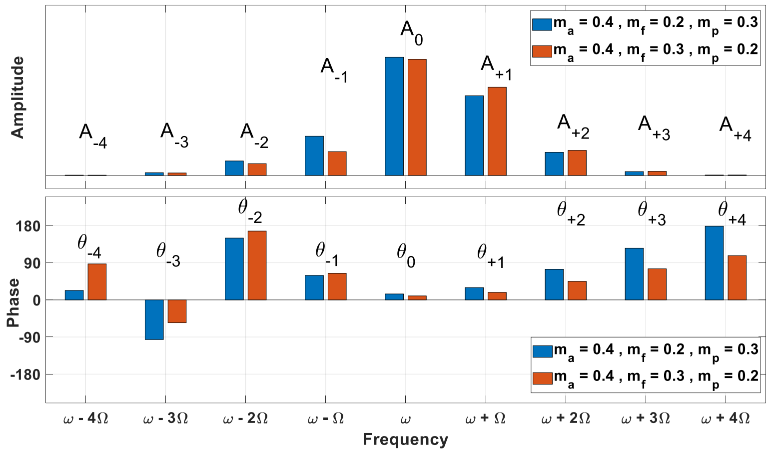

(**c**) amplitudes and phase shifts are different, when

$$m_{a_2} = m_{a_1}$$
$$m_{f_2} = m_{p_1}$$
$$m_{p_2} = m_{f_1}$$

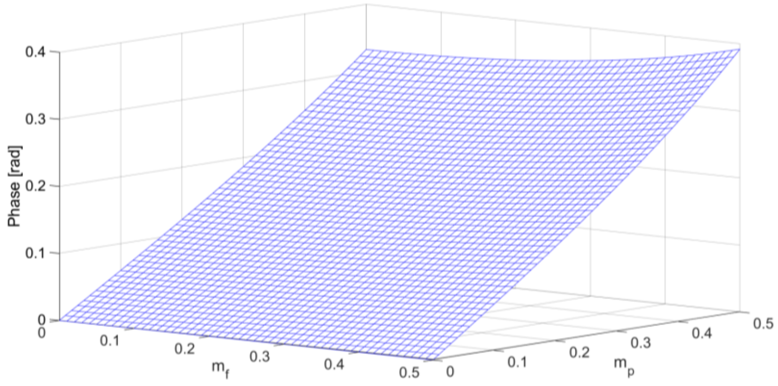

(**d**) a 3D plot of the phase shift of the primary frequency component, θ_0 , when $m_a =$ 0.3 and m_f and m_p vary from 0 to 0.5 (see Table 2.7)

Figure 2.6: The FFT spectrum of a simulated Amplitude-Frequency-Phase Modulated signal using MATLAB

2.3.7 Modulation Indices and Defect Sensitivity

Higher modulation indices typically signify stronger nonlinear interactions, often indicating significant structural defects. Precise quantification of these indices can greatly enhance early-stage defect detection and severity assessment [32, 38-40]. Recently, many researchers have studied the relationship between modulation indices and the presence of defects. Their results experimentally confirmed that modulation indices, such as AMI and FMI, are highly sensitive to the size and location of defects [32, 38-40]. However, it is noticeable that a defect may produce significantly different modulation indices depending on the following circumstances:

- *Effect of Orientation*

  Orientation refers to the angle between the defect and the incident wavefronts. Numerical simulations [102] have shown that when a defect is well-aligned, such that the induced dynamic stresses are perpendicular to the crack face, the opening-closing action is maximized, resulting in strong nonlinear behavior and significant modulation indices. In contrast, when the crack is oriented more parallel to the induced dynamic stresses, the modulation effect weakens significantly [102-104].

$$A_\omega\left(1+2m_aA_\Omega\, cos\left(\Omega t+\phi_\Omega\right)\right) cos\left(\omega t+\phi_\omega+2m_p\, A_\Omega\, cos\left(\Omega t+\phi_\Omega\right)+2m_f\, A_\Omega\, sin\left(\Omega t+\phi_\Omega\right)\right)$$

$$A_\omega\left(1+2m_aA_\Omega\, cos\left(\Omega t+\phi_\Omega\right)\right) cos\left(\omega t+\phi_\omega+2A_\Omega\sqrt{{m_f}^2+{m_p}^2}\; cos\left(\Omega t+\phi_\Omega-tan^{-1}\left(\frac{m_f}{m_p}\right)\right)\right) \tag{2.16}$$

Frequency (rad)	**Amplitude**	**Phase shift**	
ω	$A_0=A_\omega\sqrt{(a_0)^2+(b_0)^2}$	$\theta_0=\phi_\omega-tan^{-1}\left(\frac{b_0}{a_0}\right)$	$a_0=J_0(z)$ $b_0=-2m_aA_\Omega J_1(z)\, cos(\beta)$
$\omega+\Omega$	$A_{+1}=A_\omega\sqrt{(a_{+1})^2+(b_{+1})^2}$	$\theta_{+1}=\phi_\omega+\phi_\Omega-tan^{-1}\left(\frac{b_{+1}}{a_{+1}}\right)$	$a_{+1}=m_aA_\Omega J_0(z)-m_aA_\Omega J_2(z)\, cos(2\beta)+J_1(z)\, sin(\beta)$ $b_{+1}=-m_aA_\Omega J_2(z)\, sin(2\beta)-J_1(z)\, cos(\beta)$
$\omega-\Omega$	$A_{-1}=A_\omega\sqrt{(a_{+1})^2+(b_{+1})^2}$	$\theta_{-1}=\phi_\omega-\phi_\Omega-tan^{-1}\left(\frac{b_{-1}}{a_{-1}}\right)$	$a_{-1}=m_aA_\Omega J_0(z)-m_aA_\Omega J_2(z)\, cos(2\beta)-J_1(z)\, sin(\beta)$ $b_{-1}=m_aA_\Omega J_2(z)\, sin(2\beta)-J_1(z)\, cos(\beta)$
$\omega+2\Omega$	$A_{+2}=A_\omega\sqrt{(a_{+1})^2+(b_{+1})^2}$	$\theta_{+2}=\phi_\omega+2\phi_\Omega-tan^{-1}\left(\frac{b_{+2}}{a_{+2}}\right)$	$a_{+2}=-J_2(z)\, cos(2\beta)+m_aA_\Omega J_1(z)\, sin(\beta)-m_aA_\Omega J_3(z)\, sin(3\beta)$ $b_{+2}=-J_2(z)\, sin(2\beta)-m_aA_\Omega J_1(z)\, cos(\beta)+m_aA_\Omega J_3(z)\, cos(3\beta)$
$\omega-2\Omega$	$A_{-2}=A_\omega\sqrt{(a_{+1})^2+(b_{+1})^2}$	$\theta_{-2}=\phi_\omega-2\phi_\Omega-tan^{-1}\left(\frac{b_{-2}}{a_{-2}}\right)$	$a_{-2}=-J_2(z)\, cos(2\beta)-m_aA_\Omega J_1(z)\, sin(\beta)+m_aA_\Omega J_3(z)\, sin(3\beta)$ $b_{-2}=J_2(z)\, sin(2\beta)-m_aA_\Omega J_1(z)\, cos(\beta)+m_aA_\Omega J_3(z)\, cos(3\beta)$

Table 2.7: The amplitude and phase shift for different signal components in an amplitude-frequency-phase-modulated (AFPM) signal when HF and LF signals are single-tone waveforms, where $z=2A_\Omega\sqrt{{m_f}^2+{m_p}^2}$ and $\beta=tan^{-1}\left(\frac{m_f}{m_p}\right)$

- *Effect of Preload*

Preload refers to static compression, clamping, or residual stress applied to the structure or the defect. Preloading can partially or fully close a defect, reducing or eliminating the breathing motion responsible for modulation. Conversely, the defect behaves as a nonlinear contact interface when the preload condition favors a partially open crack with free surfaces. Research results confirmed that the modulation indices change dramatically when artificial preloads control defect opening, even more than when the defect size is changed [1, 2, 94, 102-105].

- *Effect of Environmental Conditions*

Environmental conditions refer to the structure's temperature and boundary conditions. Temperature changes can affect the material's expansion or contraction, changing the contact stiffness or slightly changing the cracks' breathing condition [45, 46, 106].

- *Excitation Amplitude*

The amplitude of the LF excitation determines how much the crack opens and closes during each cycle, which affects the modulation indices during the test [1, 2, 94].

- *Material nonlinearities unrelated to defects*

Some other sources of nonlinearities, such as intrinsic material nonlinearities, microstructural features, residual stresses, and friction at joints or interfaces, can produce false-positive indications. This situation requires baseline characterization, advanced signal processing techniques, and exciting HF and LF signals at specific modes [37, 39].

2.3.8 Modulation Indices and Defect Detection

Researchers have suggested different parameters to quantify the effect of a defect on the system response. The most popular parameter quantifying modulation is the Damage Modulation Index[1] (DMI), defined by Donskoy [94] and given in Equation 2.17, where $A_{\pm 1,0}$ represent the amplitude of sidebands and the primary frequency defined before [24, 94, 96, 107]. A Damage Index (DI), which is given in Equation 2.18, represents a quantitative parameter used to indicate the presence of a defect in a SUT. The relationship between the DMI and the modulated signal parameters is discussed in subsection 3.1.1.

$$DMI = \frac{A_{+1} + A_{-1}}{2A_0} \tag{2.17}$$

$$DI = \frac{DMI_{defect}}{DMI_{no\ defect}}$$

$$DI_{dB} = \left(DMI_{defect}\right)_{dB} - \left(DMI_{no\ defect}\right)_{dB} \tag{2.18}$$

---

[1] This parameter initially called Modulation Index (MI) by Donskoy, but will be called the **Damage Modulation Index (DMI)**, to avoid overlapping with the signal modulation Index

2.4 Separation of Signal Modulation Indices

As explained in subsection 2.2.1, a source of the nonlinearity on the SUT, such as a crack, modulates the excited signals (HF and LF) and generates sidebands. The DMI can potentially reveal the effect of defect growth in the measured signal [24, 94, 96, 107]. Separating signal modulation indices in VAM can characterize and monitor structural defects [32, 38-40]. One of the traditional methods for estimating the modulation indices is the Hilbert Transform (HT).

The Hilbert transform is a linear operator[1] to construct the analytic signal, $z(t)$, from a real signal, $x(t)$, using Equation 2.19, where $p.v.$ denotes the Cauchy principal value of the integral. The amplitude and phase modulation indices can be calculated using the analytic signal's instantaneous amplitude (IA) and phase (IP) or frequency (IF), which is illustrated in Equation 2.20. While the HT is a linear operator, the IA and IP computations are inherently nonlinear, as represented in Equation 2.21 [108].

$$HT\{x(t)\} = \hat{x}(t) = \frac{1}{\pi}\, p.v. \int_{-\infty}^{+\infty} \frac{x(\tau)}{t-\tau} d\tau$$

$$z(t) = x(t) + j\hat{x}(t) \qquad (2.19)$$

$$z(t) = A(t)e^{j\phi(t)}$$

$$Instantaneous\ amplitude\ (IA){:}\ A(t) = |z(t)| = \sqrt{x^2(t) + \hat{x}^2(t)} \qquad \text{(a)}$$

$$Instantaneous\ Phase\ (IP){:}\ \phi(t) = \measuredangle z(t) = tan^{-1}\left(\frac{\hat{x}(t)}{x(t)}\right) \qquad \text{(b)}$$

$$Instantaneous\ Frequency\ (IF){:}\ f(t) = \frac{1}{2\pi}\frac{d}{dt}\phi(t) \qquad \text{(c)} \qquad (2.20)$$

$$z(t) = z_1(t) + z_2(t)$$

$$|z(t)| = |z_1(t) + z_2(t)| \neq |z_1(t)| + |z_2(t)| \qquad \text{(a)}$$

$$\measuredangle z(t) = tan^{-1}\left(\frac{imag\{z_1(t) + z_2(t)\}}{real\{z_1(t) + z_2(t)\}}\right) \neq \measuredangle z_1(t) + \measuredangle z_2(t) \qquad \text{(b)} \qquad (2.21)$$

Hu et al. [32] used the Hilbert-Huang Transform[2] (HHT) [109] to investigate the amplitude and frequency modulation indices in the VAM method. Their results showed that the amplitude modulation index increased with the crack length, while the frequency modulation index decreased with the crack length [32]. Klepka et al. [40] also used the HT to experimentally investigate modulation types in the VAM response, as represented in Figure 2.7.

---

[1] $HT\{a.x(t) + b.y(t)\} = a.HT\{x(t)\} + b.HT\{y(t)\}$

[2] HHT was introduced by Norden E. Huang and his team in 1998 and consists of two main steps: decomposing Empirical Mode Decomposition (EMD) to decompose a signal into Intrinsic Mode Functions (IMFs), and then using the HT to obtain IA and IF for each IMFs

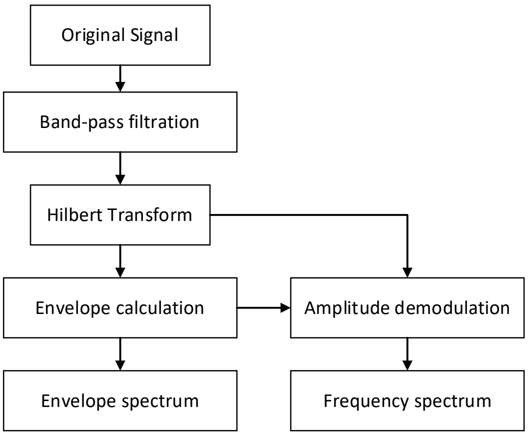

Figure 2.7: The flowchart of the MI separation algorithm using the HT [40]

Donskoy and Ramezani [39] suggested an algorithm to separate amplitude and frequency modulation indices in VAM in 2018. They introduced a Non-Modulated Carrier (NMC), an HF wave part that did not pass through defects and remained non-modulated. The amplitude and phase shift of the NMC are changed due to the wave propagation. Since the modulated signal and NMC have the same primary (carrier) frequency, which is ω, the summation of these signals contaminates the amplitude and the phase shift of the measured signal at the frequency ω. Also, as mentioned in Equation 2.19, HT estimates wrong values for modulation indices in the case of the summation of signals. Therefore, they suggested a time-domain algorithm, the Sweeping-Phase Homodyne Separation (SPHS), to separate the amplitude and frequency modulation indices using the first sidebands (left and right) to avoid using the contaminated carrier frequency, as illustrated in Figure 2.8 [39]. Appendix A illustrates the relationship between the SPHS outputs and the parameters of a modulated signal. Despite the disadvantage of the HT in the presence of an NMC, this method is still used to separate the modulation indices [32, 40].

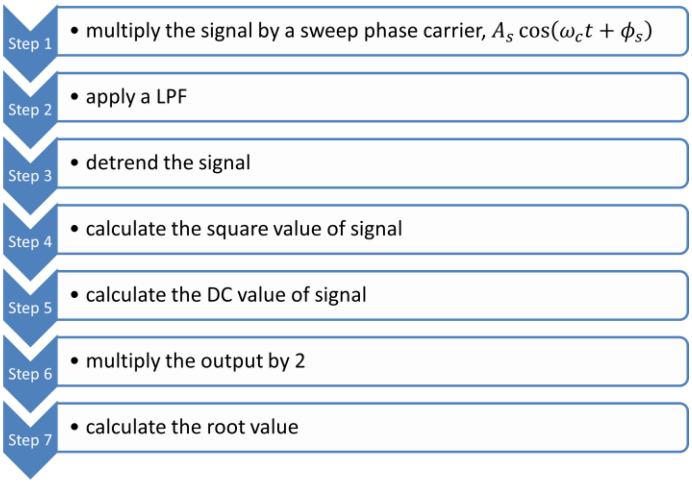

Figure 2.8: The flowchart of the MI separation algorithm using the SPHS algorithm [39]

The results published by Donskoy and Ramezani showed that the SPHS algorithm can successfully separate the amplitude and frequency modulation indices in the presence of an NMC. Their experimental results revealed that the frequency modulation index (FMI) was larger than the amplitude modulation index (AMI) at the earlier stage of the defect. Then, AMI became larger than FMI at the end of a fatigue damage evolution [39].

In 2020, Opperman et al. [41] used both mathematical methods and a short-time Fourier transform (STFT) to estimate amplitude and phase modulation separately. They noted that their results did not confirm that either AM or PM/FM is a reliable index for detecting a defect. Therefore, he suggested that considering both parameters in a combined index significantly improved results.

Despite significant advancements in modulation indices (MIs) and damage detection techniques, the relationship between MIs and damage progression remains unclear and requires further mathematical clarification. Notably, this relationship highly depends on the chosen signal model and its parameters. In this study, we aimed to mathematically enhance existing separation algorithms and to propose a comprehensive model that integrates amplitude, frequency, and phase modulation simultaneously.

2.5 Defect Localization

Defect localization is a crucial field in SHM, aiming to identify and precisely locate structural defects. Lamb wave-based methods have garnered significant attention due to their sensitivity to minor defects, their potential for early detection, and their ability to efficiently examine large areas in thin structures such as plates and shells [4, 14, 81].

An actuator, such as a piezoelectric or a shaker, or a combination of piezoelectric sensors, applies a single tone burst Lamb wave[1] at a specific frequency, and the signal is measured simultaneously using one or more receivers. A defect localization algorithm tracks the reflection part of the propagation signal from a defect and locates the source of the reflection using a damage imaging method [42-70]. This research aims not to identify or compare all damage imaging methods, so the following subsection explains only the Delay and Sum (DAS) damage imaging method used in this research.

2.5.1 Delay and Sum Damage Imaging Method

Delay-and-Sum (DAS) is a well-established imaging algorithm that has been modified by Michaels [43, 44] and used extensively in structural health monitoring (SHM) for the localization and visualization of damage in structures [43, 44, 110, 111]. DAS uses differences in arrival times of elastic or ultrasonic waves, typically Lamb waves, captured by sensor arrays mounted on structural surfaces. When an ultrasonic wave interacts with damage, such as cracks, scattered wave components propagate toward sensor arrays [81]. DAS involves shifting sensor signals by calculated time delays corresponding to the wave propagation distances from assumed damage locations. These adjusted signals are then summed coherently across the sensor array. Areas with actual defects exhibit constructive interference, resulting in pronounced amplitude peaks on generated damage maps, clearly indicating defect positions [43, 44].

Imagine that a lamb wave tone burst was excited by a piezoelectric sensor, which is called a sender or actuator, at coordinates (x_s, y_s), and propagates radially within the 2D-plate sample with the group velocity c_g, as illustrated in Figure 2.9a. The signal reaches a defect located at the coordinates (x_D, y_D) after time t_{sD}, as assessed by Equation 2.22a. The signal will be scattered by the defect and propagate radially with the same group velocity, as shown

---

[1] See subsection 2.3.2

in Figure 2.9b. This scattered signal reaches the first receiver located at the coordinates (x_{r1}, y_{r1}) after a time interval t_{Dr1}, assessed in Equation 2.22b. The total time interval t_{sDr1} during which the signal propagates along the path from the sender (or actuator) to the defect, and the receiver is provided by Equation 2.22c and illustrated in Figure 2.9c.

The locus of all potential points with the coordinates (x, y) that have the same time interval, t_{sDr1}, or spatial distance from the sender and the first receiver, are points that lie on an ellipse with the (x_s, y_s) and (x_{r1}, y_{r1}) as its foci, as represented in Equation 2.22d and Figure 2.9d. The location of a defect will be detected using a minimum of three pairs of the sender-receiver [110], as shown in Figure 2.10.

$$t_{sD} = \frac{d_{sD}}{c_g} = \frac{\sqrt{(x_S - x_D)^2 + (y_S - y_D)^2}}{c_g} \qquad \text{(a)}$$

$$t_{Dr1} = \frac{d_{Dr1}}{c_g} = \frac{\sqrt{(x_D - x_{r1})^2 + (y_D - y_{r1})^2}}{c_g} \qquad \text{(b)}$$

$$t_{sDr1} = \frac{d_{sD} + d_{Dr1}}{c_g} = \frac{\sqrt{(x_S - x_D)^2 + (y_S - y_D)^2} + \sqrt{(x_D - x_{r1})^2 + (y_D - y_{r1})^2}}{c_g} \qquad \text{(c)}$$

$$t_{sDr1} = \frac{d_{sx} + d_{xr1}}{c_g} = \frac{\sqrt{(x_S - x)^2 + (y_S - y)^2} + \sqrt{(x - x_{r1})^2 + (y - y_{r1})^2}}{c_g} \qquad \text{(d)} \qquad (2.22)$$

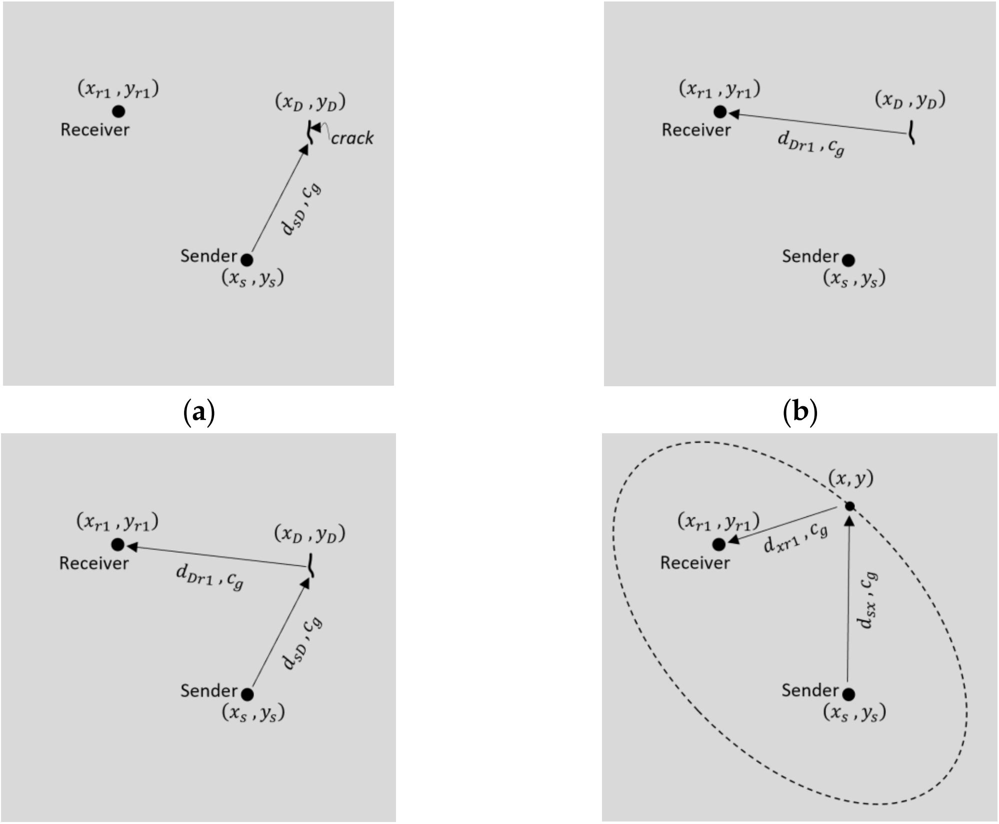

(a) (b) (c) (d)

Figure 2.9: Visualization of the time interval between source, defect, and receiver; (**a**) from the source to the defect after t_{sD}; (**b**) from the defect to the receiver after t_{Dr1}; (**c**) from the source to the receiver after t_{sDr1}; (**d**) the locus of all potential points with the coordinates (x, y) that have the same time interval equal to t_{sDr1}

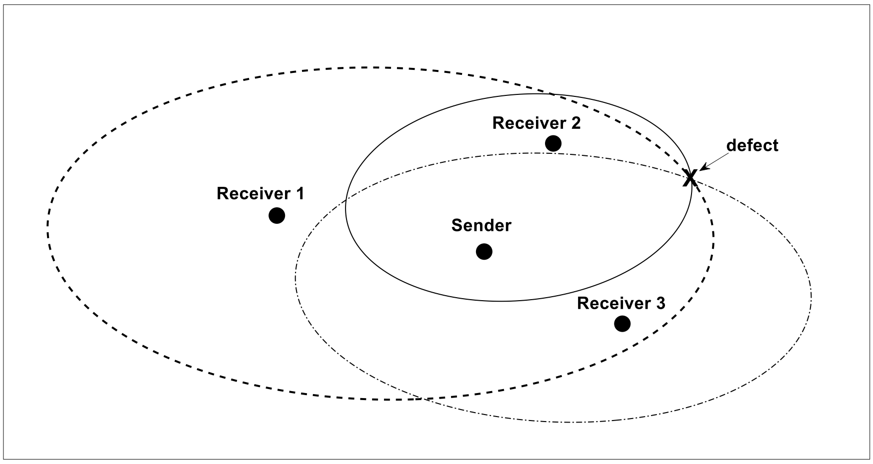

Figure 2.10: Localizing a defect using three pairs of sender-receiver

2.5.2 Boundary Reflected Signal

When a tone burst signal is excited through a piezoelectric sensor on a sample, the elastic wave propagates radially and is eventually reflected by boundaries. Therefore, receivers sense not only the first-arrived signal but also several reflected signals caused by the boundaries. Typically, the first arrived signal is used for localization. One method to avoid the unwanted reflected part is to multiply the measured signal by a boundary coefficient, $z(t)$, when the reflected signals do not overlap with the first-arrived signal[1].

The time required, t_{ij}, for the first reflected signal by the jth edge to reach a receiver can be calculated easily by assuming a mirror sender (actuator) at the jth edge, as illustrated in Figure 2.11 and Equation 2.23, where i and j referring to the receiver number and the edge number, respectively [52].

$$t_{ij} = \frac{D_{ij}}{c_g} \tag{2.23}$$

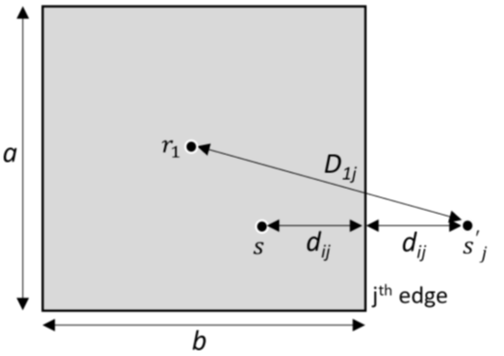

Figure 2.11: The path, D_{1j}, that the first reflected signal from the jth edge reaches the first receiver. s'_j represents the mirror sender at the jth edge [52]

After calculating the t_{ij} for i^{th}receiver and all edges, the measured signal by the i^{th} receiver multiplies by a boundary coefficient, $z(t)$. The boundary coefficient can be defined in different ways. Equations 2.24 and 2.25 represent two different boundary coefficients that can be used

---

[1] First arrived signal and the reflected signal overlap when both sender and receiver are too close to an edge, or when the tone burst signal is too wide in the time domain

to reduce the effect of the reflected signal from boundaries where $t_{km} = min\{t_{kj}\}$ and t_{kj} is the time the wave propagates from the actuator, being reflected at the j^th^ edge, and arriving at the k^{th} receiver [52]. In Equation 2.25, $\alpha = 1{\sim}4$ is the wave reflection strength coefficient, and a and b refer to the side lengths [52]. It is worth mentioning that the boundary coefficient represented in Equation 2.24 has bigger side lobes in the frequency domain because of the sudden jump in the time domain, and changes the frequency representation of the measured signal after multiplication[1]. Figure 2.12 shows a sample of the boundary coefficient in the time domain. The localization algorithm provided in this study is introduced in the next chapter.

$$z_k(t) = \begin{cases} 1 & t \leq t_{km} \\ 0 & t > t_{km} \end{cases} \tag{2.24}$$

$$z_k(t) = \begin{cases} 1 & t \leq t_{km} \\ e^{-\frac{\alpha t}{t_{kj}-t_{km}} + \frac{\alpha t_{km}}{t_0 - t_{km}}} & t_{km} < t < t_0 \end{cases} \quad , \quad t_0 = \frac{a+b}{c_g} \tag{2.25}$$

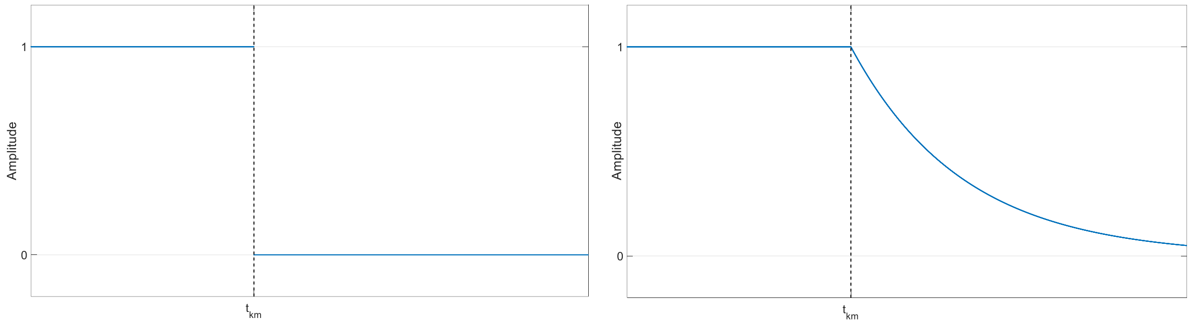

(a) (b)

Figure 2.12: A sample of the boundary coefficient, simulated in MATLAB; (a) function represented in Equation 2.24; (b) function represented in Equation 2.25

2.6 Chapter Summary

In this chapter, in addition to an overview of fundamental concepts relevant to defect detection and localization using the vibro-asoustic modulation, various combined modulation models are introduced mathematically to facilitate a better understanding of modulation index separation. The points discussed in this chapter can be categorized as follows:

- Different modulation models are described mathematically and numerically to illustrate the influence of the modulation indices (MIs) on amplitude and phase shift at different frequencies.
- An AFPM model is described mathematically in this chapter for the first time.
- A change in signal phase shifts due to MI variation is predicted in the AFPM model. The following chapter introduces the phase shift extraction method, theoretically, and the experimental results will be represented in Chapter 4.
- A general damage localization technique using a DAS damage imaging method is introduced.

---

[1] $\mathcal{F}\{x_1(t) \times x_2(t)\} = \mathcal{F}\{x_1(t)\} * \mathcal{F}\{x_2(t)\}$, where $*$ is the convolution operator

Chapter 3

Methodology

This chapter presents the research goals and methodology. In the first part of the chapter, the problem of separating modulation indices will be addressed. To this end, the mathematical relationship between the parameters of the modulated signal (amplitudes and phase shifts) and the modulation indices will be examined. Then, an algorithm for accurately separating these indices will be introduced. The phase shifts of different sidebands for both AFM and AFPM models are explained and compared in this chapter. Furthermore, the relative sensitivity of the phase shifts and damaged modulation index is investigated theoretically and numerically. The required equations for the AFM and AFPM models are represented earlier in subsections 2.3.4 and 2.3.6, respectively.

In the second part, a theoretical introduction to localization using the VAM technique is provided. First, the approach to both high- and low-frequency selection, as well as the correction of the boundary reflected signal, is explained. A brief introduction to the STFT algorithm for first-sideband extraction is forthcoming. Ultimately, the DAS damage imaging method based on the first sideband is discussed, and the flowchart of the localization algorithm is presented.

3.1 Separation of Modulation Indices

In this section, the MIs separation is addressed by introducing clearly defined mathematical relationships. The choice of modulation models is based on their ability to accurately describe the nonlinear interactions within the structure. As discussed, a combination of amplitude modulation with frequency or phase modulation was discovered in the VAM method [32, 39-41]; therefore, the AFM model is selected due to its widespread use and simplicity. In contrast, the AFPM model is developed to overcome limitations observed experimentally in phase shift behaviors, providing a more accurate representation of real experimental conditions.

Therefore, a proper modulation model for VAM can be a combination of amplitude modulation with at least one of the frequency or phase modulation; other modulation models will not be discussed in this section.

3.1.1 Damage MI[1] and AFM[2]

The relationship between the damage modulation index, defined in Equation 2.17, and the parameters of the modulated signal, listed in Table 2.5, is represented in Equation 3.1, where $g = 2m_f A_\Omega$.

---

[1] see subsection 2.3.8

[2] see subsection 2.3.4

$$DMI = \frac{A_{+1} + A_{-1}}{2A_0}$$

$$DMI = A_\omega \frac{\left(J_1(g) + m_a A_\Omega J_0(g) + m_a A_\Omega J_2(g)\right) + \left(-J_1(g) + m_a A_\Omega J_0(g) + m_a A_\Omega J_2(g)\right)}{2A_\omega J_0(g)}$$

$$DMI = \frac{2A_\omega\left(m_a A_\Omega J_0(g) + m_a A_\Omega J_2(g)\right)}{2A_\omega J_0(g)}$$

$$DMI = m_a A_\Omega \left(1 + \frac{J_2\left(2m_f A_\Omega\right)}{J_0\left(2m_f A_\Omega\right)}\right) \tag{3.1}$$

The following inferences can be derived from Equation 3.1:

- Equation 3.1 is not valid in the presence of an NMC[1].
- The DMI is equal to $m_a A_\Omega$ when $\frac{J_2(2m_f A_\Omega)}{J_0(2m_f A_\Omega)} \cong 0$. This relationship reveals that the DMI mainly shows the behavior of the $m_a A_\Omega$.
- The DMI is related to the multiplication of the LF signal amplitude, A_Ω, and the AM index, m_a. Therefore, DMI plots in dB for two test setups with different LF signal amplitudes will be almost parallel.

3.1.2 MI Separation using Simplification in the AFM Model

A method for MI separation that is used by some research teams is to substitute an approximation of the Bessel functions and simplify the equations, when the value of the $m_f A_\Omega$ is assumed to be very small [32, 39]. The approximated Bessel functions can be written as Equation 3.2, and the simplified amplitude of sidebands is listed in Table 3.1.

$$J_0\left(2m_f A_\Omega\right) \cong 1 \qquad \text{(a)}$$

$$J_1\left(2m_f A_\Omega\right) \cong m_f A_\Omega \qquad \text{(b)}$$

$$J_{n\geq 2}\left(2m_f A_\Omega\right) \cong 0 \qquad \text{(c)} \qquad (3.2)$$

Frequency (rad)	Amplitude	Phase shift
ω	$A_0 = A_\omega$	$\theta_0 = \phi_\omega$
$\omega + \Omega$	$A_{+1} = A_\omega A_\Omega\left(m_a + m_f\right)$	$\theta_{+1} = \phi_\omega + \phi_\Omega$
$\omega - \Omega$	$A_{-1} = A_\omega A_\Omega\left(m_a - m_f\right)$	$\theta_{-1} = \phi_\omega - \phi_\Omega$
$\omega + 2\Omega$	$A_{+2} = +A_\omega {A_\Omega}^2\left(m_a m_f\right)$	$\theta_{+2} = \phi_\omega + 2\phi_\Omega$
$\omega - 2\Omega$	$A_{-2} = -A_\omega {A_\Omega}^2\left(m_a m_f\right)$	$\theta_{-2} = \phi_\omega - 2\phi_\Omega$
$\omega \pm n\Omega$	$A_{\pm n\geq 3} = 0$	

Table 3.1: The simplified amplitude for different signal components in the AFM model

---

[1] NMC changes the amplitude of the signal at the carrier frequency, and the final DMI is not calculated as represented in Equation 3.1 (see subsection 2.4)

The above approximation helps us to calculate the value of m_a and m_f using the SPHS[1], which is given in Equation 3.3, or using the mathematical relationships represented in Equation 3.4.

$$\begin{aligned} SPHS_{max} &= A_\omega A_\Omega A_s m_a \\ SPHS_{min} &= A_\omega A_\Omega A_s m_f \end{aligned} \tag{3.3}$$

$$\begin{aligned} \frac{A_{+1}+A_{-1}}{2A_0} &= \frac{A_\omega A_\Omega(m_a+m_f)+A_\omega A_\Omega(m_a-m_f)}{2A_\omega} = A_\Omega m_a \\ \frac{A_{+1}-A_{-1}}{2A_0} &= \frac{A_\omega A_\Omega(m_a+m_f)-A_\omega A_\Omega(m_a-m_f)}{2A_\omega} = A_\Omega m_f \end{aligned} \tag{3.4}$$

Despite the simplicity of MI separation in this situation, this approximation can not describe the other sidebands correctly. As is evident, the second sideband is approximated to be symmetric, which is not the case experimentally. Furthermore, the third and further sidebands are supposed to be zero by this approximation; however, in practical tests, the amplitude of these sidebands is not zero, as shown in Figure 3.1.

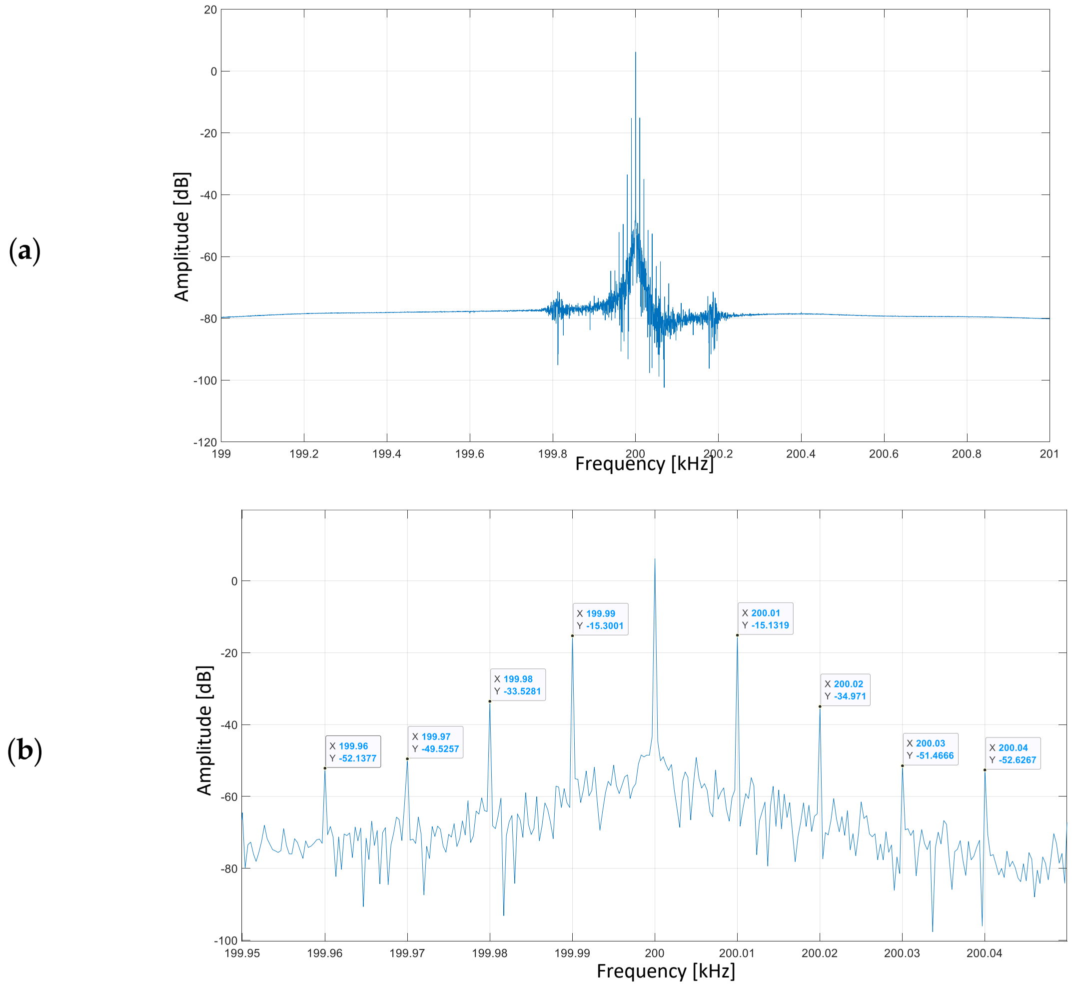

Figure 3.1: The FFT spectrum of an experimental result when $f_\omega = 200\ kHz$ and $f_\Omega = 10\ Hz$; (**a**) broad view; (**b**) zoomed view

---

[1] See Appendix A

3.1.3 MI Separation Using Advanced Simplification

As mentioned, the amplitude of the measured signal at frequency ω, A_0, can not be trusted when an NMC exists in the measured signal. A better approach is to develop an algorithm to avoid using the value of A_0. Therefore, the first and second sidebands are used for the separation technique in this algorithm. The summation and subtraction of the first and second sidebands are given in Equations 3.5 to 3.8, where $g = 2m_f A_\Omega$.

$$|A_{+1}| + |A_{-1}| =$$

$$A_\omega |J_1(g) + m_a A_\Omega J_0(g) + m_a A_\Omega J_2(g)| + A_\omega |-J_1(g) + m_a A_\Omega J_0(g) + m_a A_\Omega J_2(g)|$$

$$2A_\omega \left(m_a A_\Omega J_0(2m_f A_\Omega) + m_a A_\Omega J_2(2m_f A_\Omega)\right) \tag{3.5}$$

$$|A_{+1}| - |A_{-1}| =$$

$$A_\omega |J_1(g) + m_a A_\Omega J_0(g) + m_a A_\Omega J_2(g)| - A_\omega |-J_1(g) + m_a A_\Omega J_0(g) + m_a A_\Omega J_2(g)|$$

$$2A_\omega J_1(2m_f A_\Omega) \tag{3.6}$$

$$|A_{+2}| + |A_{-2}| =$$

$$A_\omega |J_2(g) + m_a A_\Omega J_1(g) + m_a A_\Omega J_3(g)| + A_\omega |J_2(g) - m_a A_\Omega J_1(g) - m_a A_\Omega J_3(g)|$$

$$2A_\omega J_2(2m_f A_\Omega) \tag{3.7}$$

$$|A_{+2}| - |A_{-2}| =$$

$$A_\omega |J_2(g) + m_a A_\Omega J_1(g) + m_a A_\Omega J_3(g)| - A_\omega |J_2(g) - m_a A_\Omega J_1(g) - m_a A_\Omega J_3(g)|$$

$$2A_\omega \left(m_a A_\Omega J_1(2m_f A_\Omega) + m_a A_\Omega J_3(2m_f A_\Omega)\right) \tag{3.8}$$

It needs to be mentioned that in the above equation, $A_{-1}$and A_{-2} are assumed to be positive[1]. The sign of FFT-evaluated amplitudes is always positive, and the amplitude's sign must be calculated using the phase shift of the frequency component. Notice the phase shifts of the HF and LF signals (ϕ_ω and ϕ_Ω) are also arbitrary. The summation of the first and second sideband phase shifts can delete the phase shift of the LF signal and reveal the sign of the left-side sidebands, as given in Equations 3.9 and 3.10 (see Table 2.5 or 2.7). As is evident in Equations 3.9 and 3.10, the value of the phase shift is equal to π when θ_{-1} or θ_{-2} has additional π phase shift because of the negativity, otherwise, the final value is 0. When the value of a left-side sideband is negative, the value of the summation and subtraction must be switched in the above equations.

---

[1] A_{-1} is negative, when $m_a < m_f$

$$\theta_{+1}+\theta_{-1}-2\theta_0=$$

$$(\phi_\omega+\phi_\Omega)+(\phi_\omega-\phi_\Omega)-2(\phi_\omega) \tag{3.9}$$

$$\theta_{+2}+\theta_{-2}-2\theta_0=$$

$$(\phi_\omega+2\phi_\Omega)+(\phi_\omega-2\phi_\Omega)-2(\phi_\omega) \tag{3.10}$$

The goal of the MI separation is to evaluate the value of m_a, m_f using the above equations. It is noticeable that the above equations clearly show that the output of the separation algorithm is the product of a modulation index ($m_a$or m_f) and A_Ω, rather than the index alone. Additionally, the amplitude of the HF signal, A_ω, is an unknown variable. The ratio of the above equations can lead us to new relationships, which are A_ω independence. Different ratios of summations and subtractions of sideband amplitudes are given in Equations 3.11 - 16. The value of the m_aA_Ω and m_fA_Ω can be calculated using a combination of the two following ratios.

$$AR_{12PP}\equiv\frac{|A_{+1}|+|A_{-1}|}{|A_{+2}|+|A_{-2}|}= \tag{3.11}$$

$$\frac{2A_\omega\big(m_aA_\Omega J_0(g)+m_aA_\Omega J_2(g)\big)}{2A_\omega J_2(g)}$$

$$m_aA_\Omega\frac{J_0\big(2m_fA_\Omega\big)+J_2\big(2m_fA_\Omega\big)}{J_2\big(2m_fA_\Omega\big)}$$

$$AR_{12PN}\equiv\frac{|A_{+1}|+|A_{-1}|}{|A_{+2}|-|A_{-2}|}= \tag{3.12}$$

$$\frac{2A_\omega\big(m_aA_\Omega J_0(g)+m_aA_\Omega J_2(g)\big)}{2A_\omega\big(m_aA_\Omega J_1(g)+m_aA_\Omega J_3(g)\big)}$$

$$\frac{J_0\big(2m_fA_\Omega\big)+J_2\big(2m_fA_\Omega\big)}{J_1\big(2m_fA_\Omega\big)+J_3\big(2m_fA_\Omega\big)}$$

$$AR_{12NP}\equiv\frac{|A_{+1}|-|A_{-1}|}{|A_{+2}|+|A_{-2}|}= \tag{3.13}$$

$$\frac{2A_\omega J_1(g)}{2A_\omega J_2(g)}$$

$$\frac{J_1\big(2m_fA_\Omega\big)}{J_2\big(2m_fA_\Omega\big)}$$

$$AR_{12NN}\equiv\frac{|A_{+1}|-|A_{-1}|}{|A_{+2}|-|A_{-2}|}= \tag{3.14}$$

$$\frac{2A_\omega J_1(g)}{2A_\omega\big(m_aA_\Omega J_1(g)+m_aA_\Omega J_3(g)\big)}$$

$$\frac{1}{m_aA_\Omega}\frac{J_1\big(2m_fA_\Omega\big)}{J_1\big(2m_fA_\Omega\big)+J_3\big(2m_fA_\Omega\big)}$$

$$AR_{11PN} \equiv \frac{|A_{+1}| + |A_{-1}|}{|A_{+1}| - |A_{-1}|} = \tag{3.15}$$

$$\frac{2A_{\omega}\left(m_a A_{\Omega} J_0(g) + m_a A_{\Omega} J_2(g)\right)}{2A_{\omega} J_1(g)}$$

$$m_a A_{\Omega} \frac{J_0\left(2m_f A_{\Omega}\right) + J_2\left(2m_f A_{\Omega}\right)}{J_1\left(2m_f A_{\Omega}\right)}$$

$$AR_{22PN} \equiv \frac{|A_{+2}| + |A_{-2}|}{|A_{+2}| - |A_{-2}|} = \tag{3.16}$$

$$\frac{2A_{\omega} J_2\left(2m_f A_{\Omega}\right)}{2A_{\omega}\left(m_a A_{\Omega} J_1\left(2m_f A_{\Omega}\right) + m_a A_{\Omega} J_3\left(2m_f A_{\Omega}\right)\right)}$$

$$\frac{1}{m_a A_{\Omega}} \frac{J_2\left(2m_f A_{\Omega}\right)}{J_1\left(2m_f A_{\Omega}\right) + J_3\left(2m_f A_{\Omega}\right)}$$

For the next step, a few terms of the Bessel function expansion are considered to approximate the function, while the remaining terms are neglected due to their diminishing magnitude[1]. The approximation of the Bessel functions is listed in Equation 3.17. Equations 3.18 to 3.21 represent the results of substituting Equation 3.17 into Equations 3.5 to 3.8. The separation algorithm, as represented by the final equations, is illustrated in Figure 3.2.

$$\begin{aligned}
J_0(g) &= \left(1 - \frac{g^2}{4}\right) && \text{(a)} \\
J_1(g) &= \left(\frac{g}{2} - \frac{g^3}{16}\right) && \text{(b)} \\
J_2(g) &= \left(\frac{g^2}{8} - \frac{g^4}{96}\right) && \text{(c)} \\
J_3(g) &= \left(\frac{g^3}{48} - \frac{g^5}{768}\right) && \text{(d)}
\end{aligned} \tag{3.17}$$

$$A_{1P} = |A_{+1}| + |A_{-1}| = 2m_a A_{\Omega} - m_a A_{\Omega}\left(m_f A_{\Omega}\right)^2 - \frac{1}{3} m_a A_{\Omega}\left(m_f A_{\Omega}\right)^4 \tag{3.18}$$

$$A_{1N} = |A_{+1}| - |A_{-1}| = 2m_f A_{\Omega} - \left(m_f A_{\Omega}\right)^3 \tag{3.19}$$

$$A_{2P} = |A_{+2}| + |A_{-2}| = \left(m_f A_{\Omega}\right)^2 - \frac{1}{3}\left(m_f A_{\Omega}\right)^4 \tag{3.20}$$

$$A_{2N} = |A_{+2}| - |A_{-2}| = 2\left(m_a A_{\Omega}\right)\left(m_f A_{\Omega}\right) - \frac{2}{3} m_a A_{\Omega}\left(m_f A_{\Omega}\right)^3 - \frac{1}{12} m_a A_{\Omega}\left(m_f A_{\Omega}\right)^5 \tag{3.21}$$

---

[1] All terms including a $g^{m>5}$ assumed to be zero in $J_n(g)$

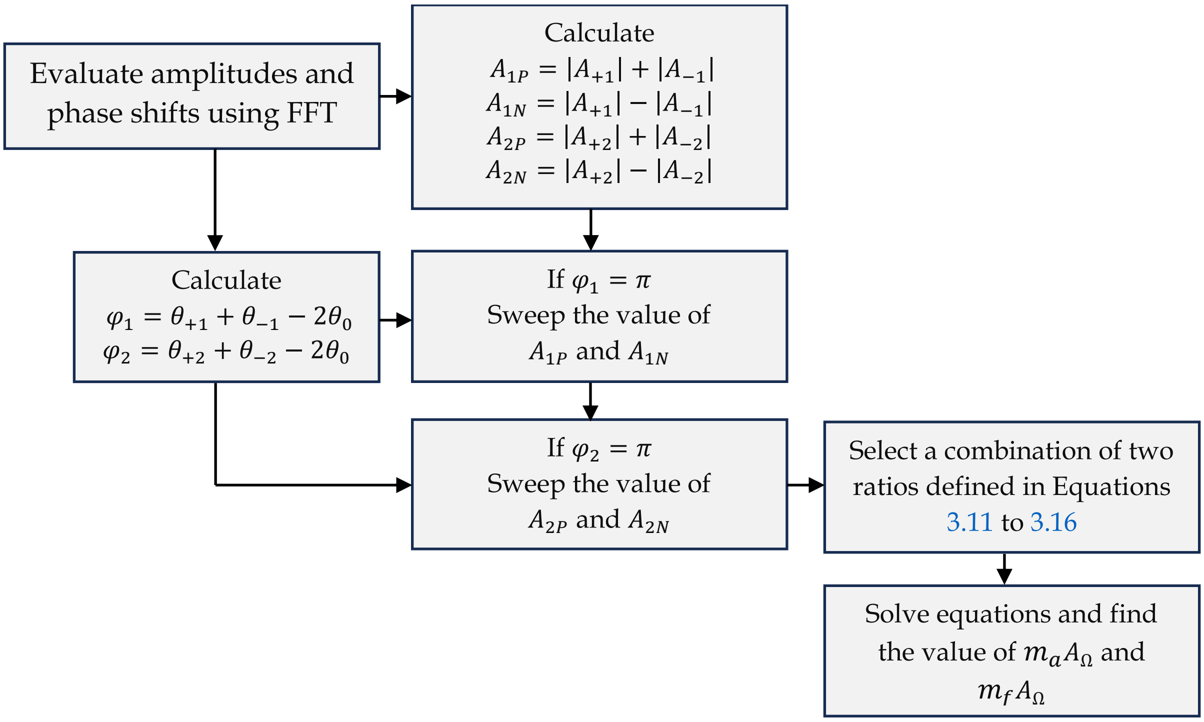

Figure 3.2: The flowchart of the MI separation algorithm for the AFM model

To assess the robustness and accuracy of the presented advanced simplification, the algorithm has been numerically simulated in MATLAB to confirm the MI separation. An AFM signal was generated in MATLAB using the parameters listed in Table 3.2. Results confirm that this algorithm can accurately separate MIs. This algorithm has been tested with 100 different parameter combinations, and the results are presented in Figure 3.3.

Parameter	**Value**
A_ω	$1 < rand^1 < 1.5$ v
A_Ω	1 v
A_{NM}	$0 < rand < 0.3$ v
m_a	$0 < rand < 0.2$
m_f	$0 < rand < 0.2$
f_ω	200 kHz
f_Ω	500 Hz
ϕ_ω	$0 < rand < 2\pi$
ϕ_Ω	$0 < rand < 2\pi$

Table 3.2: The value of parameters used in the MATLAB simulation of the MI separation algorithm for an AFM signal

---

[1] The rand here means that the value of that parameter is selected randomly

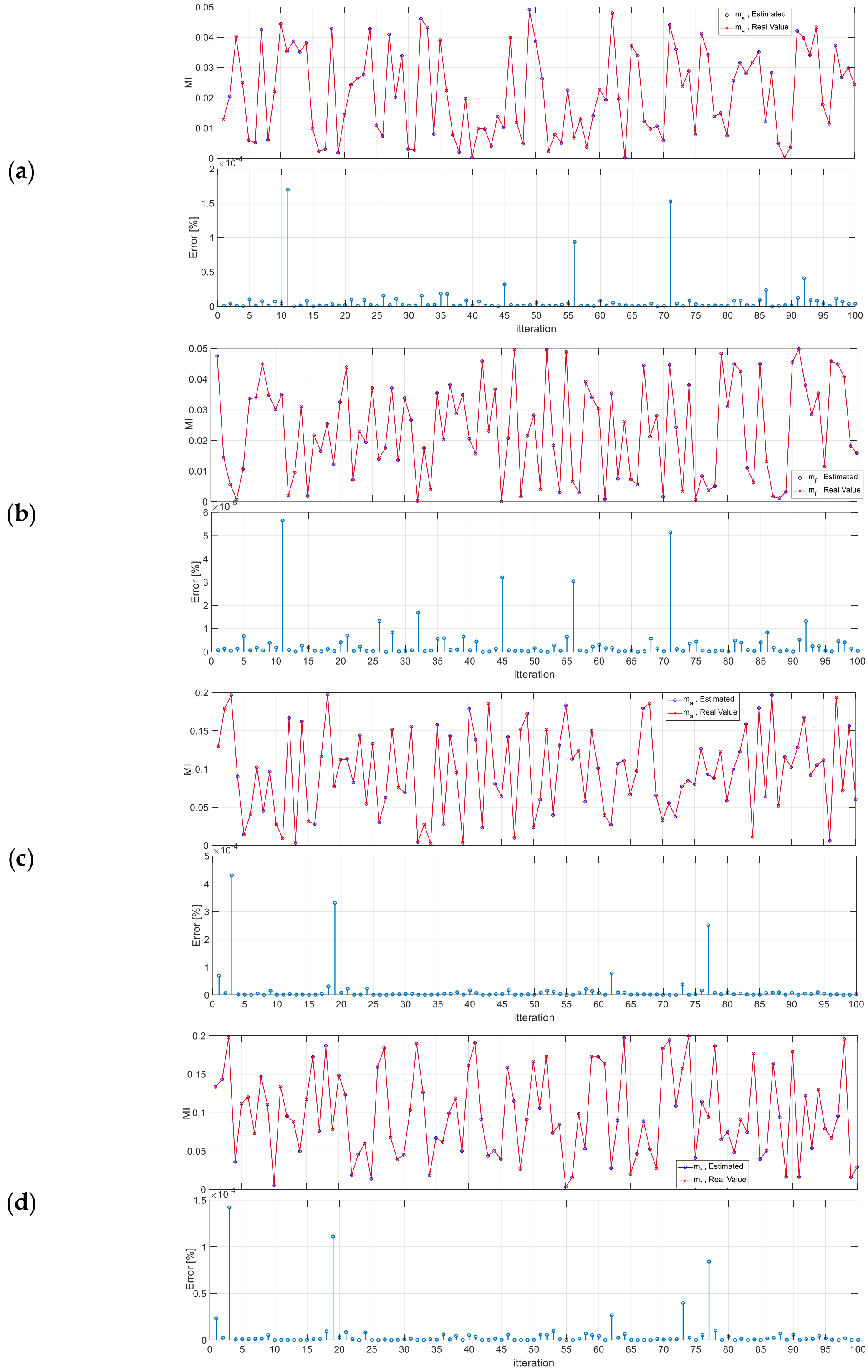

Figure 3.3: Numerical results of the MI separation algorithm using MATLAB for an AFM signal; (**a**,**b**) the actual, estimated value and the estimation error when the simulated MI are smaller than 0.05; (**c**,**d**) the actual, estimated value and the estimation error when the simulated MI are smaller than 0.2

3.1.4 MI Separation Using an Advanced Modulation Model

Recent separation methods have focused on separating the amplitude and frequency modulation indices [32, 39, 40]. The introduction of the AFPM model is motivated by its ability to not only include all three kinds of modulation but also to predict the change in phase shift due to MI variation. The AFPM model incorporates amplitude, frequency, and phase modulations simultaneously, providing a richer theoretical framework that aligns closely with experimental data and offers enhanced accuracy in modulation index estimation. This subsection discusses theoretically a separation algorithm for an AFPM model, using the parameters listed in Table 2.7.

3.1.4.1 The phase shifts in an AFM and AFPM model

Apart from the complexity of the phase shifts illustrated in Tables 2.5 and 2.7, all signal components in the AFPM model have an additional phase shift related to the modulation indices. For a better observation, Table 3.3 illustrates the phase shifts for both AFM and AFPM.

Frequency	AFM model	AFPM model
ω	ϕ_ω	$\phi_\omega - tan^{-1}\left(\frac{-2m_aA_\Omega J_1(z)\,cos(\beta)}{J_0(z)}\right)$
$\omega + \Omega$	$\phi_\omega + \phi_\Omega$	$\phi_\omega + \phi_\Omega - tan^{-1}\left(\frac{-m_aA_\Omega J_2(z)\,sin(2\beta) - J_1(z)\,cos(\beta)}{m_aA_\Omega J_0(z) - m_aA_\Omega J_2(z)\,cos(2\beta) + J_1(z)\,sin(\beta)}\right)$
$\omega - \Omega$	$\phi_\omega - \phi_\Omega$	$\phi_\omega - \phi_\Omega - tan^{-1}\left(\frac{m_aA_\Omega J_2(z)\,sin(2\beta) - J_1(z)\,cos(\beta)}{m_aA_\Omega J_0(z) - m_aA_\Omega J_2(z)\,cos(2\beta) - J_1(z)\,sin(\beta)}\right)$
$\omega + 2\Omega$	$\phi_\omega + 2\phi_\Omega$	$\phi_\omega + 2\phi_\Omega - tan^{-1}\left(\frac{-J_2(z)\,sin(2\beta) - m_aA_\Omega J_1(z)\,cos(\beta) + m_aA_\Omega J_3(z)\,cos(3\beta)}{-J_2(z)\,cos(2\beta) + m_aA_\Omega J_1(z)\,sin(\beta) - m_aA_\Omega J_3(z)\,sin(3\beta)}\right)$
$\omega - 2\Omega$	$\phi_\omega - 2\phi_\Omega$	$\phi_\omega - 2\phi_\Omega - tan^{-1}\left(\frac{J_2(z)\,sin(2\beta) - m_aA_\Omega J_1(z)\,cos(\beta) + m_aA_\Omega J_3(z)\,cos(3\beta)}{-J_2(z)\,cos(2\beta) - m_aA_\Omega J_1(z)\,sin(\beta) + m_aA_\Omega J_3(z)\,sin(3\beta)}\right)$
$z = 2A_\Omega\sqrt{{m_f}^2 + {m_p}^2} \quad and \quad \beta = tan^{-1}\left(\frac{m_f}{m_p}\right)$		

Table 3.3: The phase shifts of different components for an AFM and AFPM model

Regarding the relationships in Table 3.3, the phase shift of all components for AFM remains constant with changes in m_a or m_f. However, all phase shifts in AFPM vary with changes in modulation indices. Figure 3.4 shows 3D plots of the phase shift of a MATLAB-simulated signal at the primary frequency, ϕ_ω, for both AFM and AFPM models. Theoretically and numerically, the phase shifts in the AFM model do not change with a change in MIs (see Table 2.5); however, all phase shifts in the AFPM model change with a change in MIs. Accordingly, phase shift variations corresponding to modulation parameter changes can be employed to identify the AFPM model[1].

---

[1] see subsection 4.2.2.1

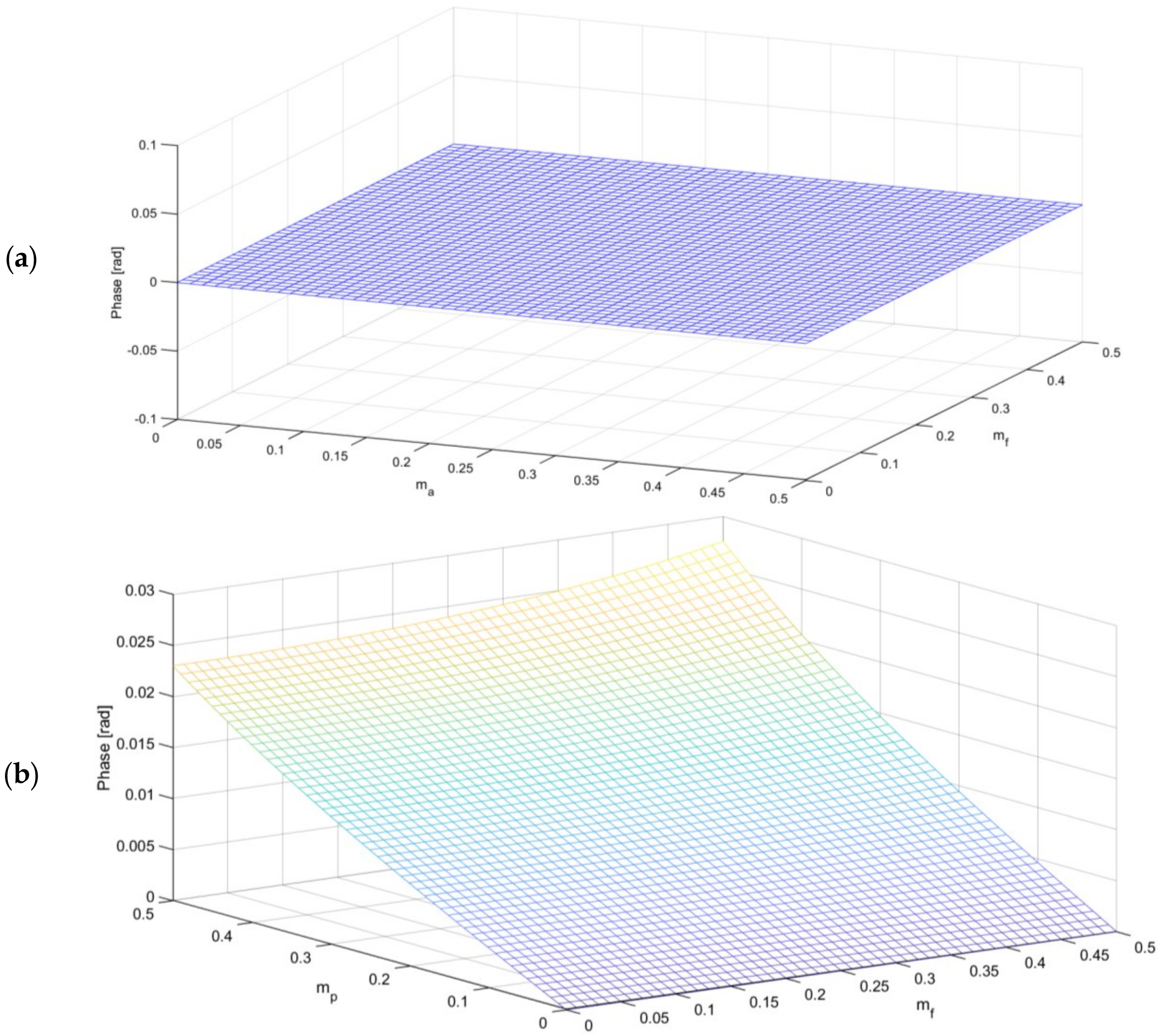

Figure 3.4: The 3D plot of the phase shift at frequency ω, where the initial phase shifts are set to ϕ_ω, $\phi_\Omega = 0$; (**a**) an AFM simulated signal; (**b**) an AFPM simulated signal for a constant $m_a = 0.02$

3.1.4.2 Relative Sensitivity of the DMI and Phase Shifts

As discussed before, the AFPM model predicts that the phase shifts of different frequency components will change with changes in modulation indices. The sensitivity of phase shifts and DMI to changes in modulation index can be investigated by examining the relative sensitivities of both functions. The relative sensitivity of a function to its variable is given in Equation 3.22.

$$Relative\ Sensitivity\ of\ F(x_1, x_2, x_3, \ldots, x_n)\ to\ x_k \equiv S_{x_k}^F = \frac{\partial F}{\partial x_k}\frac{x_k}{F} \tag{3.22}$$

Equations 3.23 and 3.24 represent the relationship between DMI and the summation of phase shifts of the first sidebands[1], Φ, as functions of modulation indices for an AFPM model, where A_{+1}, A_{-1}, A_0, θ_{+1}, θ_{-1}, β and z are represented in Table 2.7.

---

[1] See subsection 4.2.2.1

$$DMI\left(m_a, m_f, m_p\right) = \frac{A_{+1} + A_{-1}}{2A_0}$$

$$DMI = \frac{\sqrt{(m_a A_\Omega)^2 (J_0 - J_2)^2 \cos^2\beta + (m_a A_\Omega (J_0 + J_2)\sin\beta + J_1)^2} + \sqrt{(m_a A_\Omega)^2 (J_0 - J_2)^2 \cos^2\beta + (m_a A_\Omega (J_0 + J_2)\sin\beta - J_1)^2}}{2\sqrt{J_0^2 + 4\,(m_a A_\Omega)^2 J_1^2 \cos^2\beta}} \tag{3.23}$$

$$\Phi\left(m_a, m_f, m_p\right) = \theta_{+1} + \theta_{-1}$$

$$\Phi = -tan^{-1}\left(\frac{b_{+1}}{a_{+1}}\right) - tan^{-1}\left(\frac{b_{-1}}{a_{-1}}\right)$$

$$\Phi = -tan^{-1}\left(\frac{-m_a A_\Omega J_2(z)\,sin(2\beta) - J_1(z)\,cos(\beta)}{m_a A_\Omega J_0(z) - m_a A_\Omega J_2(z)\,cos(2\beta) + J_1(z)\,sin(\beta)}\right) - tan^{-1}\left(\frac{m_a A_\Omega J_2(z)\,sin(2\beta) - J_1(z)\,cos(\beta)}{m_a A_\Omega J_0(z) - m_a A_\Omega J_2(z)\,cos(2\beta) - J_1(z)\,sin(\beta)}\right) \tag{3.24}$$

The RS of both DMI and Φ for each modulation index can be calculated using Equation 3.22. Finally, the second norm of RS for each modulation index is calculated as the RS of DMI and Φ, as given in Equations 3.25 and 3.26.

$$Relative\ Sensitivity\ of\ DMI = \sqrt{\left(\frac{\partial DMI}{\partial m_a}\frac{m_a}{DMI}\right)^2 + \left(\frac{\partial DMI}{\partial m_f}\frac{m_f}{DMI}\right)^2 + \left(\frac{\partial DMI}{\partial m_p}\frac{m_p}{DMI}\right)^2} \tag{3.25}$$

$$Relative\ Sensitivity\ of\ \Phi = \sqrt{\left(\frac{\partial \Phi}{\partial m_a}\frac{m_a}{\Phi}\right)^2 + \left(\frac{\partial \Phi}{\partial m_f}\frac{m_f}{\Phi}\right)^2 + \left(\frac{\partial \Phi}{\partial m_p}\frac{m_p}{\Phi}\right)^2} \tag{3.26}$$

MATLAB was used to numerically evaluate and compare the relative sensitivities of the DMI and Φ with respect to variations in the variables. Note that each of the above RS depends on three variables m_a, m_f and m_p. Therefore, a complete visualization would be four-dimensional. To simplify plotting, the parameter m_a is held fixed, and a three-dimensional surface is rendered over $\left(m_f, m_p\right)$. At each simulation step, a value is assigned to m_a and the RS is computed. This procedure is then repeated for multiple m_a values. The ranges and magnitudes of the variable changes are represented in Table 3.4.

Variable	**Min**	**Step**	**Max**
m_a	1×10^{-6}	1×10^{-5}	1×10^{-3}
m_p	1×10^{-6}	1×10^{-5}	1×10^{-3}
m_f	1×10^{-6}	1×10^{-5}	1×10^{-3}

Table 3.4: The details of the variables used in the relative sensitivity calculation using MATLAB

Figure 3.5 illustrates the 3D plot of the RS for both $DMI\left(m_a, m_f, m_p\right)$ and $\Phi\left(m_a, m_f, m_p\right)$. As it is evident, the RS value of $\Phi\left(m_a, m_f, m_p\right)$ is bigger than $DMI\left(m_a, m_f, m_p\right)$, which means that the $\Phi\left(m_a, m_f, m_p\right)$ is more sensitive than $DMI\left(m_a, m_f, m_p\right)$ when any of the modulation indices change.

The higher sensitivity of $\Phi(m_a, m_f, m_p)$ compared with $DMI(m_a, m_f, m_p)$ implies that variations in the modulation indices induce larger changes in $\Phi(m_a, m_f, m_p)$, which can be exploited for early defect detection. However, it should be emphasized that at the early stage of crack initiation, the variation in phase shift or amplitude of different frequency components is very small and may be masked by noise or measurement errors. Utilizing high-precision instrumentation in conjunction with robust noise-reduction techniques can enhance the reliability of the results.

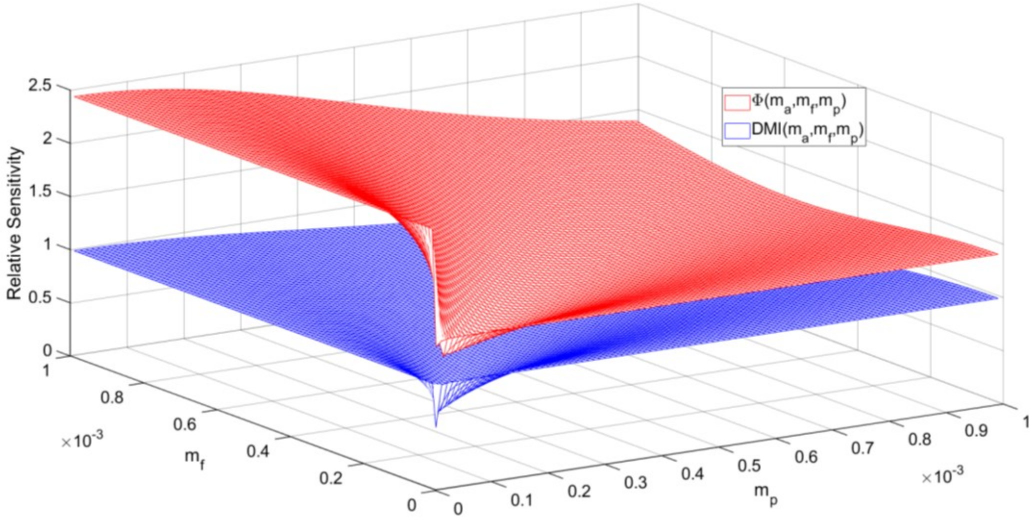

(**a**) $m_a = 1 \times 10^{-6}$

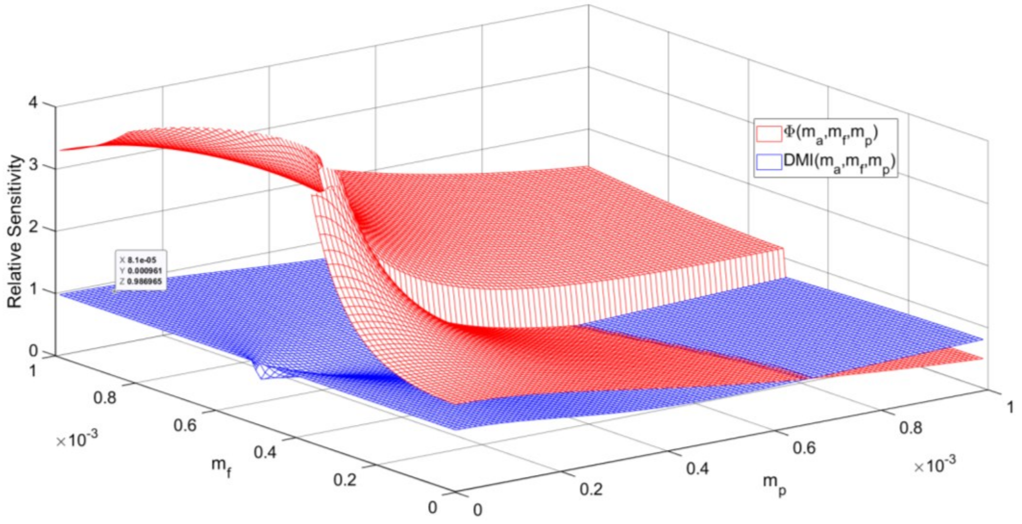

(**b**) $m_a = 5 \times 10^{-4}$

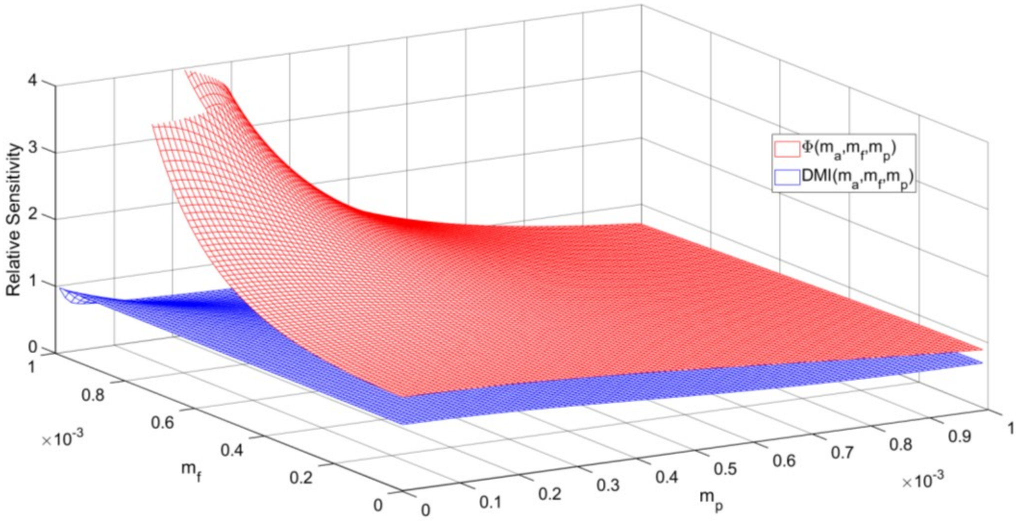

(**c**) $m_a = 1 \times 10^{-3}$

Figure 3.5: The 3D plot of the relative sensitivity (RS) of $DMI(m_a, m_f, m_p)$ and $\Phi(m_a, m_f, m_p)$ evaluated in MATLAB, when (**a**) $m_a = 1 \times 10^{-6}$, (**b**) $m_a = 5 \times 10^{-4}$ and (**c**) $m_a = 1 \times 10^{-3}$

3.1.4.3 MI Separation using the AFPM model

The DMI evaluated by the AFPM model is represented in Equation 3.23, where $J_n \equiv J_n(z)$. As is obvious, this relationship is not as simple as the DMI represented in Equation 3.1 for the AFM model.

As is evident in Table 2.7, the amplitude of different components is the root value of some terms. We know that the power of a sinusoidal waveform with the amplitude A is calculated using Equation 3.27. Thus, using the power of the signal instead of the amplitudes simplifies the root value in the mathematical relationships.

$$f(t) = Acos(\omega t + \theta)$$

$$Power\{f(t)\} = \frac{A^2}{2} \tag{3.27}$$

For the same reason mentioned in subsection 2.4, the first and second sidebands are utilized in the separation technique of this algorithm. The summation and subtraction of the power of the first and second sidebands are given in Equations 3.28 to 3.31.

$$P_{1P} = \frac{(A_{+1})^2 + (A_{-1})^2}{2} = A_\omega \left((m_a A_\Omega)^2 \left({J_0}^2(z) + {J_2}^2(z) - 2J_0(z)J_2(z)\cos(2\beta) \right) + {J_1}^2(z) \right) \tag{3.28}$$

$$P_{1N} = \frac{(A_{+1})^2 - (A_{-1})^2}{2} = A_\omega \left(2m_a A_\Omega J_1(z) \left(J_0(z) + J_2(z) \right) \sin(\beta) \right) \tag{3.29}$$

$$P_{2P} = \frac{(A_{+2})^2 + (A_{-2})^2}{2} = A_\omega \left((m_a A_\Omega)^2 \left({J_1}^2(z) + {J_3}^2(z) - 2J_1(z)J_3(z)\cos(2\beta) \right) + {J_2}^2(z) \right) \tag{3.30}$$

$$P_{2N} = \frac{(A_{+2})^2 - (A_{-2})^2}{2} = A_{\omega}\big(2m_a A_{\Omega} J_2(z)\big(J_1(z) + J_3(z)\big)\sin(\beta)\big) \tag{3.31}$$

The goal of the MI separation is to evaluate the value of m_a, m_f and m_p using the above equations. Like before[1], the output of a separation algorithm is the multiplication of an MI ($m_a$or m_f) by A_{Ω} ($m_a A_{\Omega}$ or $m_f A_{\Omega}$), not a pure MI. Additionally, the amplitude of the HF signal, A_{ω}, is an unknown variable. The ratio of the above equations leads us to new relationships, which are A_{ω} independence. Different ratios of summations and subtractions of sideband power are presented in Equations 3.32 to 3.37. As is evident in the equations, the value of z can be calculated using PR_{12NN} given in Equation 3.35, and $m_a A_{\Omega}$ and $\sin(\beta)$ can be calculated using a combination of other two power ratios.

$$PR_{12PP} \equiv \frac{(A_{+1})^2 + (A_{-1})^2}{(A_{+2})^2 + (A_{-2})^2} = \frac{(m_a A_{\Omega})^2\big({J_0}^2(z) + {J_2}^2(z) - 2J_0(z)J_2(z)\cos(2\beta)\big) + {J_1}^2(z)}{(m_a A_{\Omega})^2\big({J_1}^2(z) + {J_3}^2(z) - 2J_1(z)J_3(z)\cos(2\beta)\big) + {J_2}^2(z)} \tag{3.32}$$

$$PR_{12PN} \equiv \frac{(A_{+1})^2 + (A_{-1})^2}{(A_{+2})^2 - (A_{-2})^2} = \frac{(m_a A_{\Omega})^2\big({J_0}^2(z) + {J_2}^2(z) - 2J_0(z)J_2(z)\cos(2\beta)\big) + {J_1}^2(z)}{2m_a A_{\Omega} J_2(z)\big(J_1(z) + J_3(z)\big)\sin(\beta)} \tag{3.33}$$

$$PR_{12NP} \equiv \frac{(A_{+1})^2 - (A_{-1})^2}{(A_{+2})^2 + (A_{-2})^2} = \frac{2m_a A_{\Omega} J_1(z)\big(J_0(z) + J_2(z)\big)\sin(\beta)}{(m_a A_{\Omega})^2\big({J_1}^2(z) + {J_3}^2(z) - 2J_1(z)J_3(z)\cos(2\beta)\big) + {J_2}^2(z)} \tag{3.34}$$

$$PR_{12NN} \equiv \frac{(A_{+1})^2 - (A_{-1})^2}{(A_{+2})^2 - (A_{-2})^2} = \frac{J_1(z)\big(J_0(z) + J_2(z)\big)}{J_2(z)\big(J_1(z) + J_3(z)\big)} \tag{3.35}$$

$$PR_{11PN} \equiv \frac{(A_{+1})^2 + (A_{-1})^2}{(A_{+1})^2 - (A_{-1})^2} = \frac{(m_a A_{\Omega})^2\big({J_0}^2(z) + {J_2}^2(z) - 2J_0(z)J_2(z)\cos(2\beta)\big) + {J_1}^2(z)}{2m_a A_{\Omega} J_1(z)\big(J_0(z) + J_2(z)\big)\sin(\beta)} \tag{3.36}$$

$$PR_{22PN} \equiv \frac{(A_{+2})^2 + (A_{-2})^2}{(A_{+2})^2 - (A_{-2})^2} = \frac{(m_a A_{\Omega})^2\big({J_1}^2(z) + {J_3}^2(z) - 2J_1(z)J_3(z)\cos(2\beta)\big) + {J_2}^2(z)}{2m_a A_{\Omega} J_2(z)\big(J_1(z) + J_3(z)\big)\sin(\beta)} \tag{3.37}$$

For the next step, a few terms of the Bessel function expansion are considered to approximate the function, while the remaining terms are neglected due to their diminishing

---

[1] see subsection 2.3

magnitude[1]. The approximation of the Bessel functions is listed in Equation 3.17. The separation algorithm, as represented by the final equations, is illustrated in Figure 3.6.

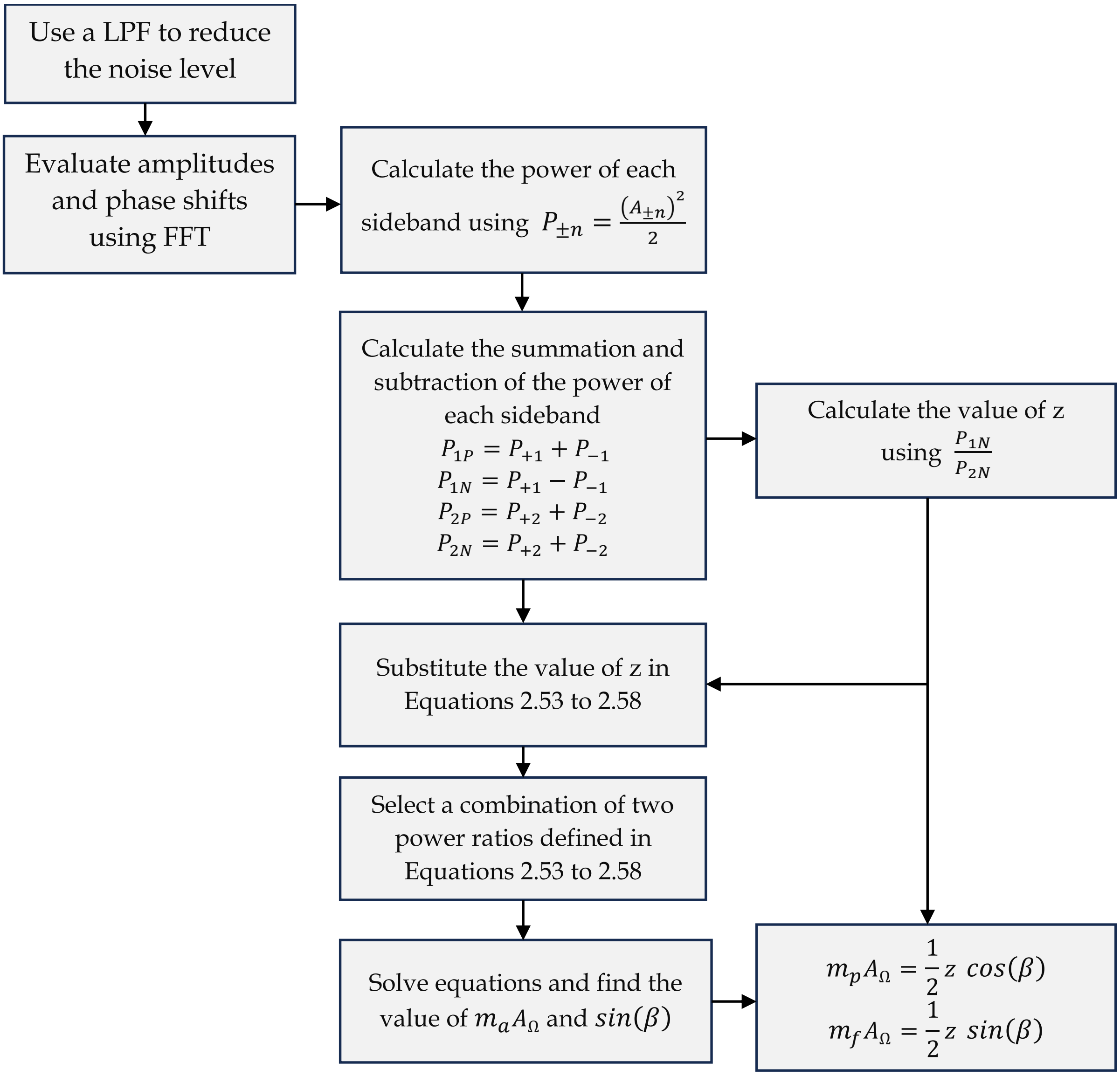

Figure 3.6: The flowchart of the separation algorithm for an AFPM model

The algorithm has been numerically simulated in MATLAB to confirm the MI separation accuracy. An AFPM signal was generated in MATLAB using the parameters listed in Table 3.5. This algorithm has been tested with 100 different parameter combinations, and the results are presented in Figure 3.7.

---

[1] All terms including a $g^{m>5}$ assumed to be zero in $J_n(g)$

Parameter	Value	Parameter	Value
A_ω	$1 < rand < 1.5$ v	A_Ω	1 v
A_{Noise}	$0.05\ v$	A_{NM}	$0 < rand < 0.3$ v
f_ω	200 kHz	f_Ω	500 Hz
ϕ_ω	$0 < rand < 2\pi$	ϕ_Ω	$0 < rand < 2\pi$
m_a	$0 < rand < 0.05$	m_f	$0 < rand < 0.05$
m_p	$0 < rand < 0.05$		

Table 3.5: The value of parameters used in the MATLAB simulation of the MI separation algorithm for an AFPM signal

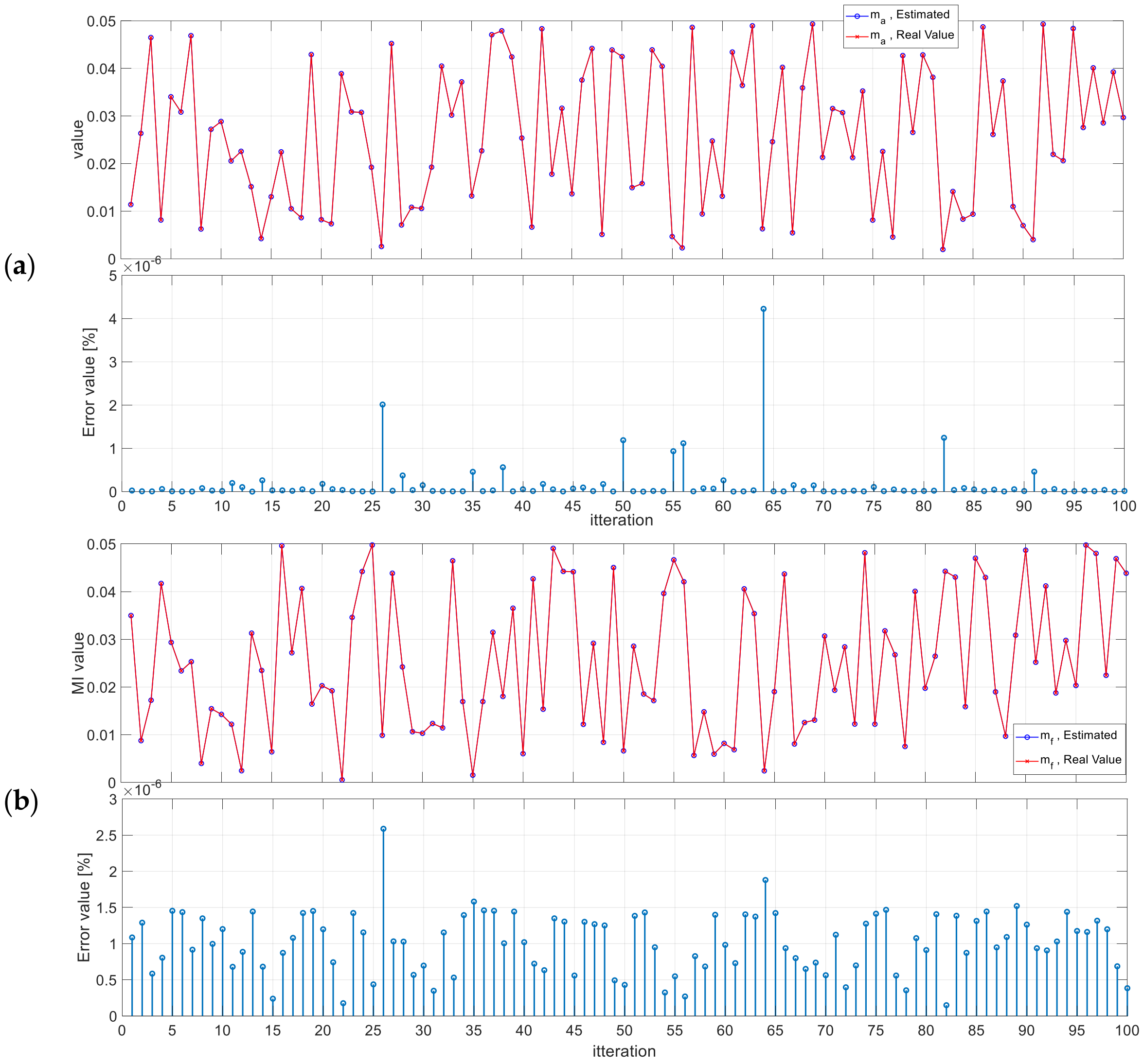

(c)

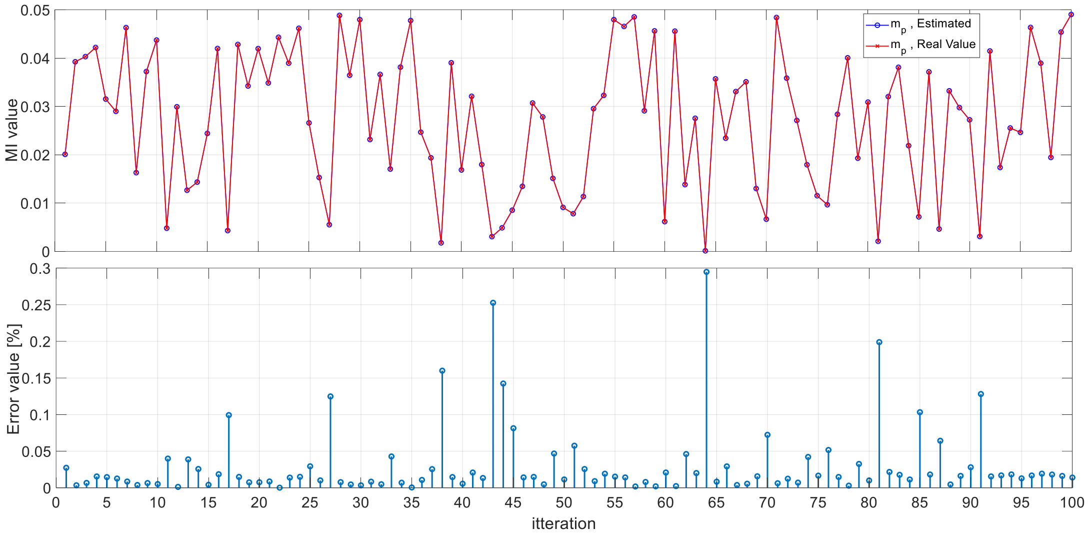

Figure 3.7: Numerical results of the MI separation algorithm using MATLAB for an AFPM signal; (**a**) the actual, estimated value, and the estimation error of m_a; (**b**) the actual, estimated value, and the estimation error of m_f; (**c**) the actual, estimated value, and the estimation error of m_p

3.2 Defect Localization using the VAM Method

The presented localization methodology integrates VAM theory with the Delay-and-Sum (DAS) damage imaging method. The motivation behind combining these approaches is their strengths: VAM detects nonlinearity caused by defects, whereas DAS provides a robust and visually intuitive localization framework.

As mentioned in subsection 2.5, for a defect localization algorithm, a tone burst signal is excited by an actuator or a pair of actuators, and a pair of sensors (at least three) measure the signal at the same time. The location of the damage can be estimated using a damage imaging method. As mentioned in subsection 2.5.1, the DAS method uses the group velocity to estimate the defect location. Additionally, based on the Lamb wave theory, the group velocity is a frequency-dependent parameter (when the material thickness is constant). A limited number of cycles for a sinusoidal waveform exhibits a broad range of side lobes in the frequency domain, as illustrated in Figure 3.8. These side lobes propagate with different group velocities and contaminate the measured signal. Multiplying this signal by a window function, such as the Hanning[1] or Hamming[2] window, which is called windowing, significantly decreases the side lobes in the frequency domain, as shown in Figure 3.8c.

---

[1] $w(t) = 0.5(1 - cos(2\pi t))$

[2] $w(t) = 0.54\ -\ 0.46\,cos(2\pi t)$

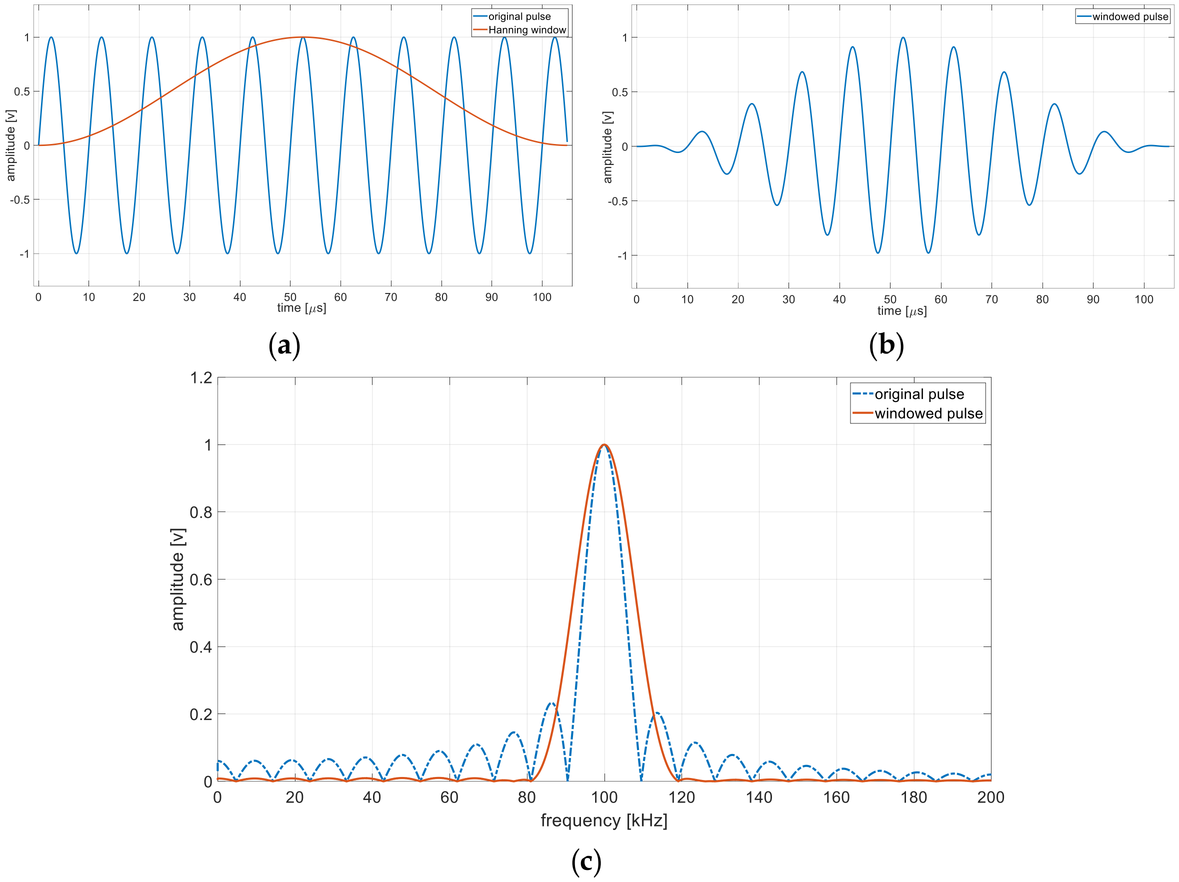

(a) (b)

(c)

Figure 3.8: A pulse with a duration of 10.5 periods at 100 kHz simulated in MATLAB; (**a**) the original pulse and the Hanning window; (**b**) the tone burst signal (windowed pulse) after multiplying the pulse and the window; (**c**) the frequency spectrum of the original pulse (- -) and the final tone burst(-) in the frequency domain

As introduced in subsection 2.2.1, the VAM method requires the excitation of an HF and an LF signal. Additionally, when the primary goal of using the VAM is localizing a defect, at least one of the HF or LF signals must be excited as a tone burst [69, 73]. In this research, the HF signal was chosen to excite as a tone burst based on the following perspectives:

- As discussed earlier, a high amplitude of the LF signal causes a higher MI and a higher sideband amplitude, making the sidebands easier to detect. Therefore, the LF signal is continuously excited in the test sample to achieve a higher vibration amplitude.
- The duration of a tone burst with the same number of signal cycles (periods) is shorter at a higher central frequency. This distinction helps differentiate between the first-arrived wave package and the reflected signal from the edges.

Figure 3.9 illustrates the general steps for defect localization using the VAM method in this research. Each step is explained below.

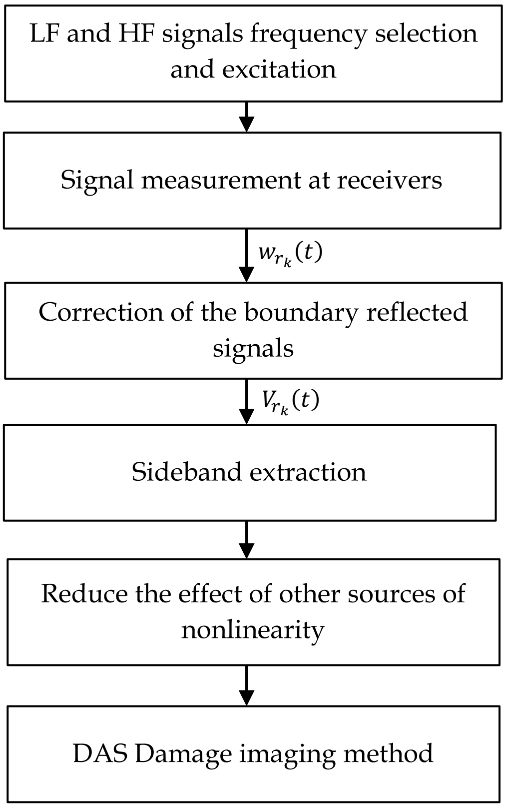

Figure 3.9: The general steps for localization using the VAM method

3.2.1 Frequency selection, excitation, and measurement

The frequency of the LF signal is selected to match the eigenfrequency of the piezoelectric sensor, thereby achieving a high vibration amplitude. Further, the LF signal is excited as an S0-mode Lamb wave to fulfill the necessary conditions mentioned in [37] using two piezoelectrics attached on both sides of a plate [37, 75], as illustrated in Figure 3.10a. The LF signal is excited continuously to ensure reaching a steady-state condition.

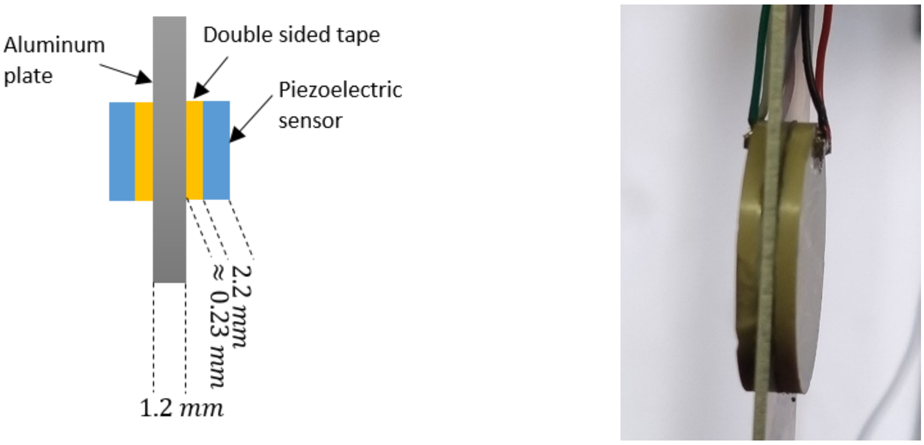

(a)

(b)

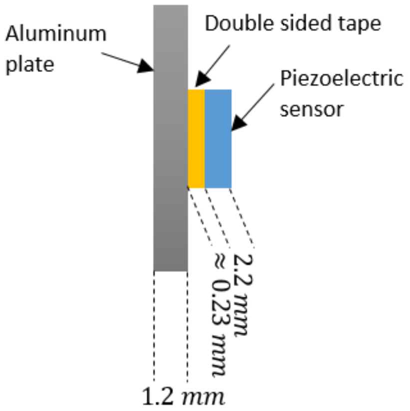

(c)

Figure 3.10: (**a**) Schematic sketch of exciting piezoelectric sensors (HF and LF signals) attached on both sides of a plate; (**b**) a sample of sensors attached on both sides of a narrow plate; (**c**) Receiver attached on one side of the plate

Additionally, an A0-mode tone burst is selected as the HF signal, based on the eigenfrequency ranges of the HF-exciting piezoelectric sensors. The HF signal is excited as a Hanning-windowed tone burst[1] with a duration ranging from 50 µs to 150 µs using two piezoelectric sensors on both sides of the plate. The HF tone burst signal is synchronized to excite when the LF signal reaches the steady-state situation.

As shown in Figure 2.10, a minimum of three receivers is required for defect localization. Thus, four receivers in different positions are attached to one side of the plate, as shown in Figure 3.10c, to measure the signal simultaneously and fulfill the localization requirement. The receivers are synchronized to start measuring the signal after the HF excitation. The process of exciting and measuring signals is repeated several times to attenuate the noise level, and the average of the measured signals is saved. The averaged measured signals at the receivers are called $w_{r_k}(t)$, where r_k refers to the k^{th} receiver.

3.2.2 Correction of the boundary reflected signal

As explained earlier[2], the measured signals, $w_{r_k}(t)$, include the reflected signal from boundaries. It is noticeable that the duration of the HF tone burst signal is chosen to avoid the overlap between the first-arrived signal and the reflections. Since the first-arrived signal is used for localization, the measured signal is multiplied by a boundary coefficient[3], $z_k(t)$, to keep the first-arrived signal untouched, and reduce the effect of the boundary reflected signal, $V_{r_k}(t) = w_{r_k}(t) \times z_k(t)$.

3.2.3 Sideband extraction

The first right-sided sideband (known as the upper sideband) at frequency $\omega + \Omega$ is chosen for the localization [69, 70] considering the following reasons:

- Based on the VAM theory, a modulation appears in the frequency domain when a source of nonlinearity exists on a SUT.
- The first sideband is larger than the other sidebands, theoretically, making it easier to detect.

---

[1] see Figure 3.7b
[2] see subsection 2.5.2
[3] Represented in Equations 2.24 and 2.25

The time history of the sideband at frequency $\omega + \Omega$ is the key to the localization. Since the FFT returns only the frequency information of the signal and cannot distinguish between two signals with different time domain representations, as illustrated in Figure 3.11, a time-frequency transformation is needed to extract the time history information of the sideband at $\omega + \Omega$. Therefore, the Short-Time Fourier Transform (STFT) is used in this research to extract the time history of the sideband.

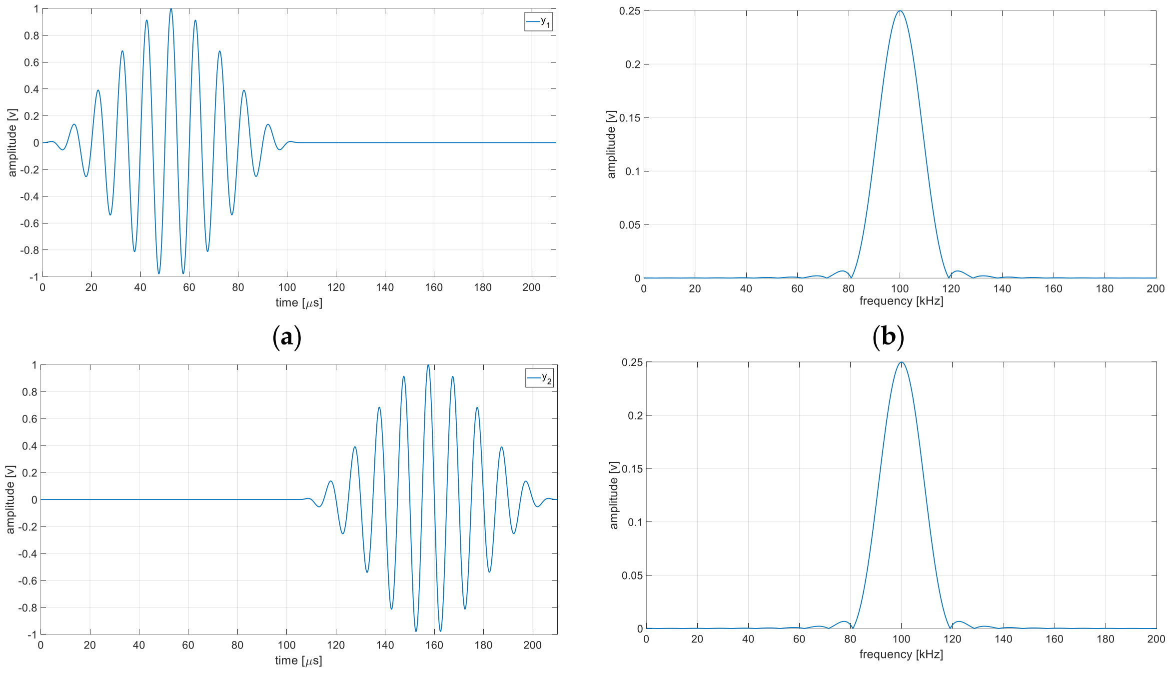

(**a**) (**b**)

(**c**) (**d**)

Figure 3.11: The frequency spectrum of two different signals simulated in MATLAB using the FFT; (**a**) and (**c**) signals with the same frequency but different time domain representation; (**b**) and (**d**) both signals have the same frequency spectrum

3.2.4 Short-Time Fourier Transform

The STFT is a fundamental time-frequency analysis technique used to examine a signal's time and frequency content. The STFT segments the signal into short, overlapping time windows, and then the FFT is applied to each segment. Mathematically, the STFT of a signal $x(t)$ is defined in Equation 3.38, where $w(\mathrm{t})$ represents a sliding window function [112, 113].

$$STFT_{x(t)}(t,\omega) = \int_{-\infty}^{+\infty} x(\tau) w(\tau - t) e^{-j\omega\tau} d\tau \qquad (3.38)$$

STFT is used when a time history of a signal at a specific frequency is needed. The output of the STFT is the signal's amplitude at different frequencies defined by a sampling frequency, f_s and the number of samples in the FFT, N_{FFT}. The Sideband Amplitude (SA) at frequency $\omega + \Omega$ evaluated by STFT for signal $u(t)$ is described by Equation 3.39. The normalized value of the SA for all receivers is used for the damage imaging step. The parameters of the STFT that are used in this study are as follows:

- The sliding window function, $w(\mathrm{t})$, is a hanning window.
- The window length for each segment is selected to be equal to the duration of the HF tone burst signal.

- The overlapping number is selected to increase the time accuracy of the STFT output, which is set to 480ns.
- The number of samples in the FFT, N_{FFT}, determine the frequency resolution, which is set to 500 Hz.

$$SA^{u}_{\omega+\Omega}(t) = STFT_{u(t)}(t\,, \omega + \Omega\ ) \qquad (3.39)$$

3.2.5 Reduce the effect of other sources of nonlinearity

In order to cancel out the instrument-related nonlinearity, only the HF tone burst is excited by a piezoelectric sensor, and all receivers measure the signals simultaneously, resulting in the measured signal $y_{r_{\mathrm{k}}}(t)$. Then, the same coefficient function, $z_k(t)$, is applied to the measured signal, called $U_{r_{\mathrm{k}}}(t) = y_{r_{\mathrm{k}}}(t) \cdot z_k(t)$. Finally, $SA^{U_{r_k}}_{\omega+\Omega}(t)$ is calculated using the STFT with the same parameters. The normalized SA of $U_{rk}(t)$ is subtracted from the normalized SA of $V_{rk}(t)$ is used as an input for the DAS imaging method for localization. This process is illustrated in Figure 3.13 as the HF measurement.

3.2.6 DAS damage imaging method

Finally, the Delay and Sum (DAS) damage imaging method, which is introduced in subsection 2.5.1, uses the result of subtraction $SA^{U_{r_k}}_{\omega+\Omega}(t)$ from $SA^{V_{r_k}}_{\omega+\Omega}(t)$ to localize a defect. In the presence of the continuous LF signal, the HF tone burst that is excited by piezoelectric sensors at coordinates $(x_s\,, y_s)$, propagates radially within the 2D-plate sample with the group velocity $c_{g_{\omega}}$, as illustrated in Figure 3.12a. The HF signal reaches the damage location at coordinates $(x_D\,, y_D)$ after time t_{sD}, as assessed by Equation 3.36a. At the defect location, the sideband at frequency $\omega + \Omega$ evolves due to the local defect. This sideband signal also propagates radially but with the group velocity $c_{g_{\omega+\Omega}}$, as shown in Figure 3.12b.

This signal reaches the receiver located at coordinates $(x_{r1}\,, y_{r1})$ after a time interval t_{Dr1}, assessed in Equation 3.40b. The total time interval t_{sDr1} during which the signal propagates along the path from the actuator to the defect at coordinates $(x_D\,, y_D)$ and to the receiver is provided by Equation 3.40c and shown in Figure 3.12c.

The locus of all potential points with the coordinates $(x\,, y)$ that have the same time interval, t_{sDr1}, are points that lie on an ellipse with the $(x_s\,, y_s)$ and $(x_{r1}\,, y_{r1})$ as its foci, as represented in Equation 3.40d and Figure 3.12d. Finally, the location of a defect will be detected using a minimum of three pairs of sender-receiver, as shown in Figure 2.8.

$$\begin{aligned}
t_{sD} &= \frac{d_{sD}}{c_{g_{\omega}}} = \frac{\sqrt{(x_S - x_D)^2 + (y_S - y_D)^2}}{c_{g_{\omega}}} && \text{(a)}\\
t_{Dr1} &= \frac{d_{Dr1}}{c_{g_{\omega+\Omega}}} = \frac{\sqrt{(x_D - x_{r1})^2 + (y_D - y_{r1})^2}}{c_{g_{\omega+\Omega}}} && \text{(b)}\\
t_{sDr1} &= \frac{d_{sD}}{c_{g_{\omega}}} + \frac{d_{Dr1}}{c_{g_{\omega+\Omega}}} = \frac{\sqrt{(x_S - x_D)^2 + (y_S - y_D)^2}}{c_{g_{\omega}}} + \frac{\sqrt{(x_D - x_{r1})^2 + (y_D - y_{r1})^2}}{c_{g_{\omega+\Omega}}} && \text{(c)}\\
t_{sXr1} = t_{sDr1} &= \frac{d_{sx}}{c_{g_{\omega}}} + \frac{d_{xr1}}{c_{g_{\omega+\Omega}}} = \frac{\sqrt{(x_S - x)^2 + (y_S - y)^2}}{c_{g_{\omega}}} + \frac{\sqrt{(x - x_{r1})^2 + (y - y_{r1})^2}}{c_{g_{\omega+\Omega}}} && \text{(d)} \qquad (3.40)
\end{aligned}$$

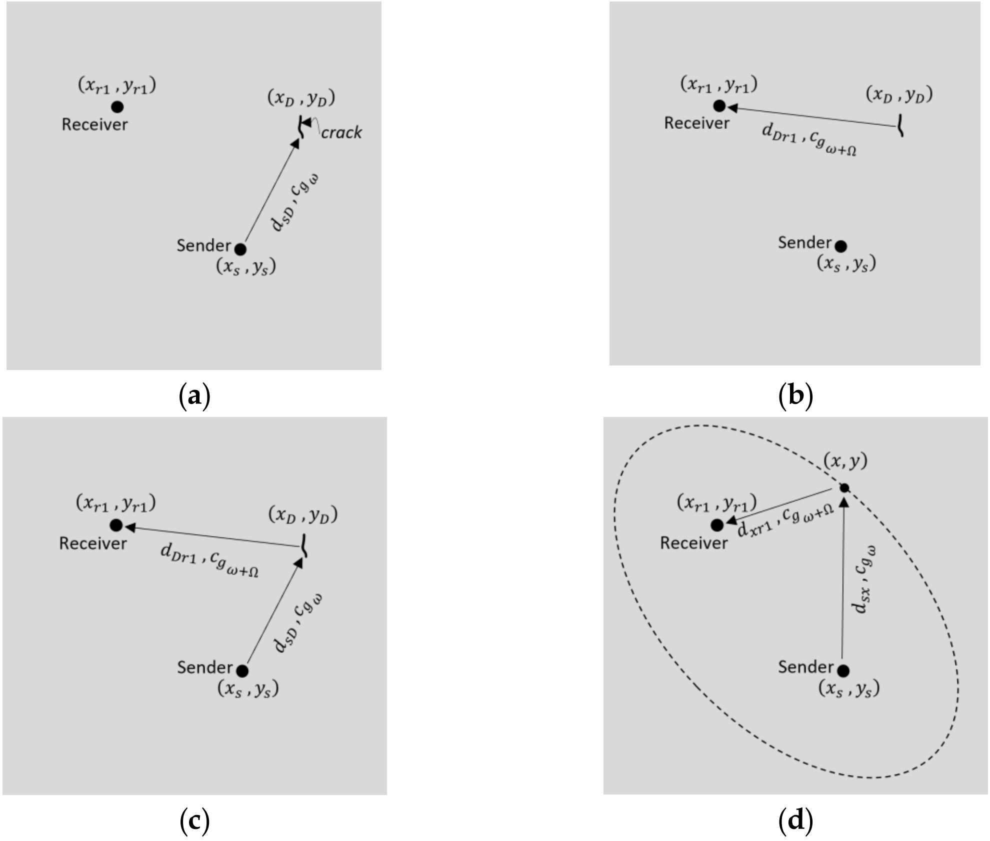

Figure 3.12: Visualization of the time interval between source, defect, and receiver; (**a**) from the source to the defect after t_{sD}; (**b**) from the defect to the receiver after t_{Dr1}; (**c**) from the source to the receiver after t_{sDr1}; (**d**) the locus of all potential points with the coordinates (x, y) that have the same time interval equal to t_{sDr1}

3.2.7 The final flowchart of the localization algorithm

Figure 3.13 represents the final flowchart of the localization algorithm using the VAM method. Since the DAS employs the group velocity for the damage imaging method, the group velocity at frequencies ω and $\omega + \Omega$ is estimated experimentally to minimize calculation errors in defect localization. The localization algorithm has been experimentally tested, and the results are presented in subsection 4.3.6.

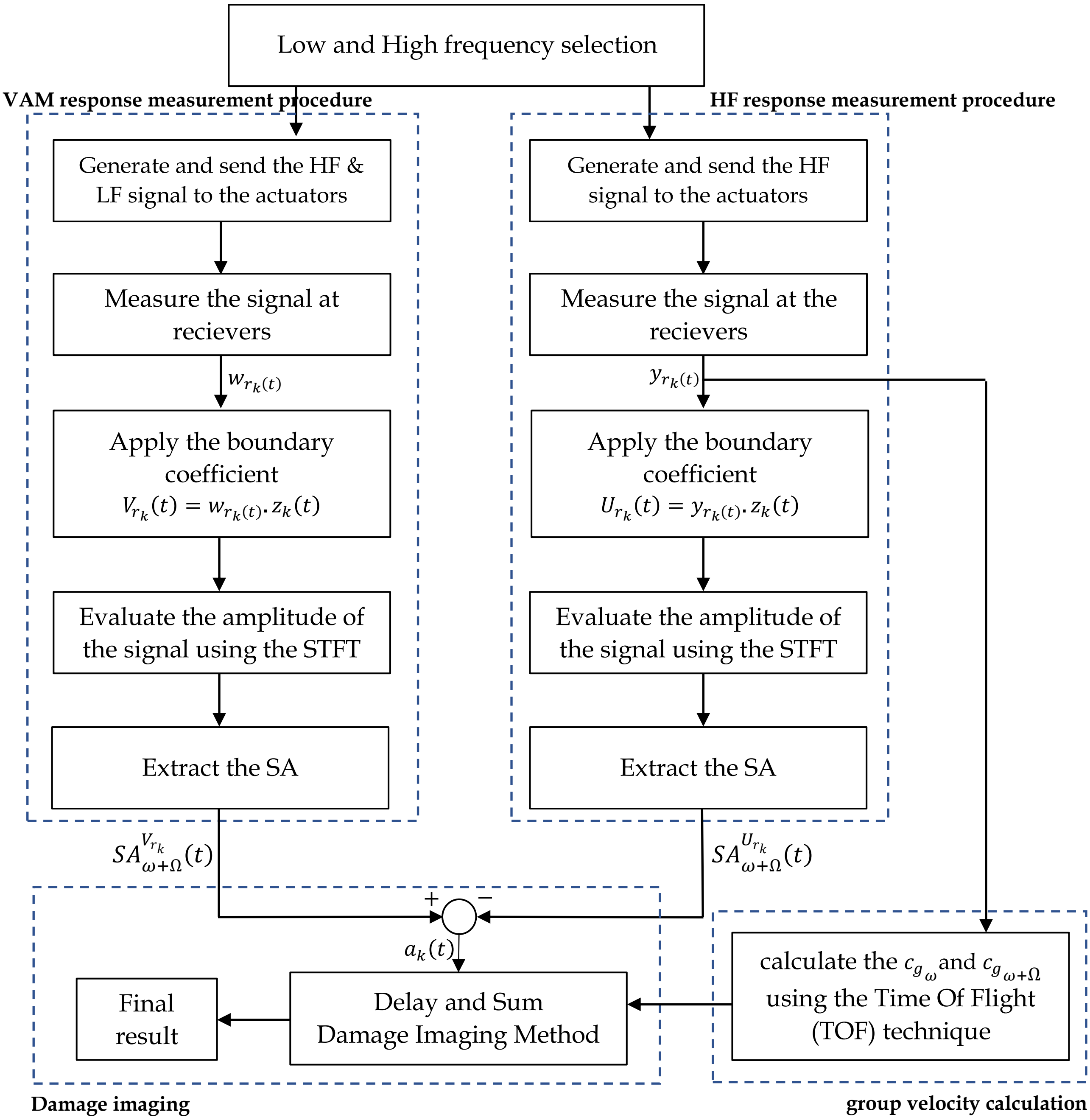

Figure 3.13: The flowchart of the localization using the VAM method

3.3 Chapter Summary

This chapter addresses two core aspects of the Vibro-Acoustic Modulation (VAM) methodology: (1) the separation of modulation indices (MI) and (2) defect localization using the VAM technique.

Initially, the chapter explores methods for accurately separating modulation indices. It introduces mathematical models and algorithms, with a specific focus on amplitude-frequency modulation (AFM) and amplitude-frequency-phase modulation (AFPM) models. It discusses challenges related to non-modulated carriers (NMCs) in measured signals, highlighting that traditional methods, such as the Hilbert Transform (HT), are compromised in their presence. New algorithms, based on advanced mathematical simplifications, are developed to overcome these limitations and provide accurate separation of modulation indices, taking into account both amplitude and phase shifts.

Subsequently, a novel approach for defect localization using the VAM method is presented in the chapter. It emphasizes the combination of traditional Lamb wave-based methods with VAM, involving nonlinear modulation signals generated by defects such as cracks. A specific focus is placed on frequency selection, signal excitation, and the significance of employing short-time Fourier transform (STFT) techniques to effectively extract and analyze sideband frequencies. The methodology also addresses issues such as reflections from boundaries, sensor placement, and the influence of nonlinearities from measurement equipment, proposing corrective techniques and strategies for clear defect identification and accurate localization.

Chapter 4

Experimental Results

This chapter presents the experimental test results for the MI separation algorithm and damage localization method discussed in the previous chapter. The chapter begins with the introduction of experimental test setups for both MI separation and localization algorithms.

Then, the results of MI separation algorithms, along with a comparison to the SPHS method, are presented. Furthermore, the algorithm employed to extract the phase shift of the first sideband and its results are discussed.

In the defect-localization section, the integrity of defect detection is examined when a high-frequency signal is excited as a tone burst with varying durations. Afterward, the presence of the first sideband in the measured response is investigated when the HF signal passes through the defect compared with defect-free paths. Finally, the results obtained from the localization algorithm across various receiver configurations and different HF tone burst durations are presented.

4.1 Test Setup

4.1.1 Test Setup for the MI separation

The suggested MI separation algorithms are experimentally studied using aluminum specimens with a thickness of 3 mm, as shown in Figure 4.1. Two piezoceramics (PI255[1]) with a diameter of 10 mm are attached to one side of the sample to excite the HF signal and measure the system response. The frequencies of the HF signal are selected at the beginning of the test using a linear frequency sweep[2].

The LF signal is applied using a tensile hydraulic machine[3] at a frequency of $f_{\Omega} = 10\ Hz$ and the amplitude of 1.5 kN (0 - 1.5 kN), as shown in Figure 4.2a. After measuring the VAM response for all selected frequencies, the amplitude of the LF is changed to 10 kN (0 - 10 kN) to induce fatigue in the SUT for a certain number of cycles, as shown in Figure 4.2b. The procedure repeats until the sample breaks.

A National Instruments Multifunction I/O device, USB-6366, is used to send the signal into the actuator and measure the system response simultaneously, and a MATLAB script controls the process.

---

[1] see Table 4.1

[2] excite the HF signal without LF, and measure the response using the other piezoelectric (receiver)

[3] INSTRON 250 kN

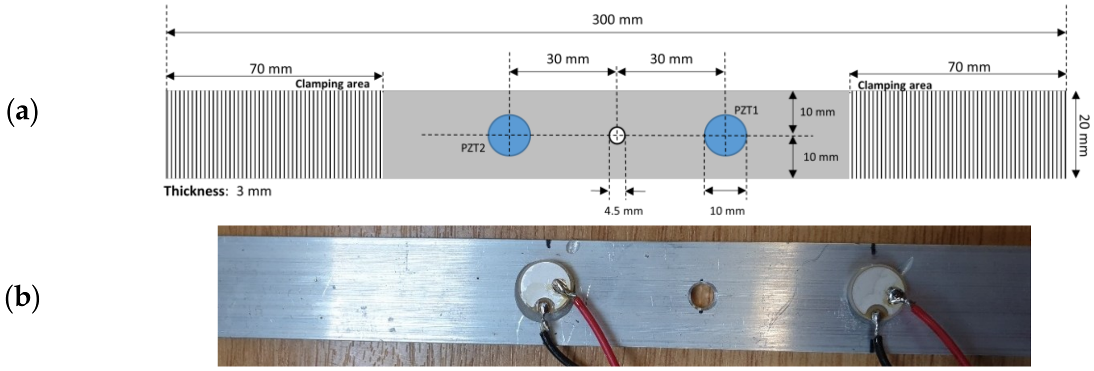

Figure 4.1: A general setup for the MI separation algorithm; (**a**) schematic sketch of the test setup; (**b**) an experimental setup

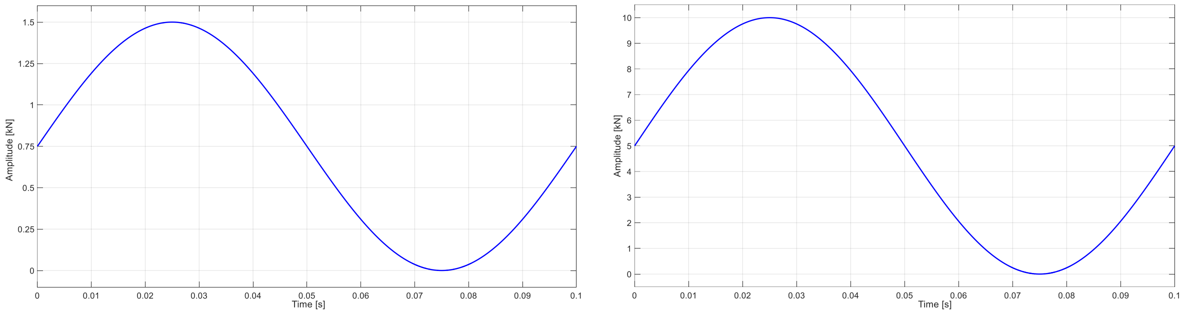

(**a**) (**b**)

Figure 4.2: The LF load amplitude; (**a**) during the VAM measurement; (**b**) Fatigue load

4.1.2 Test Setup for The Defect Localization

To confirm the localization algorithm experimentally, a 700 mm x 1000 mm x 1.2 mm aluminum plate specimen (AlMg3) is used. A hole of 4.5 mm diameter is drilled through the plate at an arbitrary position that is sufficiently away from the edges. The hole has sharp notches on two opposite sides along the y-axis. Their notch angle is 55°, as shown in Figure 4.3. A crack of length a = 30 mm has been produced growing out of the notch by applying cyclic loading along the short length of the metal plate. The aluminum plate is installed in a test rig that holds the plate specimen vertically using four spring connectors at the top and bottom sides, as shown in Figure 4.3a. Figure 4.3b shows close-up views of the notch, crack length, crack tip, and width.

A signal generator (Agilent 33220A) continuously generates the LF signal at the selected frequency. The HF tone burst signal at 175 kHz with a duration of 50 to 150 µs is generated by another signal generator (Keysight 33600A). The HF tone burst signal is excited when the LF signal reaches the steady-state condition. The signals are amplified by two WMA-320[1] high-voltage amplifiers up to 75 volts (peak) and excited by two piezoelectric sensors (PI255). Piezoelectric actuators have diameters of 10 mm and 26 mm for HF and LF signals, respectively, which are attached on both sides of the plate, as shown in Figure 3.10a, to generate S0-mode LF and A0-mode HF signals, respectively. Four piezoelectric sensors PI255, with a diameter of 8 mm, are attached at different positions and used as receivers.

---

[1] https://www.falco-systems.com/High_voltage_amplifier_WMA-320.html

Simultaneously, signals at the receivers are averaged 150 times[1] to reduce the noise level using a 4-channel RBT2004 digital oscilloscope. The NI device (USB-6366) synchronizes all equipment components, and a MATLAB script automates the process.

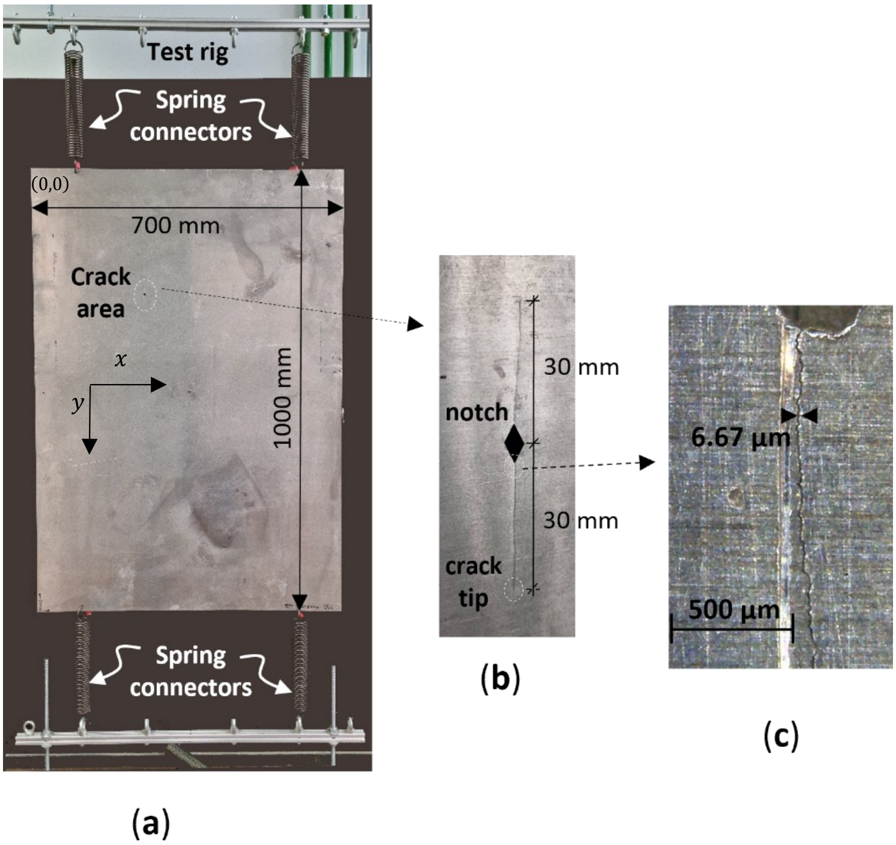

Figure 4.3: (**a**) Plate specimen installed in test rig; (**b, c**) Close-up view of notch and crack (crack length a=30 mm)

4.1.3 Actuators and receivers

Disk-like piezoelectric sensors from the PI Ceramic company are used in this research to both excite and measure vibrations on a test specimen. Each piezoelectric element can be used as either an actuator or a sensor, and its eigenfrequency is based on the disk diameter listed in Table 4.1.

Model number	PRYY+0863	000050294	000030781
diameter	10 mm	8 mm	26 mm
thickness	1 mm	1 mm	1 mm
eigenfrequency range	170 - 220 kHz	200 - 260 kHz	65 - 105 kHz

Table 4.1: List of the disk-like piezoelectric sensors used in the experimental measurement

---

[1] The whole VAM measurement process was repeated 150 times

4.2 Experimental Results of the MI Separation

To apply the MI separation algorithm, a VAM response of a sample must be measured. The continuous VAM response measurement process is illustrated in Figure 4.4, where the linear sweep is explained as follows:

- *HF Linear sweep*
  A single-tone HF signal at a specific frequency is generated in MATLAB and applied to the actuator on the sample using an NI device. The signal at the receiver is measured simultaneously. The amplitude of the measured signal, calculated by the FFT, is saved in a matrix. The process of sending and measuring the HF signal is repeated over a specific range of frequencies. A sample of the linear sweep result is shown in Figures 4.5a and b. A frequency or range of frequencies with high amplitudes, which is usually close to the sample's eigenfrequency, is selected at the receiver for the VAM measurement. The frequency selection can also be achieved using chirp excitation, as illustrated in Figure 4.5c. As shown in Figure 4.5d, an eigenfrequency of the sample can also be detected using single-tone excitation (known as a linear sweep method).

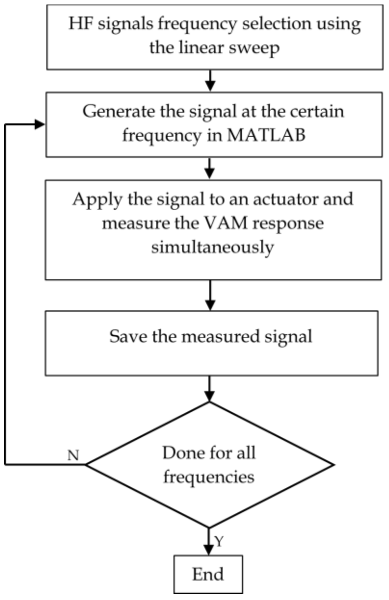

Figure 4.4: The VAM response measurement process

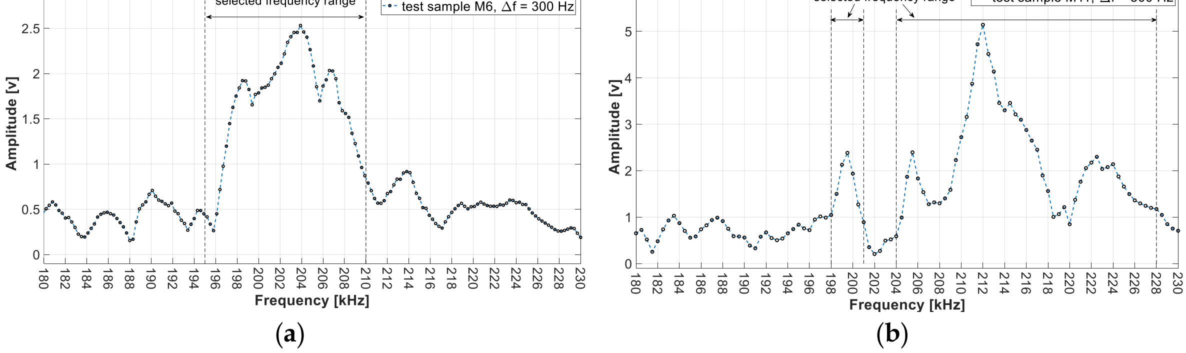

(**a**) (**b**)

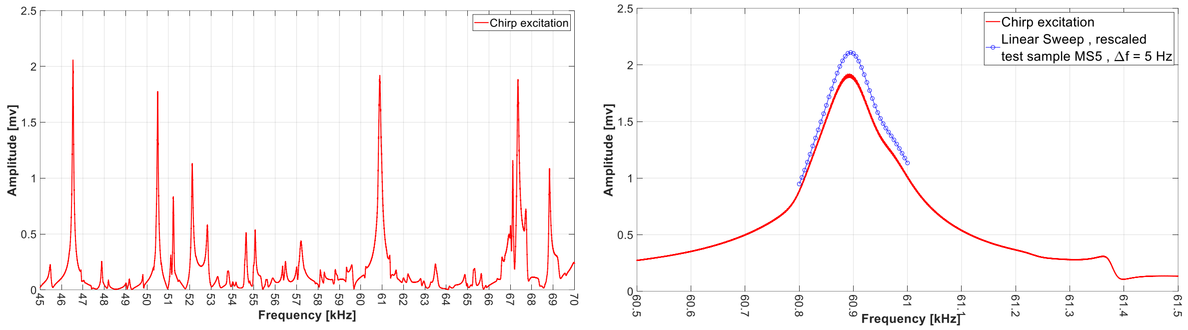

(**c**) (**d**)

Figure 4.5: Frequency selection using the linear sweep; (**a**) linear sweep result for a test sample M6; (**b**) linear sweep result for a test sample M11; (**c**) FFT result of a chirp excitation for test sample MS5; (**d**) comparison between the chirp and single-tone excitation method results around an eigenfrequency at [60.8 - 60.9] kHz for the test sample MS5

4.2.1 MIs separation using the advanced simplification for the AFM model

The MI separation algorithm, using an AFM model introduced in subsection 3.1.3, has been experimentally tested. The MI separation algorithm is applied to the VAM response of several test setups listed in Table 4.2. Figure 4.6 illustrates some results of the MI separation and the SPHS results for the test setup M11 at different high frequencies. The low frequency for all results was 10 Hz, as explained in subsection 4.1.1.

Test series	Number of high frequencies	Test series	Number of high frequencies
E03	10	M12	38
E09	47	M13	41
E13	50	M14	91
M6	31	M15	40
M7	35	M16	39
M8	35	M18	68
M11	56	M19	35

Table 4.2: The number of individual high frequencies for different test setups

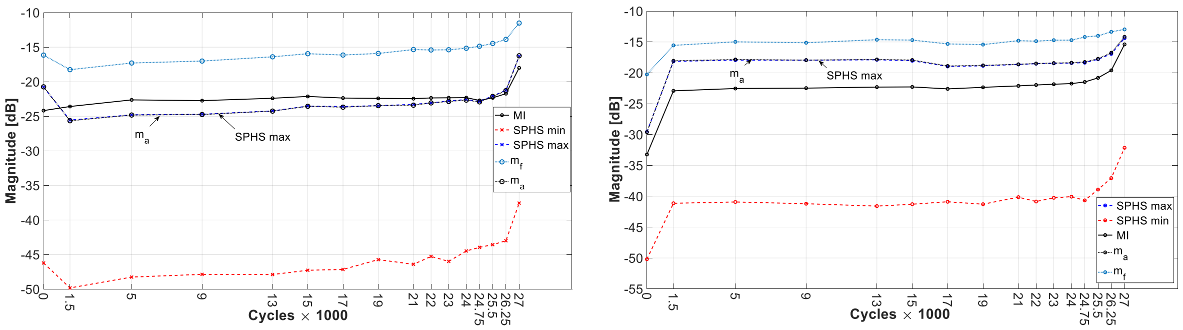

(**a**) (**b**)

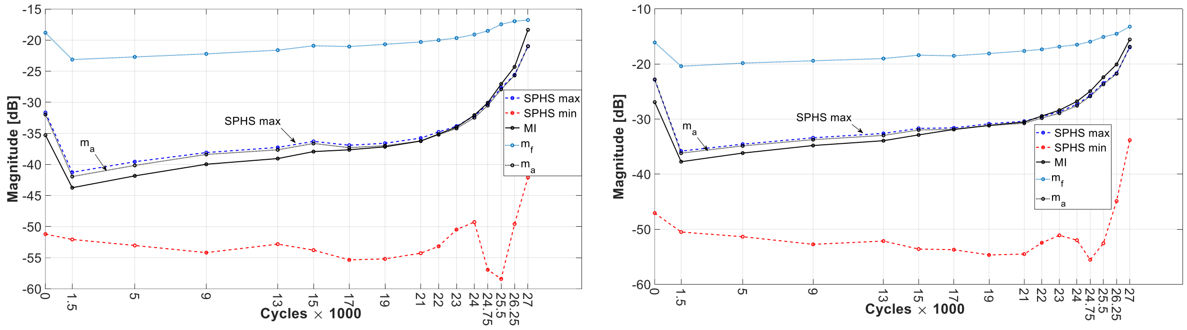

(**c**) (**d**)

Figure 4.6: Results of the MI separation using the AFM model for test setup M11; (**a**) $\omega = 198.5\ kHz$; (**b**) $\omega = 206.5\ kHz$; (**c**) $\omega = 208.5\ kHz$; (**d**) $\omega = 209.0\ kHz$

The following points can be stated based on the obtained results:

- As is evident in Figure 4.6, the maximum values of the SPHS algorithm match the m_a calculated by the MI separation algorithm. However, the minimum values of the SPHS algorithm do not match the calculated m_f.

- The calculated value of m_f was bigger than m_a during the life cycle for 597 out of 616 test results (96.92%). Results reveal that both modulation indices increase simultaneously.

- For the remaining test results, in 8 results out of 616 (1.30%), the value of m_a was bigger than m_f, and in 11 results (1.78%), one of the m_a or m_f was bigger than the other one at the beginning of the life cycle, and then they switched their position at the end. Some of the results are represented in Figure 4.7.

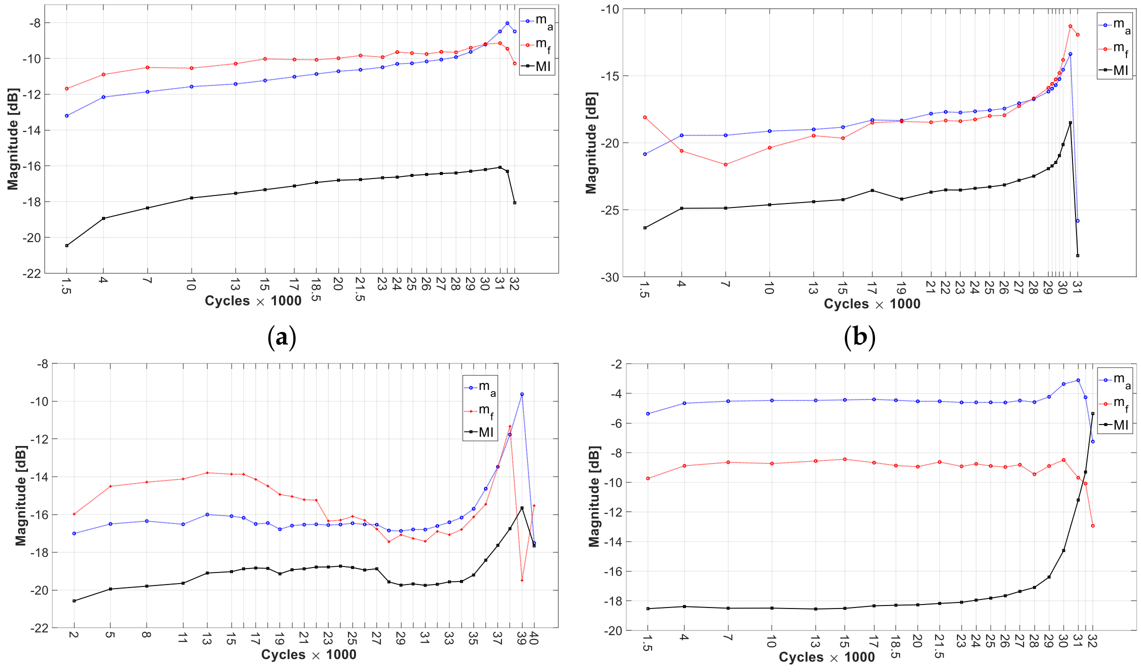

(**a**) (**b**)

(**c**) (**d**)

Figure 4.7: Experimental MI separation results for the AFM model for different test series. (**a**) M16 test series, $\omega = 215.0\ kHz$; (**b**) M14 test series, $\omega = 203.5\ kHz$; (**c**) M18 test series, $\omega = 229.0\ kHz$; (**d**) M16 test series, $\omega = 212.0\ kHz$

4.2.2 MIs separation for the AFPM model

To validate the applicability of the AFPM model experimentally, this section investigates whether the model can capture phase shift variations in the VAM response that are induced by changes in MIs. Unlike the AFM model, the AFPM model predicts that the phase shift of frequency components varies as a function of the modulation indices. Table 4.3 provides a direct comparison of the theoretical phase shifts predicted by both models. The following experimental procedure is designed specifically to isolate and evaluate these shifts, thus confirming the existence of phase-modulated components and the necessity of incorporating phase effects into MI separation.

Frequency	**Phase shifts**	
	The AFM model	**The AFPM model**
ω	ϕ_ω	$\theta_0 = \phi_\omega - tan^{-1}\left(\frac{-2m_aA_\Omega J_1(z)\,cos(\beta)}{J_0(z)}\right)$
		$\theta_0 = \phi_\omega + \theta_{MP_0}$
$\omega + \Omega$	$\phi_\omega + \phi_\Omega$	$\theta_{+1} = \phi_\omega + \phi_\Omega - tan^{-1}\left(\frac{-m_aA_\Omega J_2(z)\,sin(2\beta) - J_1(z)\,cos(\beta)}{m_aA_\Omega J_0(z) - m_aA_\Omega J_2(z)\,cos(2\beta) + J_1(z)\,sin(\beta)}\right)$
		$\theta_{+1} = \phi_\omega + \phi_\Omega + \theta_{MP_{+1}}$
$\omega - \Omega$	$\phi_\omega - \phi_\Omega$	$\theta_{-1} = \phi_\omega - \phi_\Omega - tan^{-1}\left(\frac{m_aA_\Omega J_2(z)\,sin(2\beta) - J_1(z)\,cos(\beta)}{m_aA_\Omega J_0(z) - m_aA_\Omega J_2(z)\,cos(2\beta) - J_1(z)\,sin(\beta)}\right)$
		$\theta_{-1} = \phi_\omega - \phi_\Omega + \theta_{MP_{-1}}$

Table 4.3: The phase shifts for both AFM and AFPM models

4.2.2.1 Angle modulation phase shift

The first step in investigating whether the AFPM model matches a VAM response is to check the change in phase shifts. To investigate the phase shift of the VAM response, a test setup, represented in Figure 4.8, is prepared to measure the VAM response of a sample and the sent HF signal simultaneously. The phase shifts that are written in the figure are introduced in the following:

- θ_ω represents the HF signal phase shift. The value of the θ_ω is arbitrary.
- θ_{pz1-2} represents the signal phase shift change because of a piezoelectric.

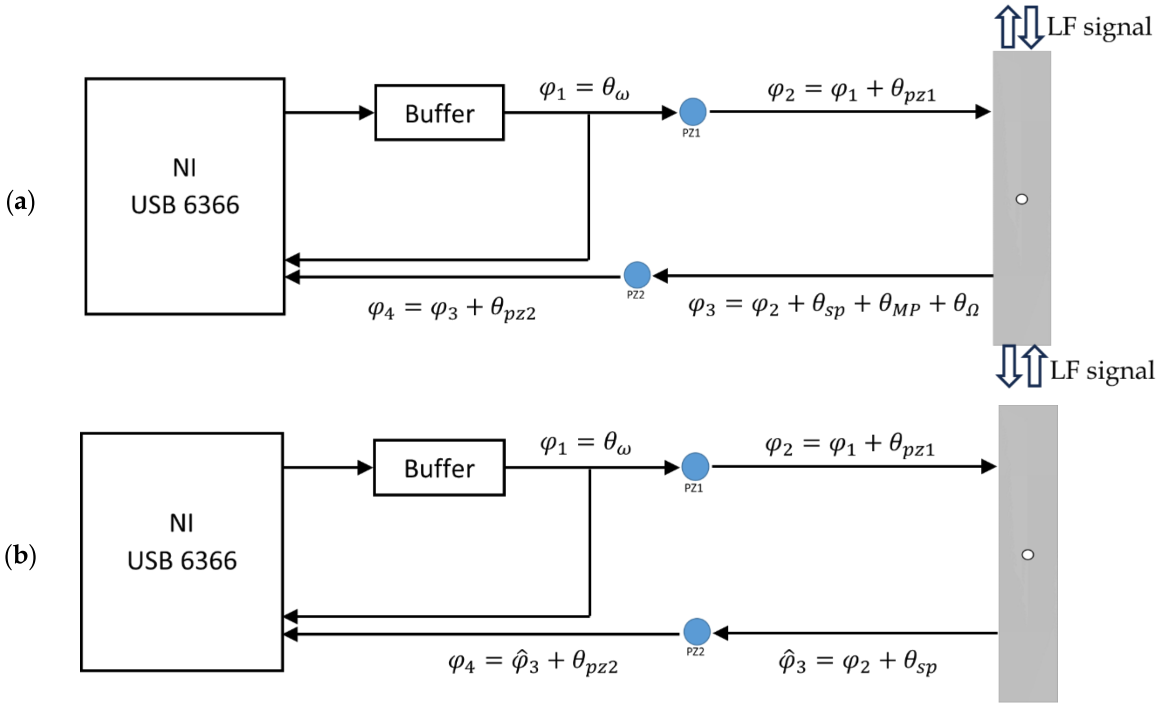

Figure 4.8: The test setup for phase shifts measurement; (**a**) the VAM response setup; (**b**) the HF response setup

- θ_{sp} represents the signal phase shift change because of the sample, such as the propagation delay.
- θ_{MP} represents the signal phase shift change because of the modulation itself (see Table 4.3).
- θ_Ω represents the LF signal phase shift. The value of the θ_Ω is arbitrary.

Due to the NMC, the phase shift of the first sideband was selected for investigation in this test setup. The value of θ_ω, θ_{pz1-2} and θ_{sp} are arbitrary and θ_{MP} is the phase shift that is being calculated. Since the sent signal and response were measured simultaneously, the value of θ_ω can be set to 0 by comparing the sent and measured responses, as represented in Figure 4.9, or can be eliminated by subtracting the sent signal phase shift calculated by FFT from the measured response phase shift at the end of the phase calculation. Thus, the value of θ_ω is assumed to be 0 in the subsequent calculation for the simplification.

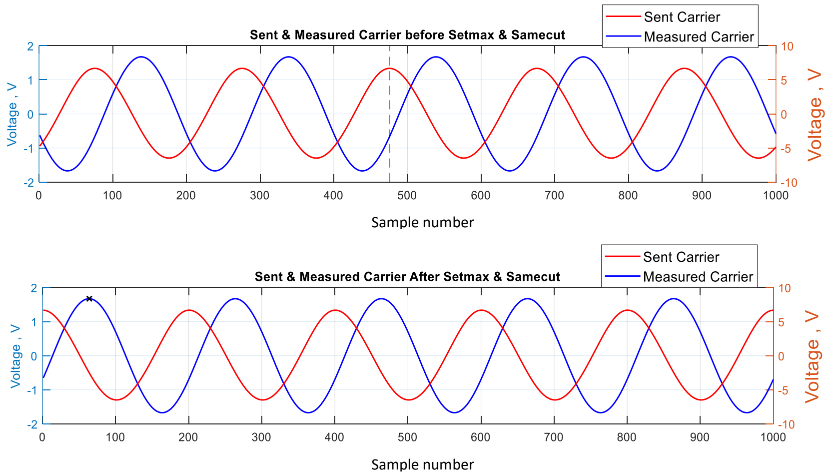

Figure 4.9: The value of θ_ω can be set to 0 by comparing the sent and measured response

The phase shift of the VAM response signal at $\omega \pm \Omega$ using the phase shifts listed in Figure 4.8a is given in Equation 4.1. Using the $\theta_{+1} + \theta_{-1}$ helps us to delete the value θ_{Ω} of the equations, especially considering that the value of θ_{Ω} is unidentified, as represented in Equation 4.2.

$$\theta_{+1} = \theta_{\omega} + \theta_{\Omega} + \theta_{pz1} + \theta_{pz2} + \theta_{sp_{+1}} + \theta_{MP_{+1}} \qquad \text{(a)}$$

$$\theta_{-1} = \theta_{\omega} - \theta_{\Omega} + \theta_{pz1} + \theta_{pz2} + \theta_{sp_{-1}} + \theta_{MP_{-1}} \qquad \text{(b)} \qquad (4.1)$$

$$\theta_{+1} + \theta_{-1} = \left(\theta_{\omega} + \theta_{pz1} + \theta_{pz2} + \theta_{sp_{+1}}\right) + \left(\theta_{\omega} + \theta_{pz1} + \theta_{pz2} + \theta_{sp_{-1}}\right) + \left(\theta_{MP_{+1}} + \theta_{MP_{-1}}\right) \qquad (4.2)$$

The phase shift of the HF response signal at ω using the phase shifts listed in Figure 4.8b is given in Equation 4.3. By comparing the last two equations, it is evident that the terms present in Equation 4.2 are essentially the same as the signal phase shift in Equation 4.3 but correspond to different frequencies.

To compare the phase shift of an HF signal at sideband frequencies, a single-tone sinusoidal waveform at different frequencies was applied to a test sample, and the phase shift was calculated using the measured response at the receiver, as represented in Figure 4.8a. Figure 4.10 shows the measured HF response phase shifts at different frequencies. The frequency of the HF signal was selected equal to $\omega \pm k\Omega$ for $k = 0, 1, 2, \cdots$ to compare the phase shift at different sidebands' frequencies.

$$\varphi_{4_{\omega}} = \theta_{\omega} + \theta_{pz1} + \theta_{pz2} + \theta_{sp} \qquad (4.3)$$

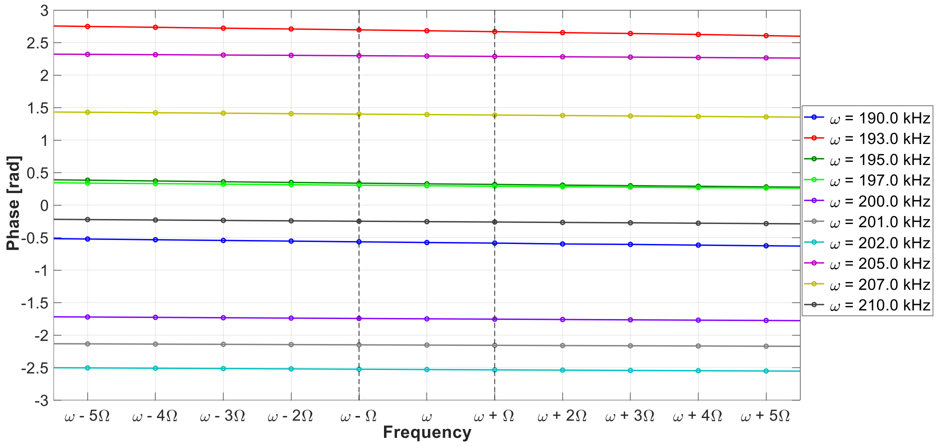

Figure 4.10: The HF response phase shift (φ_4) at different frequencies, $\omega \pm k \times 10\ Hz$ for $k = 0, 1, 2, \cdots$

Results reveal that the phase shifts ($\varphi_{4_{\omega}}$) at $\omega \pm \Omega$ and ω are almost equal with a perfect approximation. Considering this finding, Equation 4.2 can be written as Equation 4.4. Finally, the value of the $\theta_{MP_{+1}} + \theta_{MP_{-1}}$, which is called angle modulation phase shift (θ_{AngM}), can be calculated using Equation 4.5. Figure 4.11 illustrates the results of the θ_{AngM} calculated at different frequencies.

$$\theta_{+1} + \theta_{-1} = \left(\varphi_{4_{\omega}}\right) + \left(\varphi_{4_{\omega}}\right) + \left(\theta_{MP_{+1}} + \theta_{MP_{-1}}\right) \qquad (4.4)$$

$$\theta_{AngM} = \left(\theta_{MP_{+1}} + \theta_{MP_{-1}}\right) = (\theta_{+1} + \theta_{-1}) - 2\varphi_{4_{\omega}} \qquad (4.5)$$

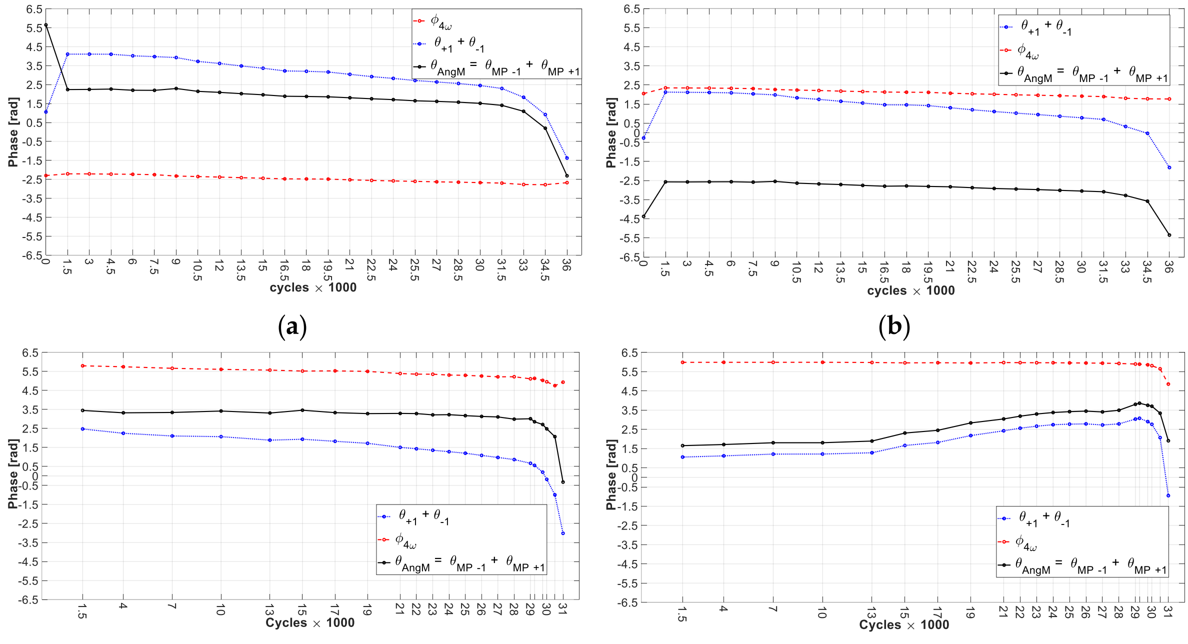

(c) (d)

Figure 4.11: Results of the calculated θ_{AngM} using Equation 4.5; (**a**) M6 test series, $\omega = 201.0\ kHz$; (**b**) M6 test series, $\omega = 206.0\ kHz$; (**c**) M14 test series, $\omega = 175.0\ kHz$; (**d**) M14 test series, $\omega = 197.0\ kHz$

As evident in Figure 4.11, θ_{AngM} changes through the life cycle and reveals that phase shift changes with MIs. As noted earlier, the AFM model fails to explain the phase shift variations corresponding to changes in the MI. In contrast, the AFPM model successfully predicts these variations, which are also evident in experimental observations.

Figures 4.11 and 4.12 demonstrate that the angle-modulation phase shift, θ_{AngM}, evolves consistently as the crack grows, confirming that phase information is fundamentally linked to the MIs, as predicted by the AFPM model. The measured θ_{AngM} provides direct experimental evidence that phase (PM) and frequency (FM) contributions coexist with amplitude modulation in the VAM response.

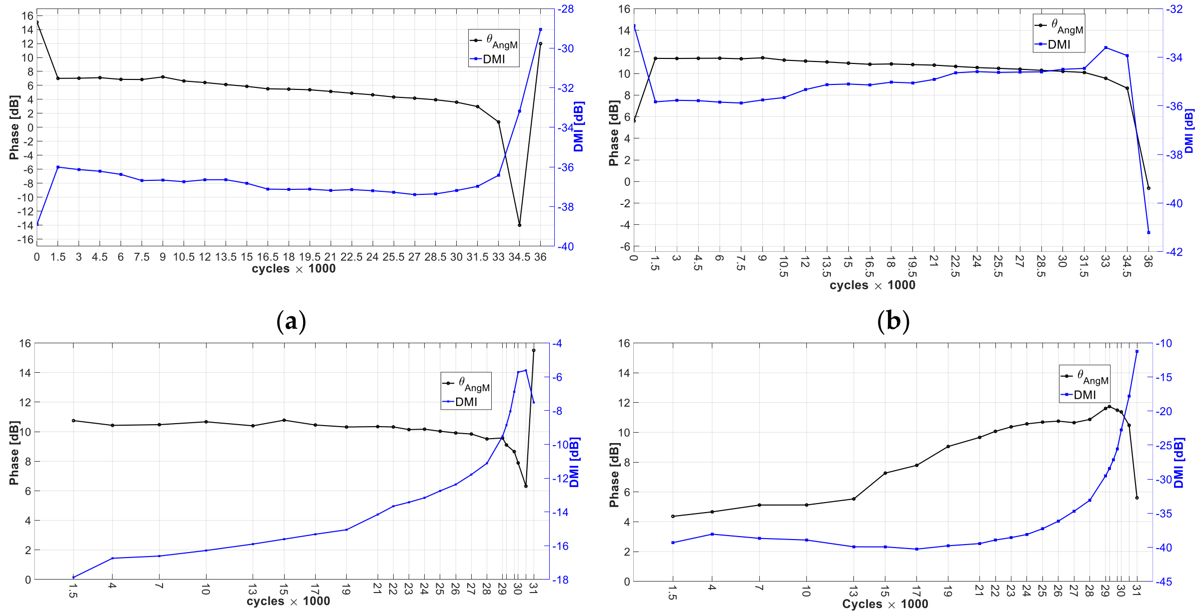

(c) (d)

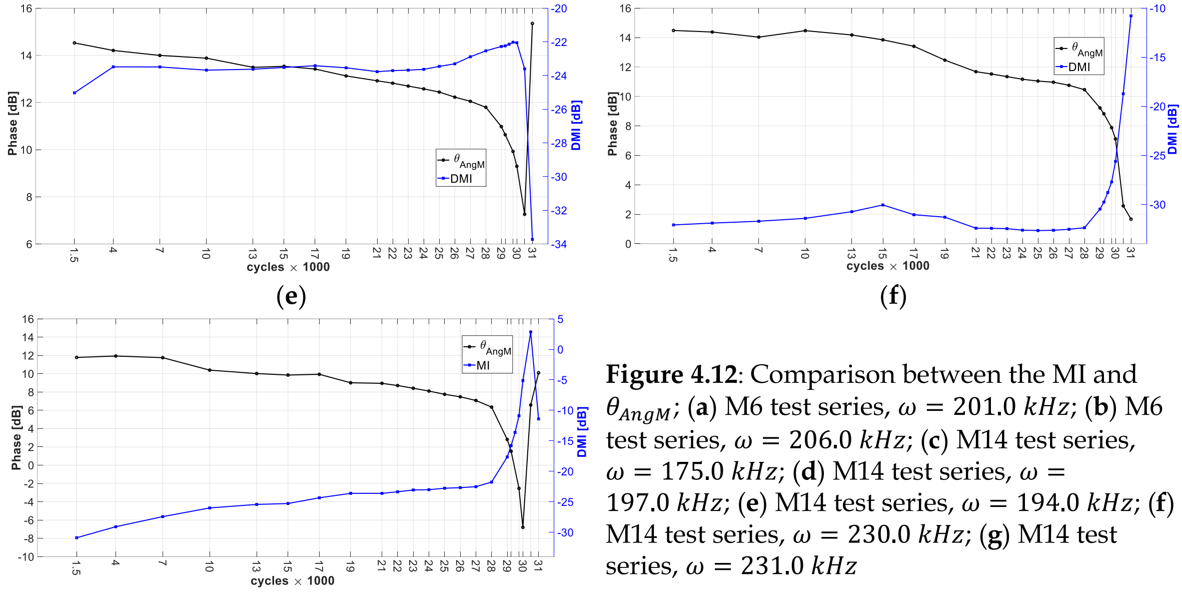

(e) (f)

(g)

Figure 4.12: Comparison between the MI and θ_{AngM}; (**a**) M6 test series, $\omega = 201.0\ kHz$; (**b**) M6 test series, $\omega = 206.0\ kHz$; (**c**) M14 test series, $\omega = 175.0\ kHz$; (**d**) M14 test series, $\omega = 197.0\ kHz$; (**e**) M14 test series, $\omega = 194.0\ kHz$; (**f**) M14 test series, $\omega = 230.0\ kHz$; (**g**) M14 test series, $\omega = 231.0\ kHz$

Since specimens M6 and M14 failed after around 36,500 and 31,200 cycles, respectively, the relative lifetime of each specimen, expressed as a percentage of the total number of cycles at which measurements were performed, is shown in Table 4.4.

M06	**Cycle**	0	1500	3000	4500	6000	7500	9000	10500	12000
	%	0	4%	8%	12%	16%	21%	25%	29%	33%
	Cycle	13500	15000	16500	18000	19500	21000	22500	24000	25500
	%	37%	41%	45%	49%	53%	58%	62%	66%	70%
	Cycle	27000	28500	30000	31500	33000	34500	36000		
	%	74%	78%	82%	86%	90%	95%	99%		
M14	**Cycle**	1500	4000	7000	10000	13000	15000	17000	19000	21000
	%	5%	13%	22%	32%	42%	48%	54%	61%	67%
	Cycle	22000	23000	24000	25000	26000	27000	28000	29000	29250
	%	70%	74%	77%	80%	83%	86%	90%	93%	94%
	Cycle	29750	30000	30500	31000					
	%	95%	96%	98%	99%					

Table 4.4: The details of the measured cycles for the M6 and M14 test setups

A direct comparison between the two curves is not feasible because their ranges of variation are not consistent. To eliminate this dimensional inconsistency and enable meaningful comparison, the data of both curves are normalized using Equation 4.6, where x is either θ_{AngM} or DMI. Under the assumption that data (θ_{AngM}, DMI) at each frequency are independent of those at other frequencies, the minimum and maximum values for each frequency are used to normalize the data at that frequency.

$$x_{Norm} = \frac{x - min(x)}{max(x) - min(x)} \tag{4.6}$$

After data normalization, the rate of change (slope) between successive points was calculated using three different approaches:

1. Direct method: based on the normalized data
2. Mean–mean method: slope between the mean of several consecutive points and the mean of the preceding points.
3. Point–mean method: slope between each point and the mean of its preceding points

The slope variations of θ_{AngM} and DMI curves were compared across different frequencies and across all three calculation approaches for both the M6 and M14 test setups, as illustrated in Tables 4.5 and 4.6.

Lifetime	First method		Second method		Third method	
	N	%	N	%	N	%
60% to 70%	7	22.58 %	16	51.61 %	28	90.32 %
70% to 80%	9	29.03 %	13	41.94 %	28	90.32 %
80% to 90%	6	19.35 %	8	25.81 %	24	77.42 %
60% to 75%	5	16.13 %	15	48.39 %	28	90.32 %
75% to 90%	3	9.68 %	4	12.9 %	24	77.42 %
60% to 80%	5	16.13 %	13	41.94 %	28	90.32 %
80% to 95%	4	12.9 %	1	6.45 %	15	48.39 %

Table 4.5: The number of frequencies[1] in M6 where the slope of variation in θ_{AngM} is bigger than DMI.

Lifetime	First method		Second method		Third method	
	N	%	N	%	N	%
60% to 70%	21	23.08 %	19	20.88 %	40	43.96 %
70% to 80%	22	24.18 %	21	23.08 %	47	51.65 %
80% to 90%	20	21.98 %	25	27.47 %	37	40.66 %
60% to 75%	19	19.78 %	14	15.38 %	40	43.96 %
75% to 90%	16	17.58 %	19	20.88 %	34	37.36 %
60% to 80%	12	13.19 %	11	12.09 %	38	41.76 %
80% to 95%	10	10.99 %	18	19.78 %	26	28.57 %

Table 4.6: The number of frequencies in M14 where the slope of variation in θ_{AngM} is bigger than DMI.

The following conclusions can be drawn based on the results presented in Tables 4.5 and 4.6:

- The above results clearly demonstrate that, at specific frequencies, the θ_{AngM} curve is capable of revealing larger variations than the MDI curve at earlier stages.
- It is worth noting that, as with the DMI curve, which at specific frequencies does not adequately reveal the nonlinearity of the specimen, the phase curve may also fail to reflect variations in response parameters, despite its theoretical higher sensitivity.
- These results should not be interpreted as evidence of the overall superiority of phase over the DMI. As illustrated in Figure 4.12 and summarized in Tables 4.5 and 4.6, the DMI

---

[1] The total nomber of frequancis for each test setup is listed in Table 4.2

curve exhibits greater variations at specific frequencies. Nevertheless, the findings demonstrate that incorporating phase variation analysis can enhance the sensitivity to structural changes, often revealing variations more prominently than the amplitude-based approach.

4.2.2.2 MIs Separation using the AFPM model

Experimental results of the MI separation algorithm using an AFPM model introduced in subsection 3.1.4.2 are represented in this subsection. The MI separation algorithm is also applied to the VAM response of several test setups listed in Table 4.2. Figure 4.13 illustrates some results of the MI separation for the test setup M11 at different high frequencies. It is worth noting that the MI separation equations for this model are highly nonlinear (Equations 3.28-3.33); both MATLAB and Maple were used to solve the equations.

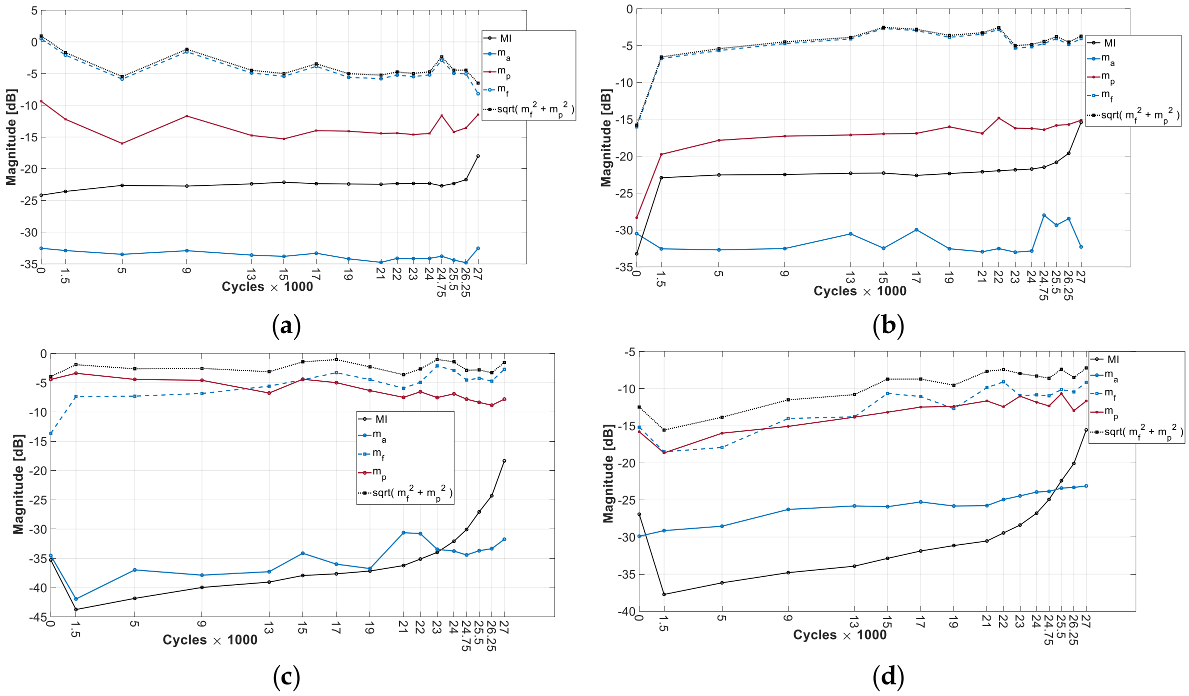

(a) (b)

(c) (d)

Figure 4.13: Results of the MI separation using the AFPM model for test setup M11; (**a**) $\omega = 198.5\ kHz$; (**b**) $\omega = 206.5\ kHz$; (**c**) $\omega = 208.5\ kHz$; (**d**) $\omega = 209.0\ kHz$

The following points can be stated based on the obtained results for the AFPM model:

- Results confirm that, similar to the results for the AFM model, the calculated value of the angle modulation index, $\sqrt{{m_f}^2 + {m_p}^2}$ was bigger than m_a during the life cycle for all 616 out of 616 test results.
- The values of MIs calculated for the AFPM and AFM models differ due to the differences in the equations describing the amplitudes in both models.

4.3 Experimental Results of the Defect Localization

The primary objective of this study was to evaluate the effectiveness of the VAM method in localizing a defect within a structure. As mentioned in subsection 3.2.3, the first sideband at frequency $\omega + \Omega$ was selected for this purpose. Also, in order to simplify the extraction of this frequency from others in the VAM response, the LF excitation was applied via piezoelectric transducers, enabling access to a broader operational bandwidth. The subsequent sections present a step-by-step experimental validation procedure for applying the VAM method in defect localization.

4.3.1 *Integrity of the defect detection*

The reliable defect identification integrity using VAM while the LF signal is transmitted within the kHz range was tested at the first step using the test setup introduced in subsection 4.1.2 and Figure 4.3. In this test, the LF and HF signals were excited continuously to ensure they reached the steady-state condition, and then the response was measured at the receivers. Figure 4.14 shows the measured velocity of a continuous LF signal at 89.5 kHz via a laser Doppler vibrometer (LDV)[1] in the time domain. The figure shows that the LF signal reaches the steady-state condition after 70 ms. Therefore, measurement after 200 ms guarantees that signals have already reached their steady-state condition. The process of measuring the response was repeated three times to measure the HF response, LF response, and VAM response.

The FFT results of the responses at two different frequencies are illustrated in Figures 4.14 and 4.15. It is worth noting that the zero-padding technique was employed to enhance the FFT resolution in Figure 4.16. As evident in Figures 4.15c and 4.16d, only the VAM response contains the sideband signal at $\omega + \Omega$. Results reveal that the defect was detectable when both HF and LF signals were excited by piezoelectric actuators.

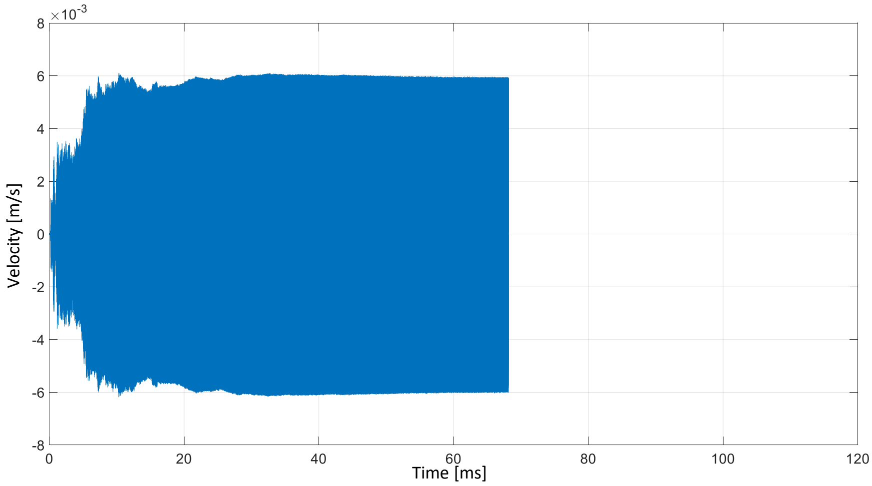

Figure 4.14: The continuous LF signal reaches the steady-state condition after 80 ms

---

[1] Psv-500, Polytec

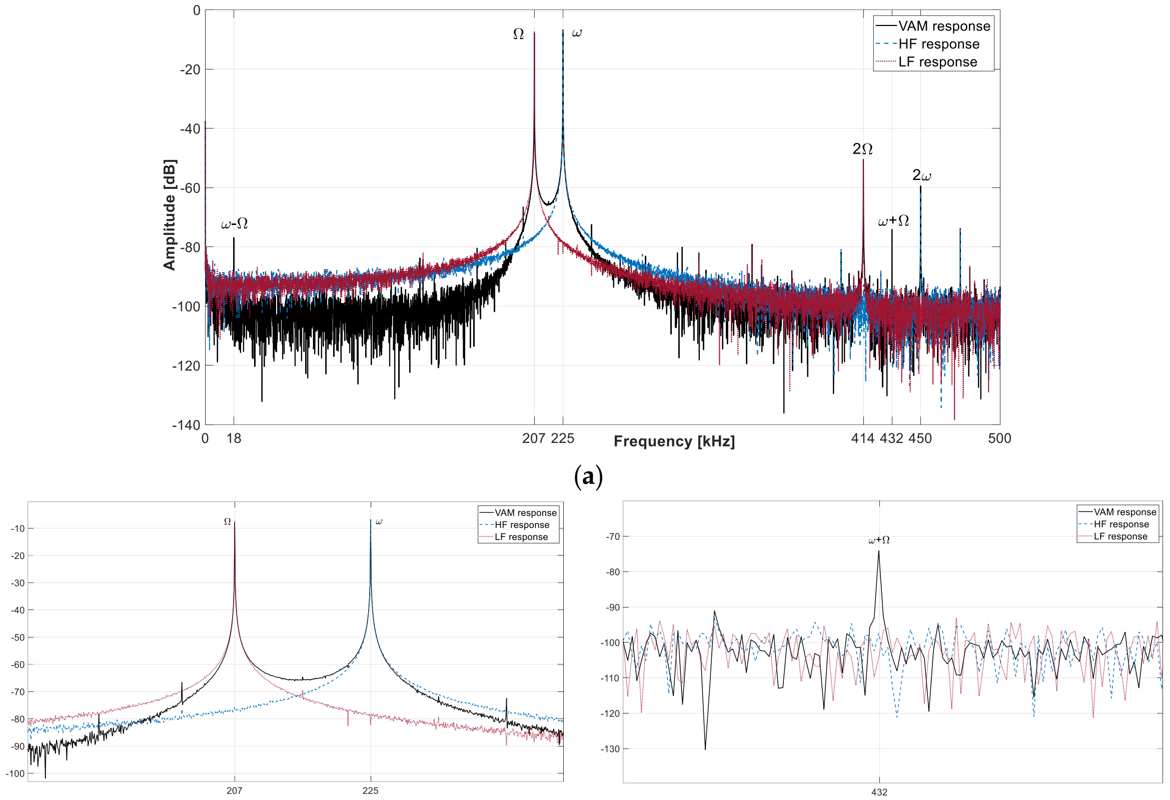

(**a**)

(**b**) (**c**)

Figure 4.15: The FFT results of steady-state responses for $\omega = 225\ kHz$ and $\Omega = 207\ kHz$; (**a**) broad range view; (**b** & **c**) zoomed ranged view; $response\ duration\ =\ 12\ ms\ , F_s = 10.87\ MHz$

4.3.2 HF and LF signals' amplitude and VAM response

In order to examine the influence of the amplitudes of the HF and LF excitations on the sideband amplitude (SA), an experimental test was carried out, as shown in Figure 4.17. The LF and HF signals are generated numerically in MATLAB and sent to the NI device (USB 6366). The two output channels of the NI are amplified by two amplifiers (x50) before being applied to the piezoelectric sensors on the sample. The system response is measured using the RBT2004 digital oscilloscope. The VAM response measurements are repeated for different LF and HF signal amplitudes.

Figure 4.18a represents the amplitude of the VAM response at Ω, ω, and $\omega + \Omega$, when the HF signal amplitude was fixed to 1250 mV, and the LF signal amplitude changed between 10 and 400 mV in MATLAB. Additionally, the results obtained when the LF amplitude was fixed and the HF signal amplitude was changed within the same range are presented in Figure 4.18b. In both figures, the value of the normalized sideband amplitude is calculated using the relationship that is given in Equation 4.7, where A_ω, A_Ω, and $A_{\omega+\Omega}$ represent the HF, LF, and sideband amplitudes, respectively. The normalized sideband amplitudes in both scenarios are illustrated in Figure 4.18c for better comparison.

$$Normalized\ A_{\omega+\Omega} = \frac{A_{\omega+\Omega}}{A_\omega A_\Omega} \tag{4.7}$$

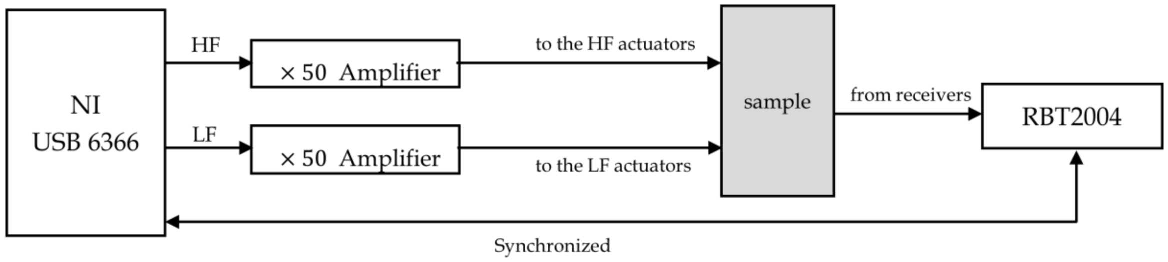

Figure 4.17: Schematic sketch of the VAM response test setup

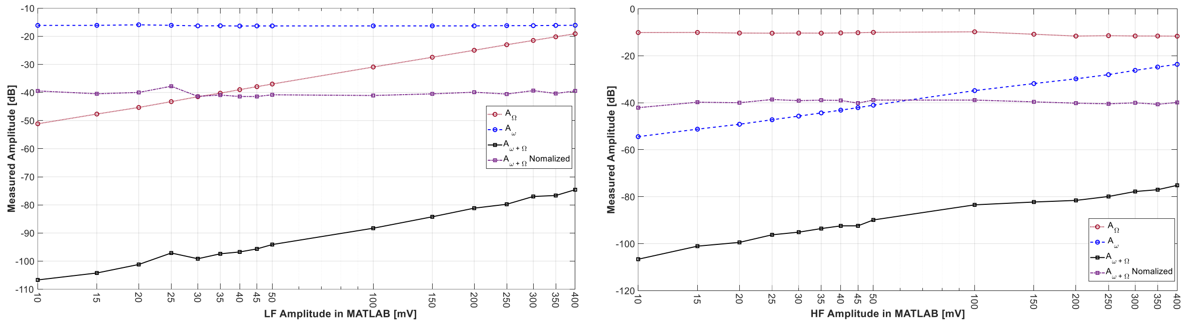

(**a**) (**b**)

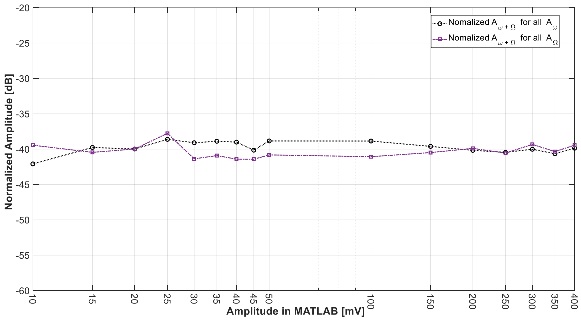

(**c**)

Figure 4.18: The amplitude of the VAM response signal; (**a**) $A_\omega = 1250\ mV$ and $A_\Omega$varies between 10 to 400 mV; (**b**) $A_\Omega = 1250\ mV$ and $A_\omega$varies between 10 to 400 mV; (**c**) comparison between the normalized sideband amplitudes calculated in (**a**) and (**b**)

The following points can be stated based on the obtained results:

- As shown in Figures 4.18a-b, the sideband amplitude varies parallel to the HF or LF amplitude change. These results confirm the mathematical description in the AFM and AFPM model[1] that the sideband amplitude varies proportionally with the product of the LF and HF amplitudes.

- In both figures, the normalized sideband amplitude remains constant, as expected, when one of the LF or HF signal amplitudes changes. Furthermore, Figure 4.18c shows that the normalized amplitudes in both scenarios are nearly equal, confirming that the modulation indices in both scenarios are the same, as expected.

-

---

[1] see subsections 2.3.5 and 2.3.6

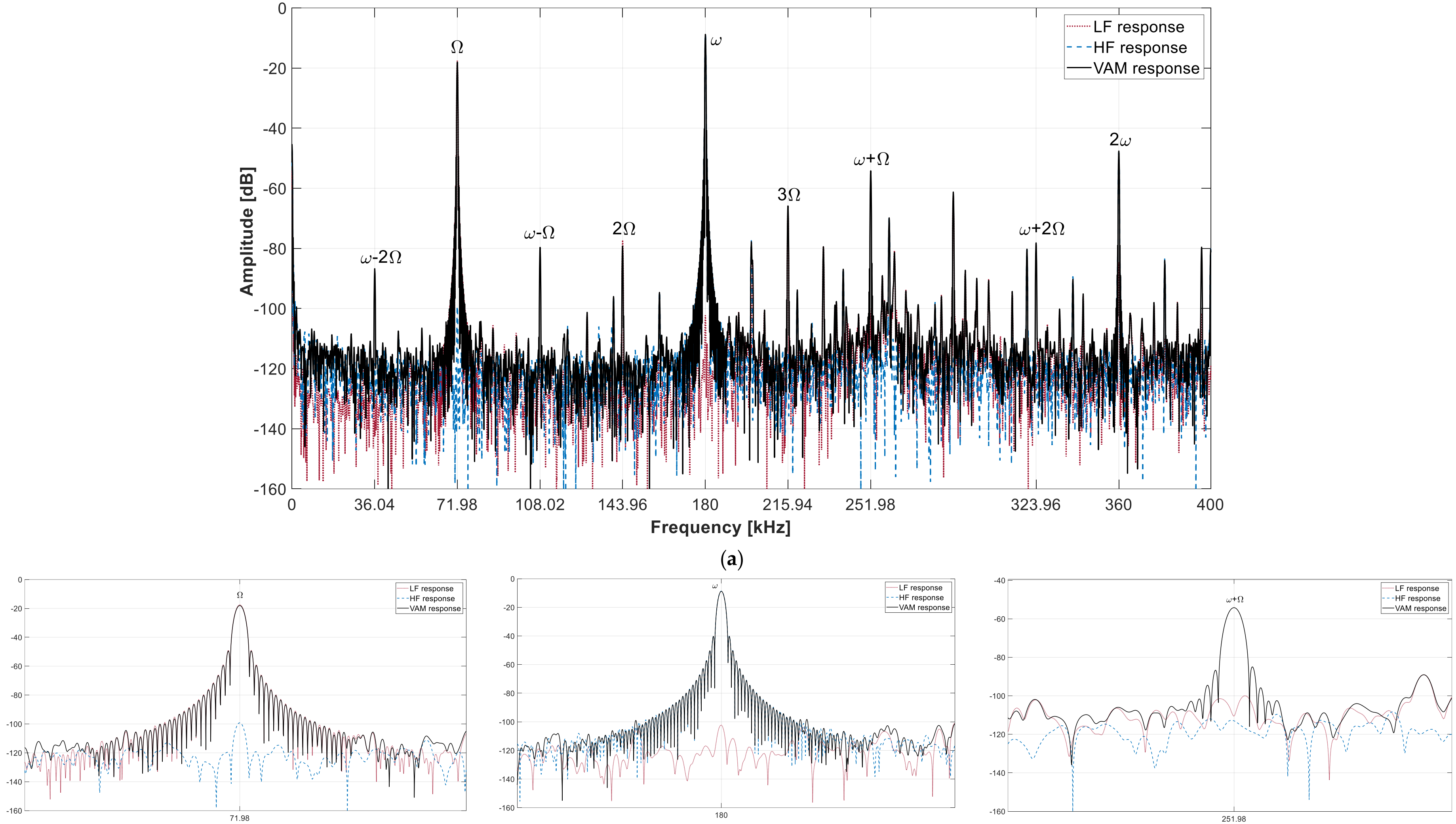

(**a**)

(**b**) (**c**) (**d**)

Figure 4.16: The FFT results of steady-state responses for $\omega = 180\ kHz$ and $\Omega = 71.98\ kHz$; (**a**) broad range view; (**b**) zoomed view at ω; (**c**) zoomed view at Ω; (**d**) zoomed view at $\omega + \Omega$; $response\ duration\ =\ 4.8\ ms\ , F_s = 27.17\ MHz$

4.3.3 Tone burst HF signal and VAM response

As discussed in subsection 3.2, an HF tone burst is required for effective defect localization. In the next step, the influence of the time duration of the HF tone burst on the sideband amplitude is investigated. To this end, a continuous LF signal at 77 kHz was continuously excited in the test setup described in Figure 4.17. After 350 ms[1], another pair of piezoelectric actuators excited a tone burst HF signal at a central frequency of 190 kHz with different durations, and the VAM response was measured simultaneously. Figure 4.19 shows some of the FFT results of the measured responses when the duration of the HF tone burst was changed from 50 to 600μs. The following considerations must be acknowledged when interpreting the above results:

- As evident, the sideband at $\omega + \Omega = 267\ kHz$ is still detectable, while the HF signal was excited as a tone burst signal.

- Theoretically, a tone burst signal with a shorter time domain duration has a broader bandwidth in the frequency domain, as evident in Figure 4.19d. Therefore, a shorter duration requires advanced signal processing and wise frequency selection to avoid masking the sideband frequency with other unwanted frequencies, such as harmonics.

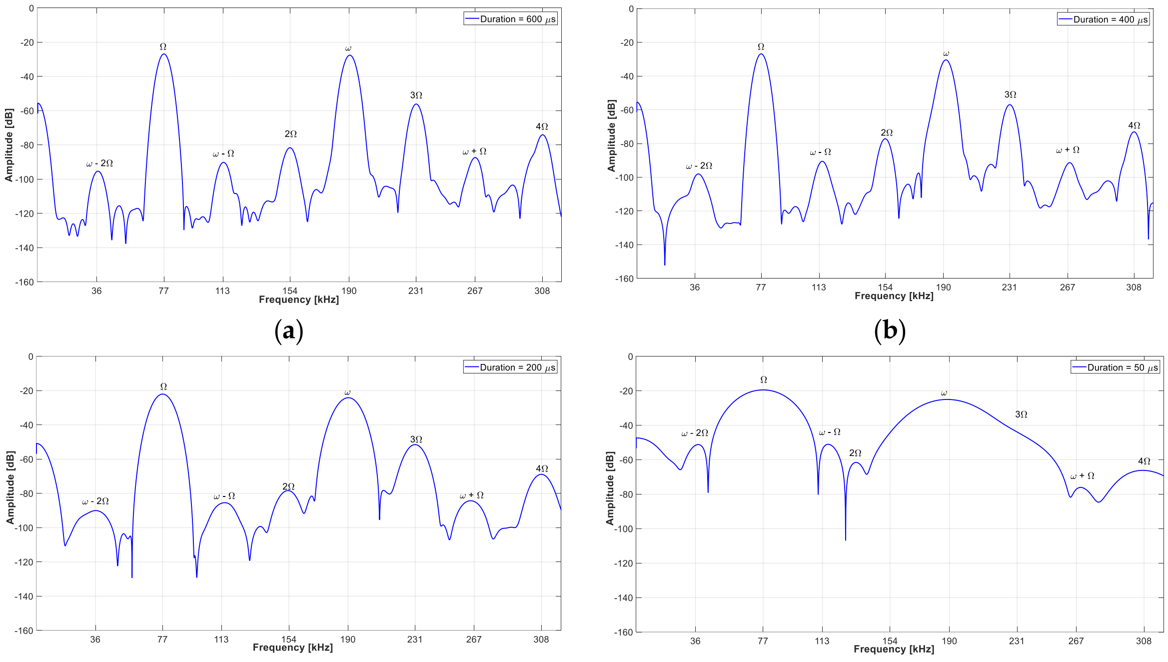

(a) (b)

(c) (d)

Figure 4.19: The FFT results of the VAM response for different time durations of tone burst HF when the LF signal was excited continuously; (**a**) 600μs duration; (**b**) 400μs duration; (**c**) 200μs duration; (**d**) 50μs duration

A different test has been made to investigate changes in the sideband amplitude when the HF excites as a tone burst. A continuous LF signal with a constant amplitude at 77 kHz was applied to the sample. At the same time, a tone burst HF signal with a duration of 300μs at 190 kHz central frequency was applied with another pair of actuators. The amplitude of the

---

[1] refering to Figure 4.14, this delay ensures reaching the steady-state condition for the LF signal

tone burst HF signal was varied from 800 to 1900 mV in the MATLAB script[1], as illustrated in Figure 4.20. Results show that, like in the continuous excitation test[2], the sideband amplitudes vary almost in parallel with the HF amplitudes. In contrast, the normalized sideband amplitudes calculated by Equation 4.6 remain almost constant.

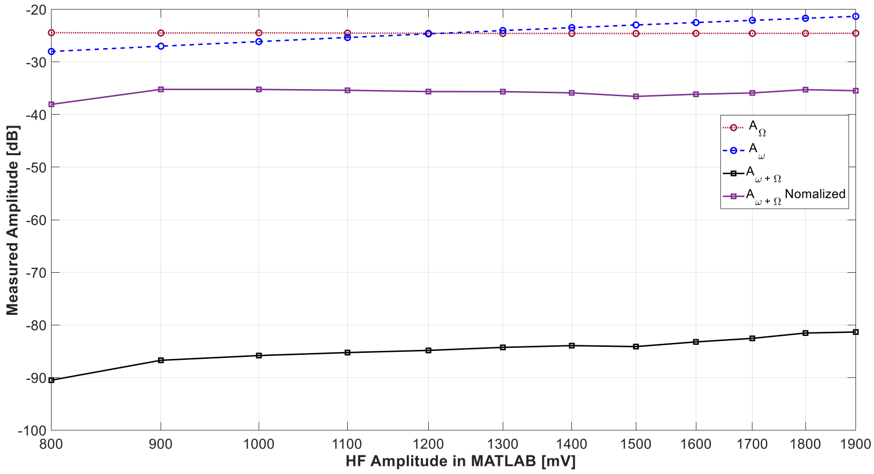

Figure 4.20: The amplitude of the VAM response signal at Ω, ω, and $\omega + \Omega$, when A_{Ω} was kept constant while A_{ω} was varied from 800 to 1900 mV; the normalized sideband amplitude is calculated using Equation 4.6

The VAM method, when the HF signal is excited as a tone burst, is investigated in the previous subsections. In the subsequent subsections, this method is referred to as short-time VAM. The results confirmed that the short-time VAM can detect the defect even when the duration of the tone burst HF is $50\mu s$ in length. However, the location of the defect remains unknown. The following subsections explain how a defect can be localized experimentally using the short-time VAM method.

4.3.4 Group velocity calculation

As discussed in subsection 3.2.6, the group velocity of the lamb wave at frequencies ω and $\omega + \Omega$ are required for the DAS image method. In order to measure the group velocity at these frequencies, a tone burst signal with 50µs length is excited using piezoelectric actuators. Signals are measured using two receivers positioned at 200 mm and 400 mm, respectively, as shown in Figure 4.21a. Figure 4.21b shows an example of the measured signal at the actuator, receiver 1, and receiver 2 when the central frequency was 100 kHz. The group velocity of the signal is calculated using the time-of-flight (TOF) technique [37, 43, 44, 52, 114]. Figure 4.21c represents the experimentally measured frequency-dependent group velocity as well as the expected theoretical group velocity.

---

[1] See Figure 4.17

[2] see subsection 4.3.1 and Figures 4.15 and 4.16

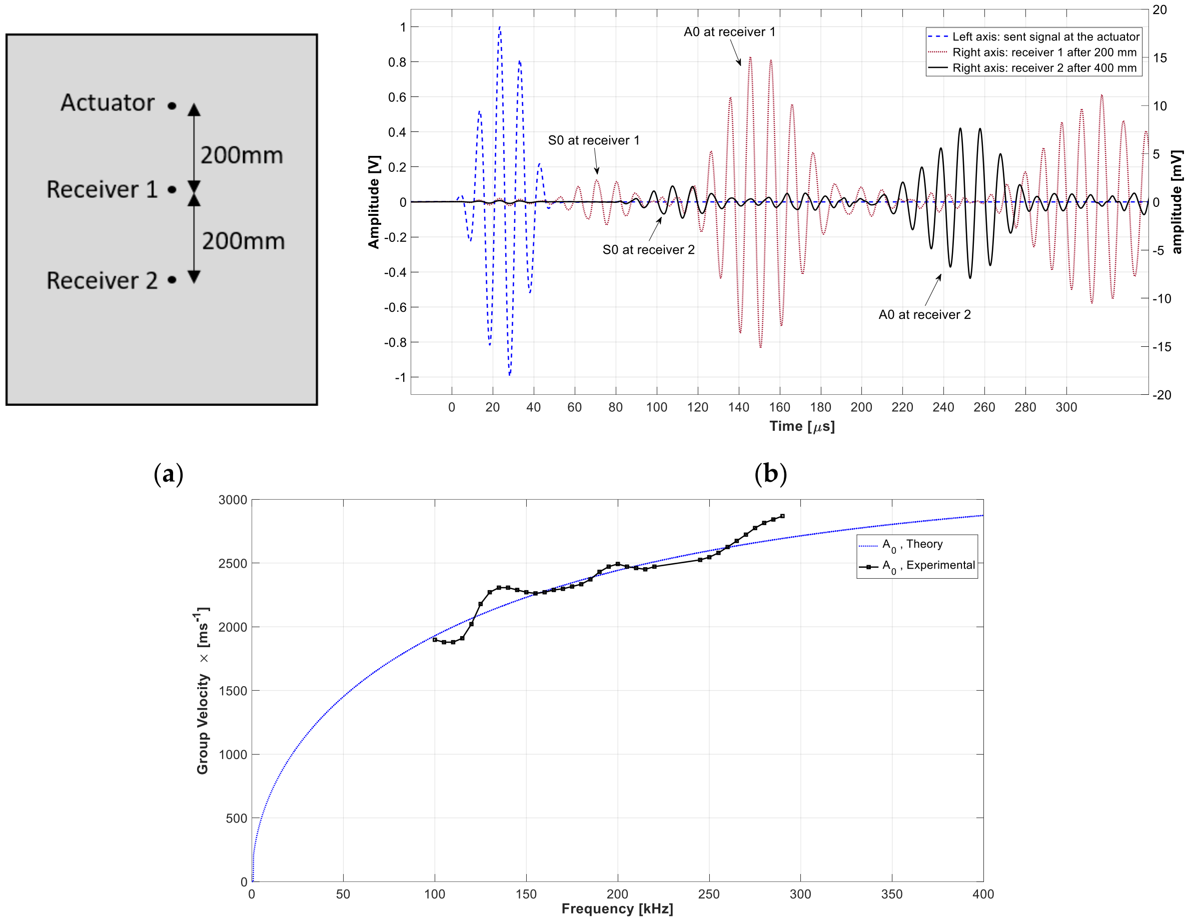

(a) (b)

(c)

Figure 4.21: (**a**) Test setup for evaluating the group velocity; (**b**) The measured signal at the actuator, receiver 1, and 2 when the central frequency was 100 kHz; (**c**) Group velocity for different frequencies, theoretical (continuous line) and experimental results

4.3.5 Role of a notch or a crack in scattering the signal

Based on the wave propagation theories, when a wave propagates and encounters a crack or a notch along its path, it is scattered by the crack. In fact, the crack/notch functions as a secondary source that re-emits the signal [4, 78, 83].

A 700 mm x 1000 mm x 1.2 mm aluminum plate specimen (AlMg3) is used to investigate the signal scattering by a crack. A 200 mm long notch was introduced at the center of the upper edge of the specimen to ensure that the crack would be located in this region and to obstruct the direct propagation of the wave toward the opposite side, as shown in Figure 4.22a. A crack of length 30 mm has been produced growing out of the notch by applying cyclic loading, as illustrated in Figure 4.22b.

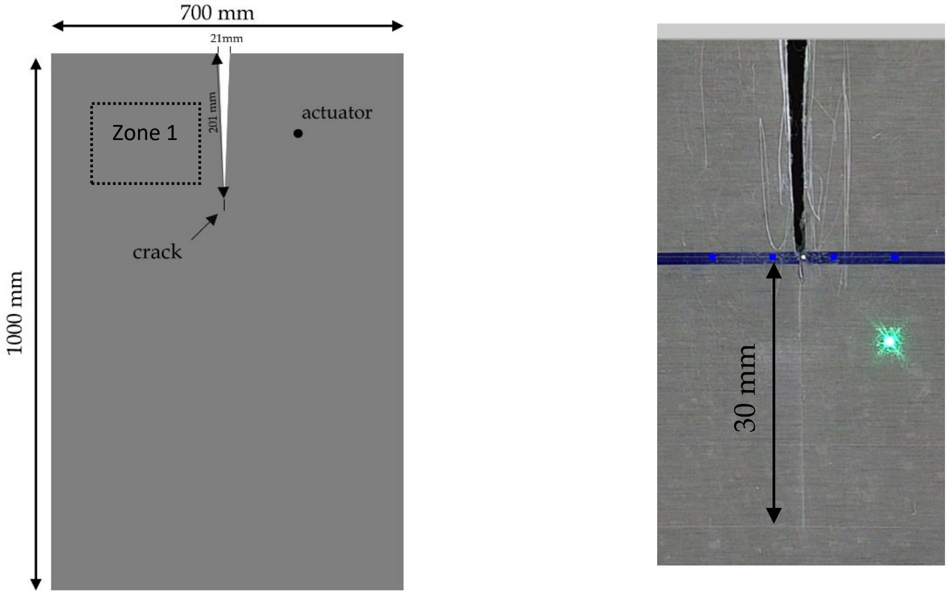

(**a**) (**b**)

Figure 4.22: Investigating the scattered signal from a crack/notch; (**a**) the test setup; (**b**) zoomed view of the crack (the green dot on the sample is the LDV laser point)

A pair of actuators was placed on the right side of the notch, near the edge, in such a way that no direct path for signal propagation toward the left side of the notch existed (zone 1 in Figure 4.22a). A 75 μs length tone burst HF at a central frequency of 175 kHz was applied to the actuators with a delay of 2 ms[1]. Signals at different points were measured using the laser Doppler vibrometer.

Figure 4.23 illustrates selected measuring points and the direct propagation path of the excited tone burst. It should be noted that the actuators are located outside the frame represented in the figure. The measured signals at the selected points in the time domain are plotted in Figure 4.24. The results indicate that, despite the absence of a direct propagation path for the excited tone burst to reach the third point, the signal arrived at P3 before P2 with a lower amplitude. Results confirm that the notch tip scatters a part of the tone burst, and the signal measured at P3 has already passed through the crack. The 2D visualization of the tone burst propagation using the measured voltages for the selected area around the crack at four different time durations after the excitation is represented in Figure 4.25.

---

[1]. To scan all measuring points using the LDV, the situation for all points must be the same. A 2ms delay at the beginning guarantees that the vibration from the previous excitation completely vanishes after multiple reflections.

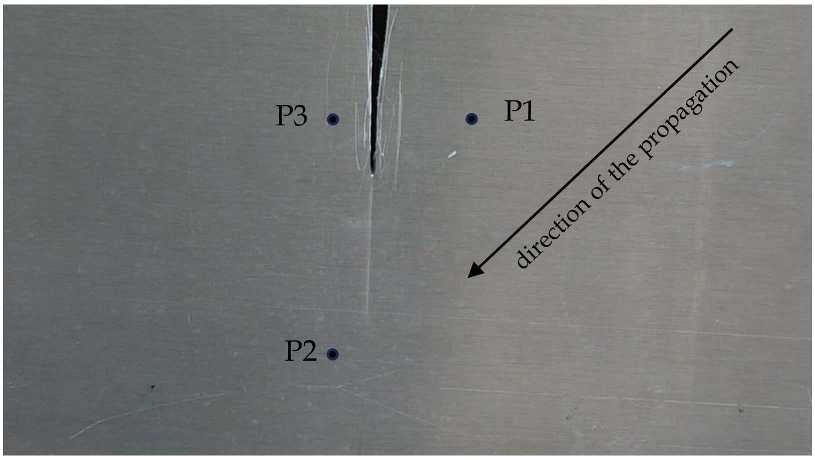

Figure 4.23: Location of selected measuring points and the direction of the tone burst propagation

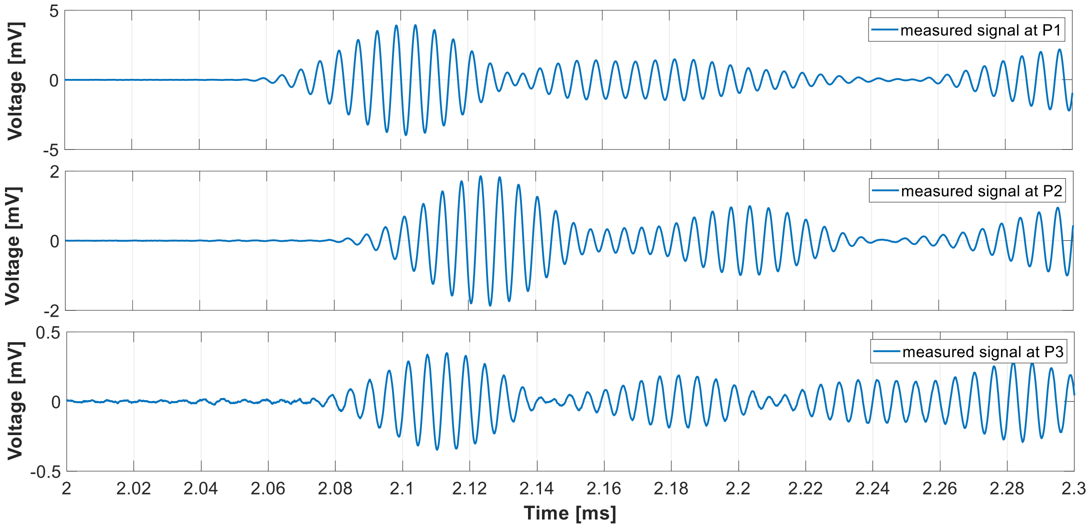

Figure 4.24: The measured voltage at the selected points using the LDV

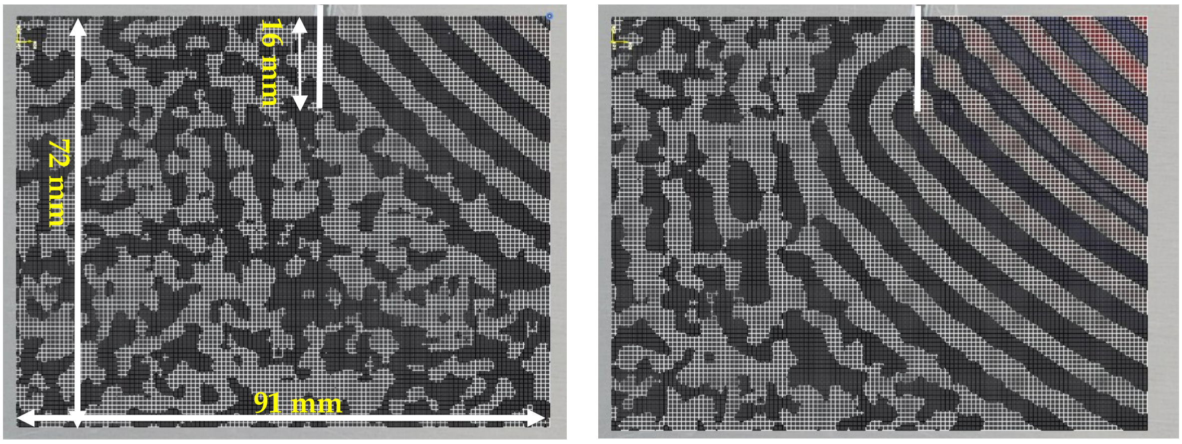

(**a**) 53.20 μs after the excitation

(**b**) 67.84 μs after the excitation

(**c**) 77.12 μs after the excitation (**d**) 96.48 μs after the excitation

Figure 4.25: The 2D visualization of the scattered signal by the notch/crack at: (**a**) 53.20 μs, (**b**) 67.84 μs, (**c**) 77.12 μs, and (**d**) 96.48 μs after the excitation

Another test setup has been prepared and tested to continue investigating the scattered signal from the notch and tip of a crack using the arrival time. A 20 mm notch was made on the upper side of a plate-like aluminum sheet, and a crack of 145 mm length was generated extending from the notch by applying cyclic loading, as shown in Figure 4.26a. As can be observed in Figure 2.25b, the crack edges are not perfectly aligned, and a slight gap exists between them, particularly near the notch. A pair of actuators is positioned on the right side of the crack to excite a tone burst HF signal, and four piezoelectric sensors are positioned at different locations to measure the signal simultaneously, as shown in Figure 4.26b, where N and T represent the tip locations of the notch and the crack, respectively.

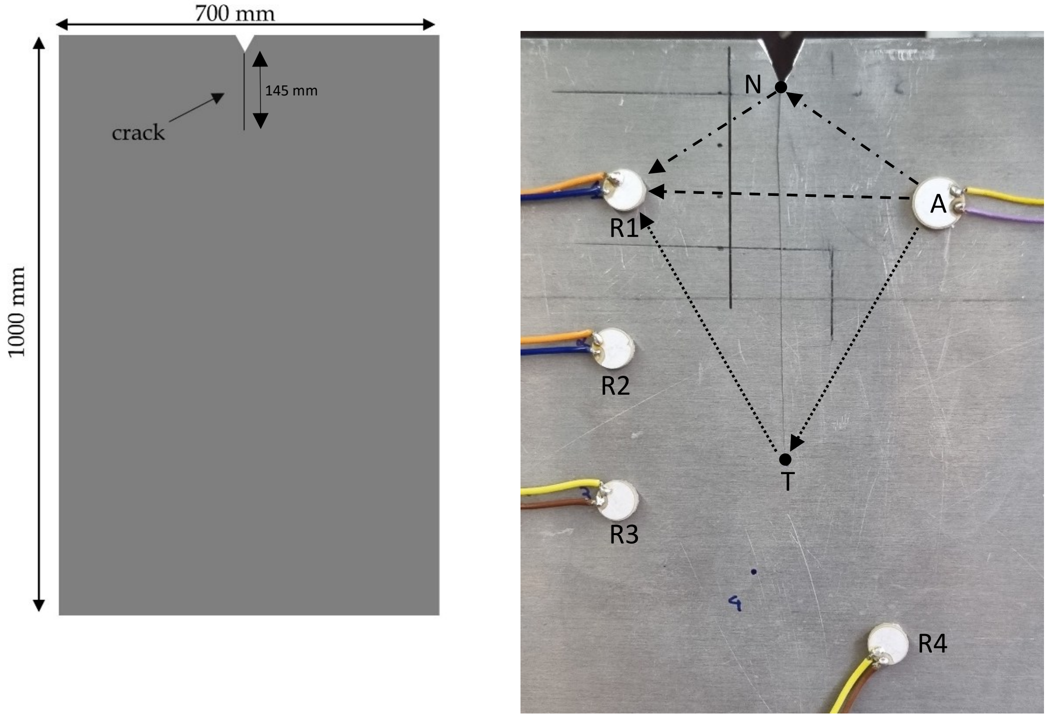

(**a**) (**b**)

Figure 4.26: The test setup for investigating the scattered signal using the arrival time. The distances are listed in Table 4.7. Three possible paths are considered for each pair of the actuator-receiver

A 50 µs length tone burst HF at a central frequency of 150 kHz was applied to the actuators, and the signals were measured at the receivers simultaneously. To estimate the arrival time, the group velocity of the A0-mode lamb wave at 150 kHz is calculated as 2113 $\frac{m}{s}$ in the previous tests, as described in the previous subsection. The distances between the actuator, the notch tip (N), and the crack tip (T) to the receivers are listed in Table 4.7. The predicted arrival time for each possible path between the actuator and the receivers is calculated using Equation 4.8. Figure 4.27 illustrates the measured signal, the signal's envelope, and the predicted arrival times for all receivers. Parameters t_1, t_2 and t_3 in the figures represent the predicted arrival time when the tone burst propagates along between the actuator to a receiver (A-R), the actuator to the crack tip and then to a receiver (A-T-R), and the actuator to the notch tip and then to a receiver (A-N-R), respectively, as plotted in Figure 4.26b.

$$Predicted\ arrival\ time = \frac{Distance}{c_g} \tag{4.8}$$

	A	R1	R2	R3	R4
Actuator (A)		52	62	77	78
notch tip (N)	32.5	32.5	55	81	105
crack tip (T)	58	58	32	30	38

Table 4.7: The list of distances (in mm) between the actuator, the notch tip (N), and the crack tip (T) to the receivers

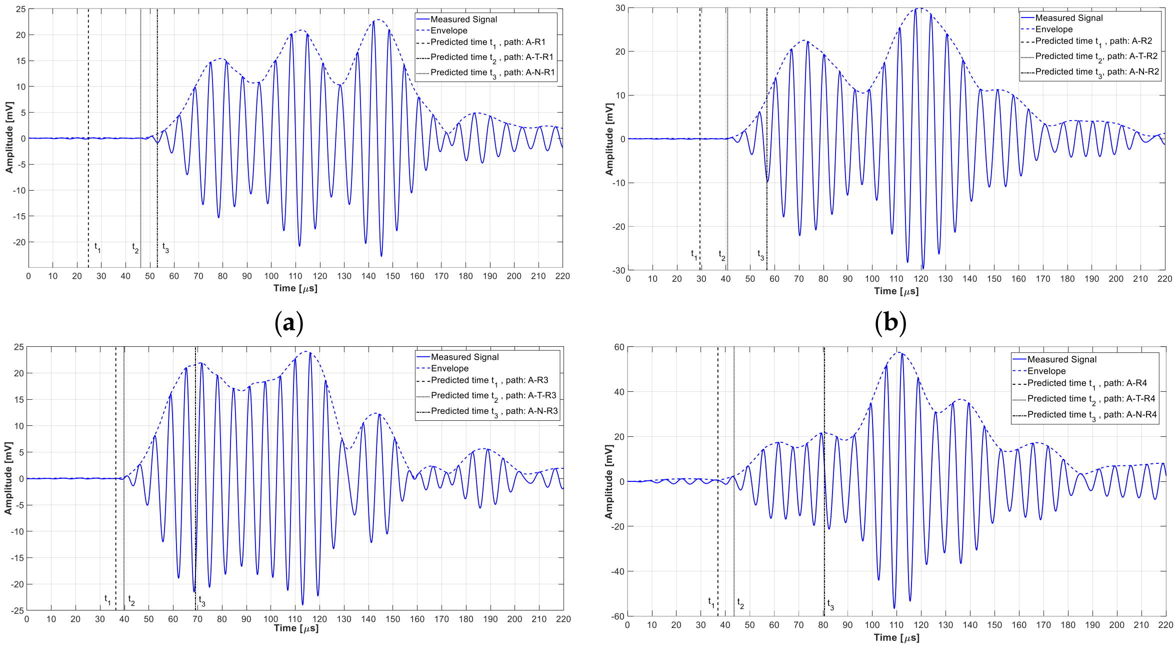

(a) (b)

(c) (d)

Figure 4.27: The measured signal at receivers and predicted arrival times for different paths; (**a**) signal at receiver 1; (**b**) signal at receiver 2; (**c**) signal at receiver 3; (**d**) signal at receiver 4

The measured signal illustrated in Figure 4.27a clearly shows that the approximate arrival time at receiver 1 is longer than the time required to propagate along the direct path between the actuator and the receiver (t1). This delay is attributed to the gap between the crack edges, which causes the received signal to originate from the scattering of the signal at the crack tip. A similar effect is observed in the measured signal at receiver 2, as shown in Figure 2.26b. This behavior differs in the case of receiver 4. There is no obstruction along the direct path between the actuator and the receiver. Therefore, the signal arrival time at this receiver corresponds to the predicted time t1, as illustrated in Figure 4.27d. It is worth mentioning that the scattered signal by the notch edge and the crack tip explains the presence of signal peaks close to predicted arrival times in the measured signal at the receivers.

4.3.6 Crack detection using STFT

As confirmed in the previous subsections, the steady-state and short-time VAM methods can detect nonlinearity in a structure. However, localizing the source of the nonlinearity requires the time history of the sideband amplitude. Thus, the STFT is used to extract the time history at the required frequencies. A test setup was prepared to investigate the crack detection using the STFT.

Three receivers are positioned at the selected distance of 190 mm around an HF actuator on the plate specimen, as shown in Figure 4.28. The direct path from the HF actuator to Receiver 1 crosses the crack at a 90° angle, while the direct path from the HF actuator to Receivers 2 and 3, respectively, does not cross the crack. Also, the position of the LF actuator is shown in the figure. In this test, theoretically, the crack is expected to affect the sideband amplitude received by Receiver 1 most prominently compared to the signals received by Receivers 2 and 3.

In the first measurement, the LF actuators excite a 400 ms signal at 90 kHz, and after 250 ms, the HF actuators excite a tone burst at a central frequency of 175 kHz and a duration of 100 µs. The VAM response, $V_{rk}(t)$, is measured by receivers simultaneously. In the next measurement, only HF was applied to the actuators, and the HF response, $U_{rk}(t)$, measured by receivers. Figure 4.29 shows the measured VAM and HF responses at the receivers.

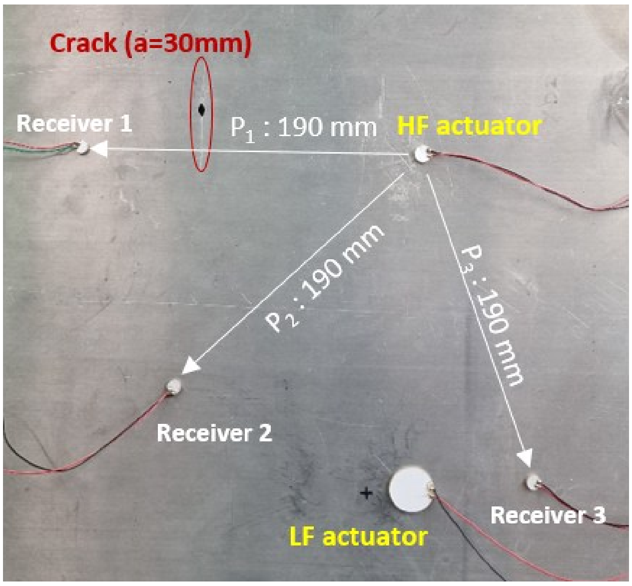

Figure 4.28: Actuator and receiver arrangement adjacent to the crack; Signal sensitivity of the path crossing the defect vs not crossing the defect

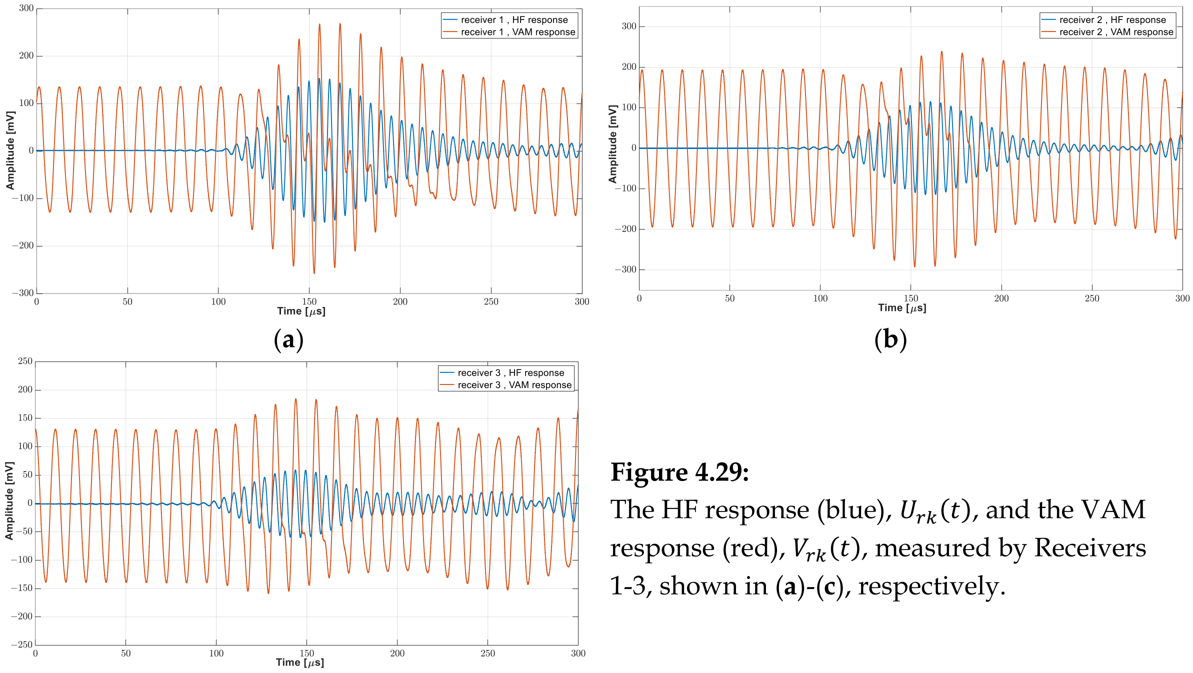

(a) (b)

(c)

Figure 4.29: The HF response (blue), $U_{rk}(t)$, and the VAM response (red), $V_{rk}(t)$, measured by Receivers 1-3, shown in (**a**)-(**c**), respectively.

Figure 4.30a represents the HF response measured by Receiver 1, and Figure 4.30b shows the STFT result of the same signal, where white lines represent the high frequency, $\omega = 175\ kHz$, the low frequency, $\Omega = 90\ kHz$, and the first sideband frequency at $\omega + \Omega = 275\ kHz$. As expected, the STFT plot reveals the highest level of energy at 175 kHz. The energy of the signal at 90 kHz and 275 kHz is almost zero. The normalized HF response in the time domain and the normalized STFT amplitude are illustrated in Figure 4.30c. A is evident in the figure, the peak of the STFT amplitude at 175 kHz matches the peak of the HF response at the corresponding receiver.

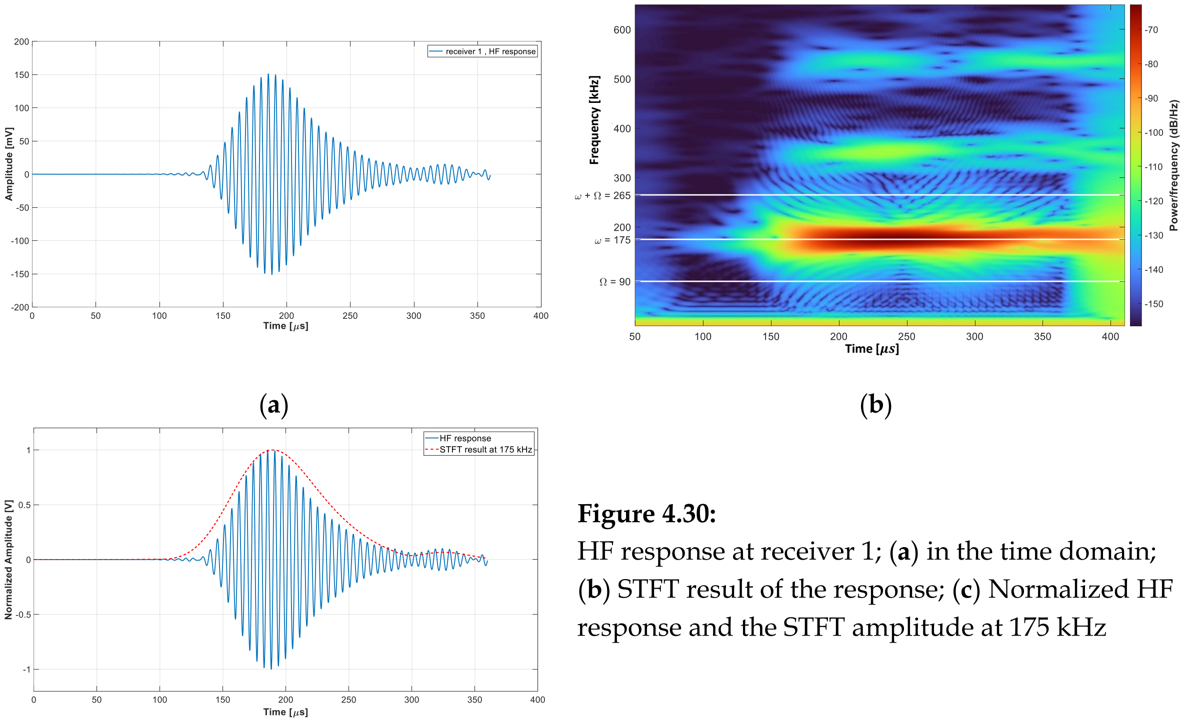

(a) (b)

(c)

Figure 4.30: HF response at receiver 1; (**a**) in the time domain; (**b**) STFT result of the response; (**c**) Normalized HF response and the STFT amplitude at 175 kHz

The STFT results for the VAM response measured at receiver 1 are represented in Figure 4.31, where Figure 4.31a shows the VAM response received at Receiver 1 in the time domain, and Figure 4.31b provides the STFT plot of the corresponding signal. As expected, the STFT plot reveals high energy at the sideband frequency as well as at frequencies ω and Ω.

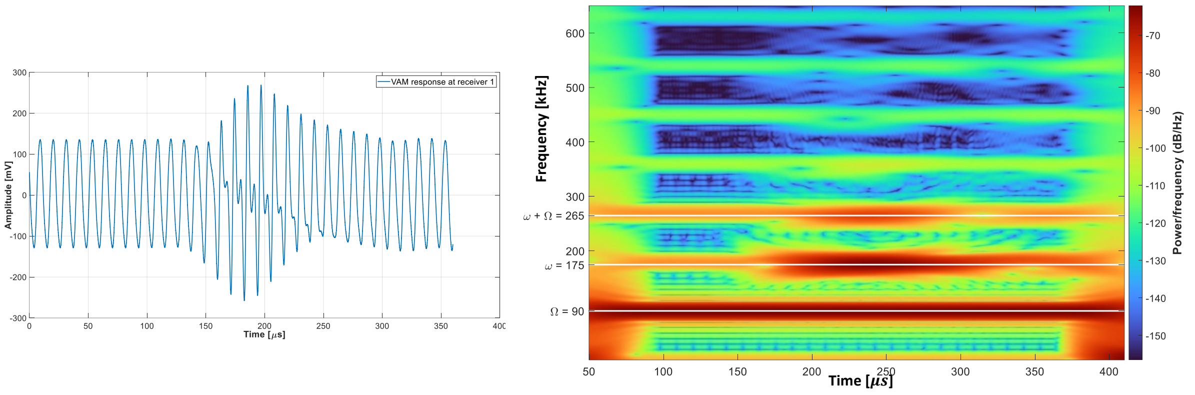

(**a**) (**b**)

Figure 4.31: VAM response at receiver 1; (**a**) in the time domain; (**b**) STFT result of the response

Figure 4.32a-c illustrates the STFT-evaluated amplitude of VAM response at 175 kHz, 90 kHz, and 265 kHz for receivers, respectively. The signal has a constant amplitude at frequency 90 kHz due to the continuously-excited LF signal. Observing the curve progressions, it becomes evident that the sideband frequency at 265 kHz is highly sensitive to the nonlinear defect. However, since the amplitudes of the high- and low-frequency components affect the sideband amplitude, the sideband amplitude must be normalized for better comparison using Equation 4.6. The normalized STFT-evaluated amplitude at the sideband frequency is shown in Figure 4.32d.

In VAM measurement, the signal along Path P1, as annotated in Figure 4.28, between the HF actuator and Receiver 1 through the crack delivers a sideband amplitude peak. Receiver 2 receives a signal along the direct path with no change in sideband amplitude; however, there is a signal contribution along the indirect path that crosses the crack, resulting in a visible increase in sideband amplitude.

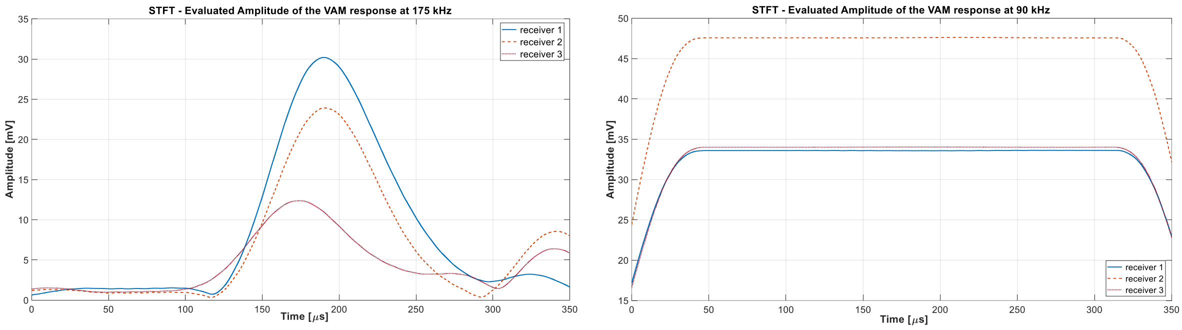

(**a**) (**b**)

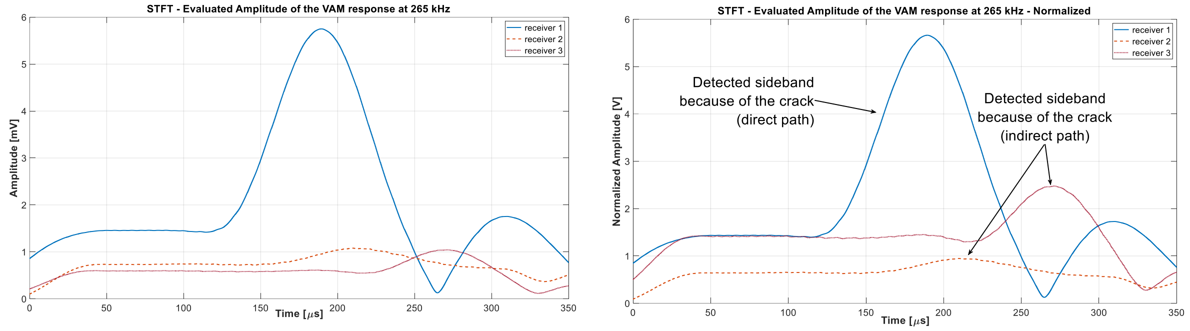

(**c**) (**d**)

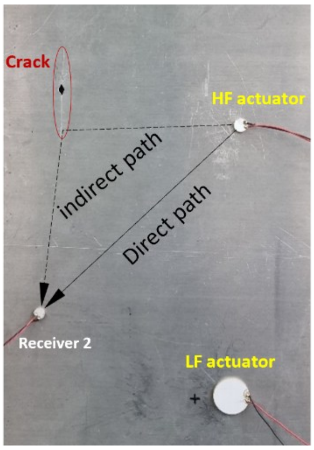

(**e**)

Figure 4.32:
STFT- evaluated amplitude of the VAM response at receivers; (**a**) at 175 kHz; (**b**) at 90 kHz; (**c**) at 265 kHz; (**d**) Normalized amplitude at 265 kHz; (**e**) direct and indirect propagation path for receiver 2

4.3.7 Crack Localization

Previous test results revealed a crucial point essential for localization. A crack localization can be done considering the following facts.

- A source of nonlinearity can be detected using the short-time VAM method, even in cases where the tone burst HF has a short duration.
- A crack or a notch tip scattered the signal like a new source of excitation.
- Since the crack modulates the HF signal and generates the sideband, tracking the scattered signal at the sideband frequency leads us to the source of the nonlinearity.

The localization algorithm described in Figure 3.12 is represented in Figure 4.33a for easier reference to the experimental approaches[1]. A test setup is prepared to experimentally investigate the localization algorithm described in section 3.2. The test setup for localization is shown in Figure 4.33b. A 400 ms S0-mode signal at a low frequency of 69 kHz is excited by two piezoelectric sensors attached to opposite sides of the aluminum plate[2]. After a 350 ms time delay[3], a tone burst HF signal at 175 kHz is excited by another set of sensors at a different location. The duration of the tone burst signal is varied from 50 µs to 150 µs. Simultaneously, the signals are averaged 150 times and saved at four receivers positioned in a symmetrical sensor arrangement, as shown in Figure 4.33. It is emphasized that the defect, which is a

---

[1] Figures 3.13 and 4.33 represent the localization algorithm described in Section 3.2
[2] See Figure 3.10a
[3] The delay is necessary to ensure reaching the steady-state condition for the LF excitation

30 mm crack, is positioned outside the sensor arrangement. The position of the actuators, receivers, and the crack are listed in Table 4.8.

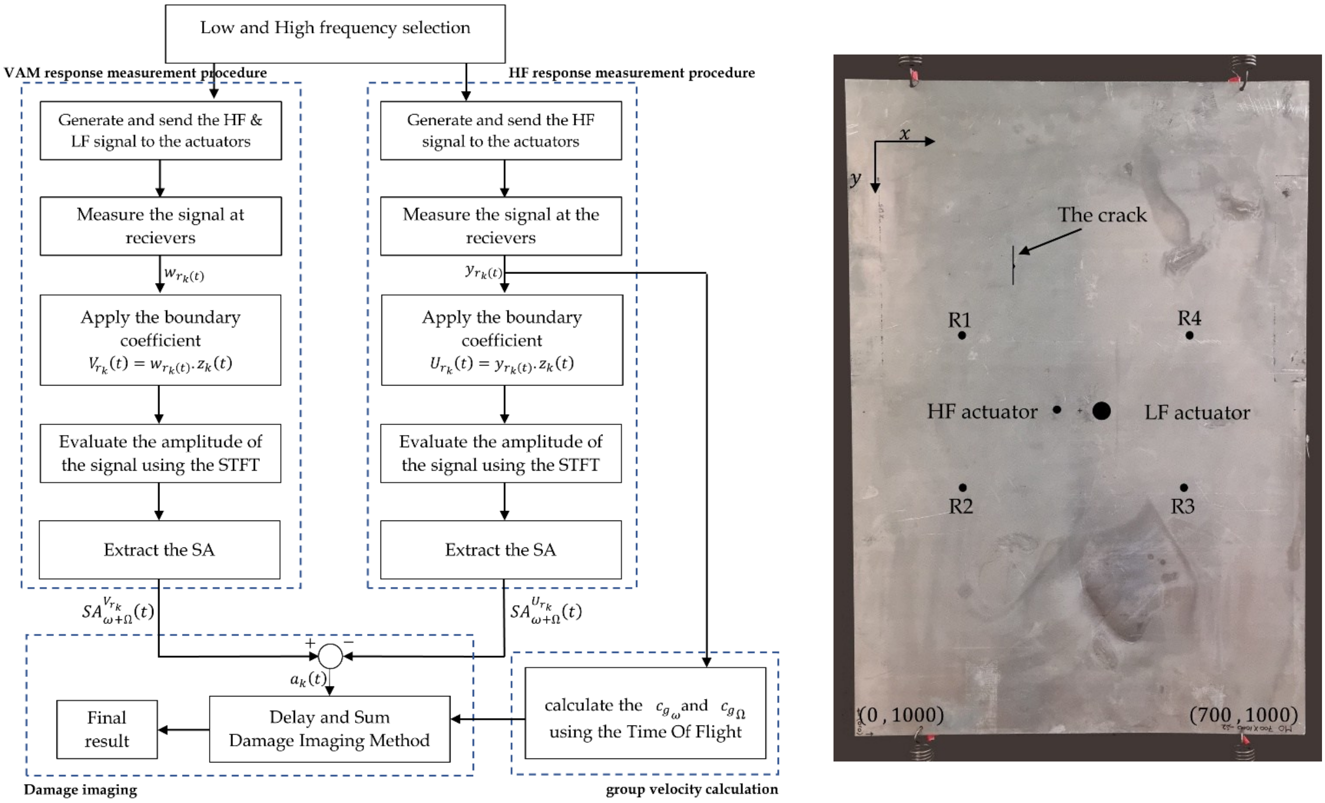

(**a**) (**b**)

Figure 4.33: (**a**) The flowchart of the localization using the VAM method introduced in section 3.2; (**b**) the localization test setup

	x	y
HF actuators	318	500
LF Actuators	380	500
Receiver 1	200	404
Receiver 2	202	600
Receiver 3	500	598
Receiver 4	499	398
The crack	250	245-313

Table 4.8: The position of the actuators, receivers, and the crack on the plate for the symmetric arrangement of receivers

For each potential crack coordinate of (x, y), the estimated time between the actuators, the potential crack, and a receiver k, t_{sXrk} is calculated using Equation 3.36d[1]. The SA that is read out of $a_k(t)$ is assign to $f_k(x, y)$, which is given in Equation 4.9, where k refers to the receiver number. Repeating this procedure for all coordinates of the grid of the sample plate essentially gives the potential coordinates for the defect positioned on an ellipse. The ellipses assessed

---

[1] $t_{sXr1} = \frac{\sqrt{(x_S-x)^2+(y_S-y)^2}}{c_{g_\omega}} + \frac{\sqrt{(x-x_{r1})^2+(y-y_{r1})^2}}{c_{g_{\omega+\Omega}}}$

for receivers R1-R4 are shown in Figure 4.34, respectively, when the duration of the tone burst HF is selected to be 100 µs. The yellow ellipse marks the potential locations of the defect.

$$f_k(x,y) = a_k\big(t_{sXrk}(x,y)\big) \tag{4.9}$$

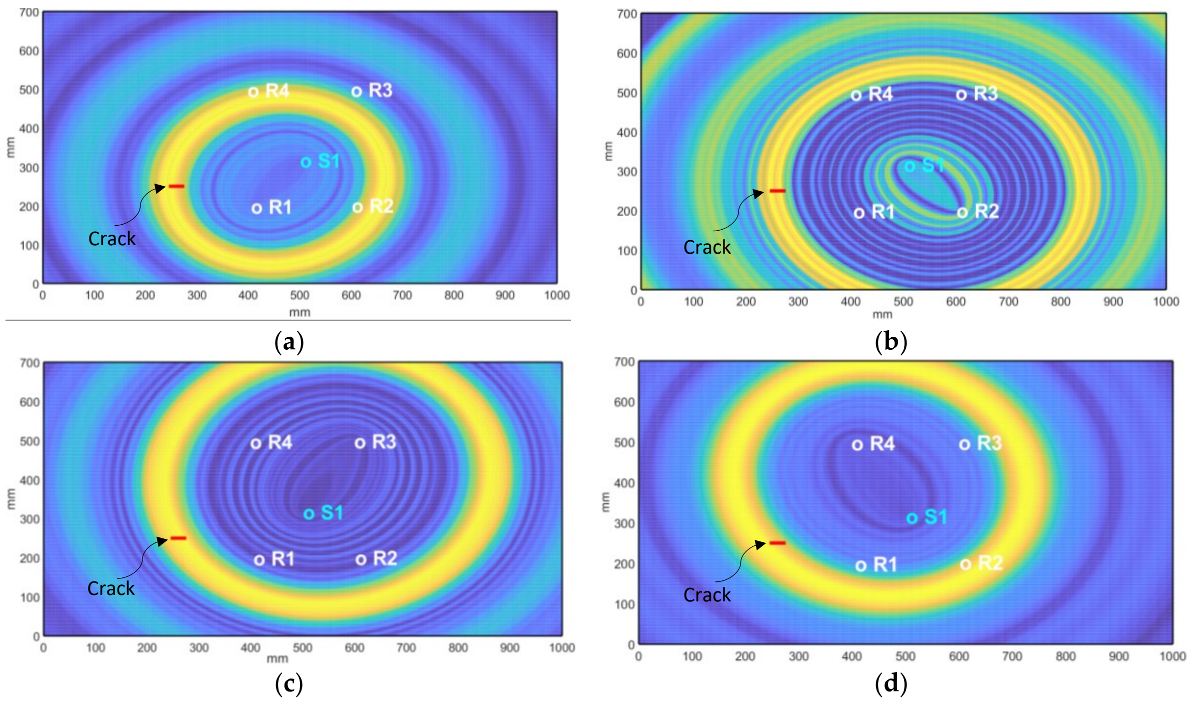

(**a**) (**b**)

(**c**) (**d**)

Figure 4.34: Damage imaging (DI) for each sender-receiver pair, when the duration of the tone burst was 100 µs: (**a**) DI for the S1-R1 pair; (**b**) DI for the S1-R2 pair; (**c**) DI for the S1-R3 pair; (**d**) DI for the S1-R4 pair. The red line indicates the position of the crack. Frequencies: LF: 69 kHz; HF: 175 kHz.

A single contour plot of the sideband amplitude $f(x,y)$ is created by overlaying the ellipses (Figures 4.34a-d), revealing the position of the defect on the plate. The final damage imaging is calculated by Equation 4.10 and visualized in Figure 4.35. The results demonstrate that the localization algorithm accurately locates the area of nonlinearity, very close to the actual crack, with a=30 mm.

$$f(x,y) = \prod_{k=1}^{4} f_k(x,y) \tag{4.10}$$

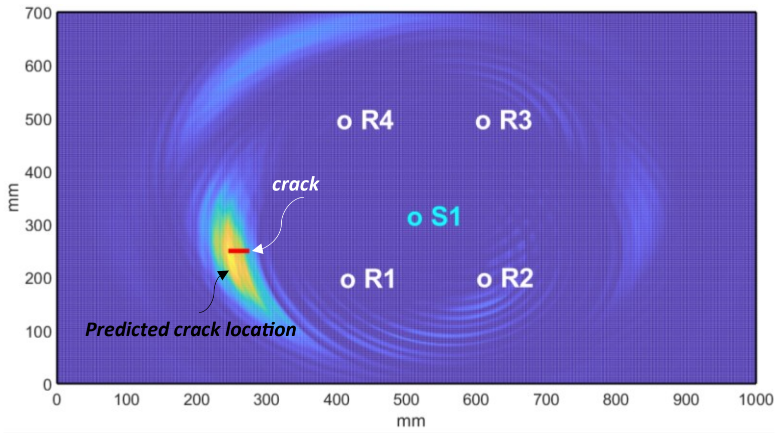

Figure 4.35: The final overlaying DI reveals the accurate location of the crack, where the duration of the tone burst HF is 100 µs. The red line indicates the position of the crack.

4.3.7.1 Crack localization and the Tone Burst Duration

The tone burst duration appears to be a crucial parameter in crack localization. A too-long tone burst duration essentially causes overlap of reflected signals, compromising the first-arrived signal. In contrast, a too-short tone burst duration provides not enough energy input to make the nonlinearity recognizable. Hence, it is explored a) whether a longer signal duration improves the quality of localization results concerning SA magnitude, and, if this is the case, b) how short the tone burst duration can be selected.

The test setup, as shown in Figure 4.33b, is used for the symmetric sensor arrangement. The tone burst durations are varied between 50 µs, 75 µs, 125 µs, and 150 µs. Figures 4.36a-d prove that a longer tone burst duration increases the SA magnitude, resulting in a more intense DAS marking. However, it is noted that the area of the defect mark increases with the duration of the tone burst. It is concluded that the benefits of longer tone burst durations are limited, and a tone burst duration of 50 µs already provides satisfying results. A shorter tone burst duration diminishes the outcome due to insufficient energy entry and does not yield acceptable results.

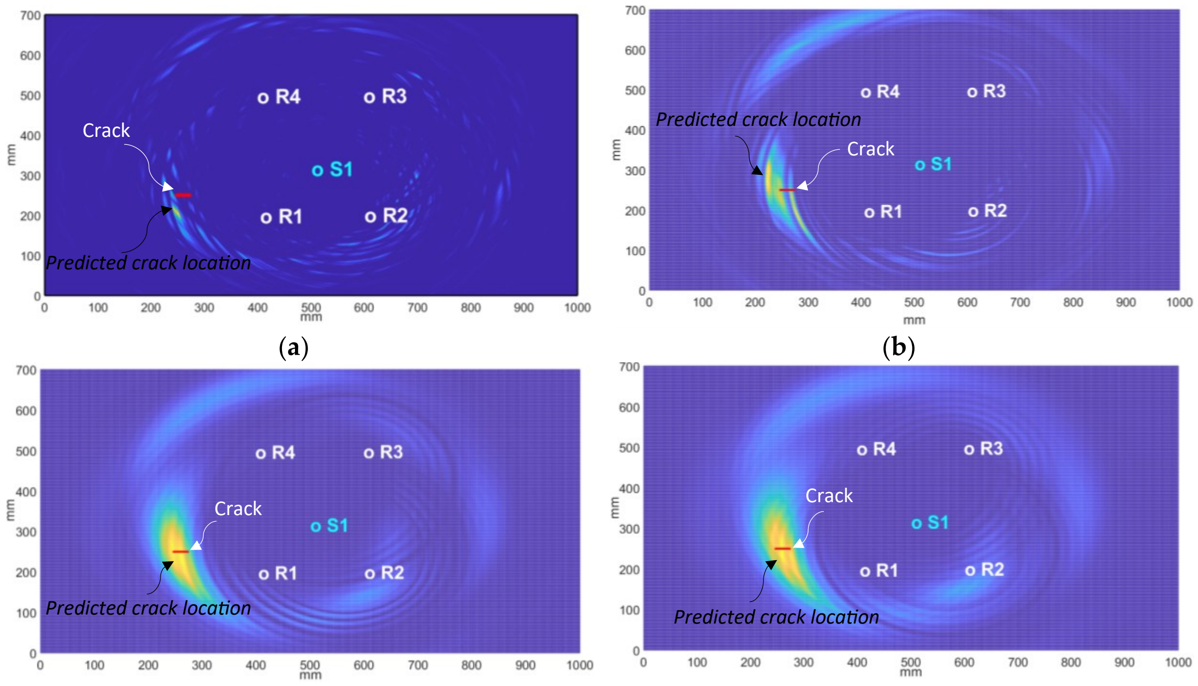

(a) (b)

(c) (d)

Figure 4.36: Localization result for different tone burst durations and the symmetric arrangement of receivers; (**a**) 50 µs duration; (**b**) 75 µs duration; (**c**) 125 µs duration; (**d**) 150 µs duration - crack position indicated by red line - Frequencies: LF: 69 kHz and HF: 175 kHz.

4.3.7.2 Nonsymmetric arrangement of sensors

The same test setup, as represented in Figure 4.33b, is prepared with a nonsymmetric arrangement of the receivers. The position of the receivers in this test is listed in Table 4.9. The selected frequency for the LF signal in this test is 76.5 kHz. A tone burst HF signal at a central frequency of 175 kHz with durations of 100, 125, and 150 µs is applied after a delay of 350 µs. The results of the localization are illustrated in Figure 4.37. The test outcome clearly shows that a symmetric arrangement of the receiver is not required and does not affect the measurement outcome.

	x in mm	y in mm
HF actuators	318	500
LF Actuators	375	500
Receiver 1	173	356
Receiver 2	253	723
Receiver 3	521	653
Receiver 4	582	337
The crack	250	245-313

Table 4.9: The position of the actuators, receivers, and the crack on the plate for the nonsymmetric arrangement of receivers

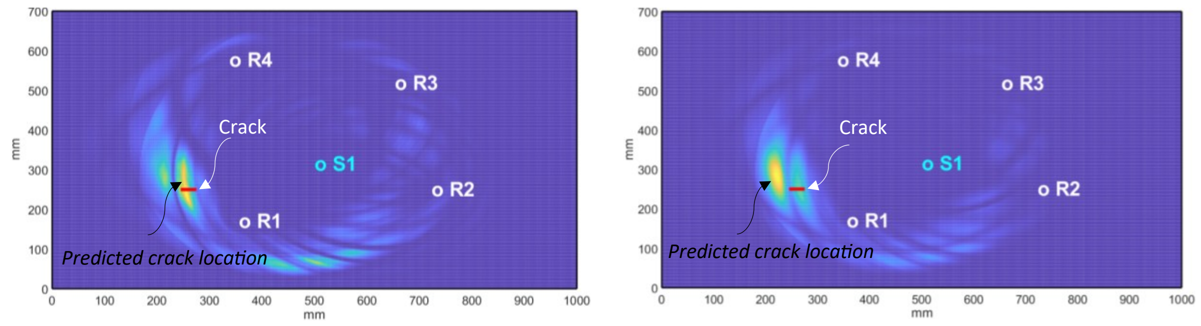

(**a**) (**b**)

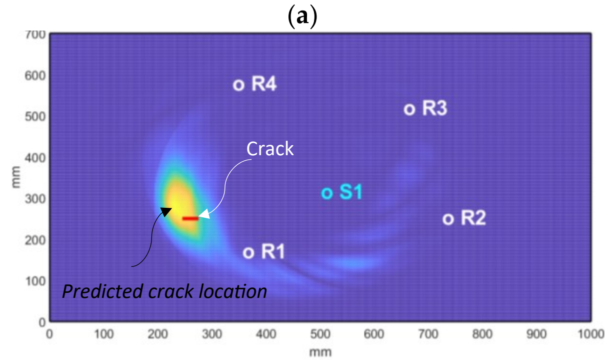

(**c**)

Figure 4.37:
Localization result for different tone burst durations and the nonsymmetric arrangement of receivers; (**a**) 100 µs duration; (**b**) 125 µs duration; (**c**) 150 µs duration - crack position indicated by red line
Frequencies: LF: 76.5 kHz and HF: 175 kHz

4.3.7.3 Diamond-like arrangement of sensors

The same test setup, as represented in Figure 4.33b, is prepared with a diamond-like arrangement of the receivers. The position of the receivers in this test is listed in Table 4.10. The selected frequency for the LF signal in this test is 77 kHz. A tone burst HF signal at a central frequency of 175 kHz with durations of 100, 125, and 150 µs is applied after a delay of 350 µs. The results of the localization are illustrated in Figure 4.38. The localization results demonstrate that the crack location was accurately localized in this arrangement. The localization results for different kinds of receiver arrangements clearly demonstrate that the localization algorithm is independent of the receiver arrangement. Important factors in the localization process are the frequency of the LF signal and the duration of the tone burst HF signal.

	x in mm	y in mm
HF actuators	318	500
LF Actuators	380	500
Receiver 1	350	398
Receiver 2	202	500
Receiver 3	350	600
Receiver 4	500	498
The crack	250	245-313

Table 4.10: The position of the actuators, receivers, and the crack on the plate for the diamond-like arrangement of receivers

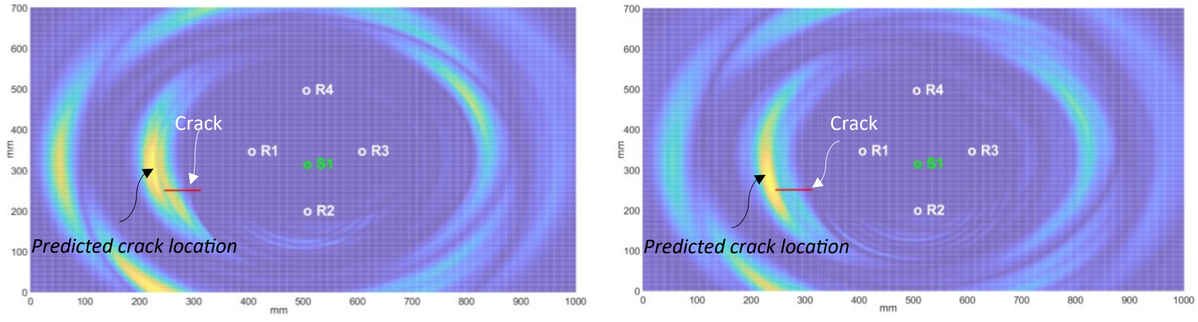

(**a**) (**b**)

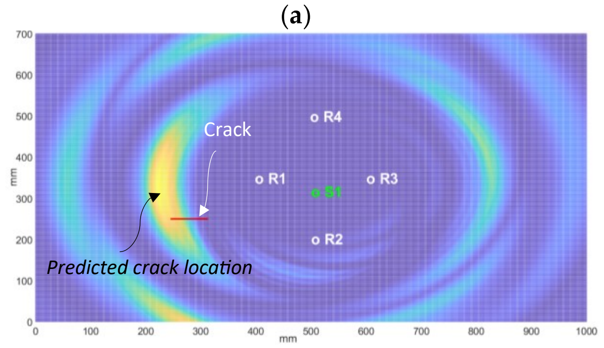

(**c**)

Figure 4.38:
Localization result for different tone burst durations and the diamond-like arrangement of receivers; (**a**) 100 µs duration; (**b**) 125 µs duration; (**c**) 150 µs duration - crack position indicated by red line
Frequencies: LF: 77 kHz and HF: 175 kHz

4.3.7.4 The Localization error

The measurements reveal a difference between the actual crack location and the predicted crack location, which is defined as localization error. Equation 4.11 provides an assessment of the distance between the actual and predicted crack location using the coordinates of the predicted crack, $(x_p\ ,\ y_p)$, and the actual crack, $(x_c\ ,\ y_c)$. Table 4.11 lists the distances from the predicted crack locations to the crack tips as well as the center of the crack for the measurement scenarios shown in Figures 4.35, 4.36, 4.37, and 4.38. The last column of Table 4.11 represents the localization error ratio in respect to the sample dimensions in [%], assessed by Equation 4.12, where X_{max} and Y_{max} are the sample dimensions 700 mm and 1000 mm, respectively.

$$Err_{Loc} = \sqrt{\left(x_p - x_c\right)^2 + \left(y_p - y_c\right)^2} \qquad (4.11)$$

$$Err_{Loc}\% = \sqrt{\left(\frac{x_p - x_c}{X_{max}}\right)^2 + \left(\frac{y_p - y_c}{Y_{max}}\right)^2} \times 100\,\% \tag{4.12}$$

ω [kHz]	Ω [kHz]	Tone burst duration [μs]	Localization error [mm]				Localization error ratio [%]
			to the right crack tip	to the center of the crack	to the left of the crack tip	Average	Average
175	69	50	41.05	43.01	49.65	44.57	6.12
		75	37.8	48.41	60.9	49.04	5.8
		100	11.18	14.14	26.93	17.42	2.05
		125	8.06	17.88	32.02	19.32	2.14
		150	17.00	2.00	13.00	10.67	1.07
	76.5	100	16.28	12.65	22.47	17.13	2.12
		125	41.04	50.99	62.97	51.67	6.24
		150	29.93	34.06	45.22	35.40	4.45
	77	100	94.15	67.18	49.73	70.35	8.63
		125	75.26	45.22	16.64	46.71	4.96
		150	112.54	90.43	77.47	93.48	12.18

Table 4.11: The list of localization errors

4.4 Chapter summary

This chapter presented the experimental validation of the two principal contributions of this study: (1) the MI separation algorithm using the newly proposed model, and (2) the localization of real cracks in an aluminum plate using the short-time Vibro-Acoustic Modulation (VAM) method.

For MI separation, the VAM response was analyzed using both the amplitude-frequency modulation (AFM) and the amplitude-frequency-phase modulation (AFPM) models. Experimental results demonstrated that the proposed separation algorithms accurately estimate the modulation indices, even in the presence of non-modulated carrier (NMC) components. The AFPM model, in particular, successfully captured phase shift variations in the VAM response that the AFM model could not explain, providing strong support for its theoretical formulation. Additionally, the comparison between the DMI and θ_{AngM} curves illustrates that the θ_{AngM} curve can reveal changes in MIs earlier than the DMI curve at some frequencies. However, these results should not be interpreted as evidence of the overall superiority of phase over the DMI. The findings demonstrate that combining phase and amplitude variation analysis can enhance the sensitivity to structural changes, often revealing variations more prominently than the amplitude-based approach alone.

In the second part, the short-time VAM method was experimentally applied for defect localization. The method uses a continuous LF excitation and a tone-burst HF signal to isolate nonlinear sideband components generated by defects. The crack modulated the HF wave, and this modulated component was detectable using the Short-Time Fourier Transform (STFT). The Delay-and-Sum (DAS) imaging method was then applied to the extracted sideband amplitude to localize the crack. Results showed that even short-duration tone bursts (50 µs) yielded successful localization, and the method remained robust for both symmetric and nonsymmetric sensor configurations. Notably, cracks located outside the sensor arrangement could still be detected and localized with high accuracy.

Chapter 5

Summary and Outlook

Two different topics were studied in this research: (1) the separation of modulation indices (MI), and (2) the localization of real cracks using the Vibro-Acoustic Modulation (VAM) method. After providing a literature review of the current state of research on both topics, this study introduces experimental studies on the MI separation and the localization of a real crack in a metal plate.

5.1 Modulation Indices Separation

5.1.1 The represented study

The objective of this part of the study was to enhance the mathematical representation of the VAM response terms, commonly referred to as sidebands, using established modulation models. Two models were described and compared in this study: (1) the amplitude-frequency modulated (AFM) model, which researchers commonly use for the MI separation algorithms, and (2) the amplitude-frequency-phase modulated (AFPM) model, which is described for the first time in this study. In contrast with the AFM model, the AFPM model explains the phase-shift variations corresponding to changes in the MIs, which are also evident in experimental observations. Furthermore, the sensitivity analysis of the damage modulation index (DMI) and phase shifts shows that the relative sensitivity of the phase shift is higher than that of the DMI.

Considering a non-modulated carrier (NMC) in the measured response distorts and invalidates results obtained with fundamental approaches, such as the Hilbert Transform (HT). Therefore, the focus of this work was to enhance an MI separation algorithm in the presence of the NMC using the first and second sidebands. The results of the MI separation algorithm and phase shift extraction reveal the following interesting findings:

- The experimental results show that the phase shift of the sedebands changes over lifetime, indicating that the phase shift of the frequency components varies with the changes in MIs. The phase shift change is predicted and described mathematically using the AFPM model. The AFM model, however, cannot describe changes in phase shifts.

- The results clearly demonstrate that, at specific frequencies, the angle modulation phase shift (θ_{AngM}) is capable of revealing larger variations than the MDI at earlier stages. The findings demonstrate that combining phase and amplitude variation analysis can enhance sensitivity to structural changes.

- The proposed separation algorithms for both AFM and AFPM models can accurately estimate the MIs, theoretically, despite the existence of the NMC in the measured response.
- By using the ratio of the sideband amplitudes or powers, the proposed MI separation algorithms are independent of the HF signal amplitude. However, the estimated MIs are dependent on LF amplitude. In fact, all separation algorithms estimate the product of the LF amplitude and MIs.

- The MI separation results of the AFM model do not confirm that, when either m_a or m_f is smaller than the other at the beginning of the crack growth, and becomes larger at the final phase of crack growth. However, the results revealed that both m_a and m_f are increased simultaneously, with varying amounts of the increase.

- Despite the accuracy of the represented MI separation algorithms in estimating the MIs, the values of the MIs are sensitive to the response measurement due to their small magnitude. Therefore, a high level of noise in an experimental measurement can contaminate the estimated MIs.

5.1.2 Directions for future studies

The following directions are suggested for further research regarding the MI separation algorithm:

- *MI separation using AI*
  Design and train an Artificial Neural Network (ANN), or any other deep learning method, using the simulation results, and use it to estimate the MIs in the experimental measurement.

- *MI separation using statistical tools*
  Since the measured signal can be compromised by noise or other sources of uncertainty, a combination of mathematical and statistical tools can be used to estimate the range of the MIs, rather than their specific values.

5.2 Defect localization using the short-time VAM

5.2.1 The represented study

The goal of this part of the study was to develop a method for crack localization using the VAM method. The defect localization algorithm addresses the following existing challenges in defect localization:

- Since an adjacent piezoelectric sensor might compromise the direct signal, the number of receivers is minimized, and a narrow grid of piezoelectric sensors is avoided.
- The capability of the algorithm to localize a defect positioned outside of the arrangement of receiving piezoelectric sensors.

- Assessment of other sources of nonlinearity, such as nonlinear signal contributions from measuring equipment, to enable the measurement of pure defect-related signals.
- Consideration of reflected signals compromising the direct signal.
- The effect of tone burst signal duration on the accuracy of the defect localization.
- The dependence of defect localization outcome on the symmetric or nonsymmetric arrangement of receivers.
- The independence of the defect localization method from a baseline measurement makes it attractive for practical use.

To achieve these goals, the proposed defect localization algorithm combines VAM detection theory and traditional damage imaging. Tracking the signal at sideband frequency $\omega+\Omega$, hence, focusing on nonlinear signals, is used for localization using four receivers at arbitrary positions on an aluminum plate in an experimental setup. A S0-mode LF and an A0-mode HF signal are excited simultaneously as a continuous and a tone burst signal, respectively. This method is referred to as the short-time VAM method in this research. A Short-Time Fourier Transform (STFT) is applied to received signals, and the amplitude at $\omega+\Omega$ is used for localization. The Delay and Sum (DAS) damage imaging method is used to graphically display the location of cracks. The following interesting aspects influenced the progress of the localization algorithm:

- Comparison of the direct signal passing through a real crack and not passing through a real crack confirms that the presence of a crack has a significant influence on generating a signal at the sideband frequency $\omega + \Omega$.

- The tip of the crack or the notch scattered the tone burst signal in all directions, causing it to act like a new source of excitation. The scattered signal was illustrated visually using the Laser Doppler Vibrometer (LDV-Psv-500, Polytec).

- Since the crack generates the signal at the sideband frequency $\omega + \Omega$, the scattered signal contains the sideband. Tracking the scattered signal reveals the location of the nonlinearity, in this case, a crack. The sideband generated by the crack is detectable on either a direct or an indirect path, with a time delay related to the distance between the defect and the receiver.

- The results of the localization algorithm indicate that the real crack is localized with high accuracy when the duration of the HF tone burst is at least 50 μs in the selected experimental setup. A shorter tone burst duration would prevent localization due to insufficient energy input, while a longer tone burst duration would negatively affect defect localization resolution.

- The results of the localization algorithm indicate that any arrangement of piezoelectric sensors within the maximum limits yields the same quality of defect localization, and neither a symmetric nor a nonsymmetric arrangement of sensors provides an advantage in terms of signal quality.

- The algorithm introduced allows defect location when the defect is positioned outside the arrangement of sensors.

5.2.2 Direction for future studies

The following topics are suggested for further research regarding the defect localization algorithm:

- *The possibility of exciting a soliton wave in metal*
  Localizing the faraway cracks is a big challenge for engineers, since the tone burst signal loses energy during propagation. The possibility of sending a specific type of waveform over a longer distance is an interesting research topic. This type of waveform exists in certain materials, such as water, known as the soliton wave, which can travel over extremely long distances without losing energy. The existence of a soliton wave depends on nonlinear terms in the wave equation in the propagating material. In metals, however, the wave equation is not inherently nonlinear, and a nonlinear term must be explicitly added to the equations.

- *Smart Defect Detection*
  In real-world conditions, the dimensions of a monitored structure may be so large that even the deployment of multiple parallel defect localization systems cannot fully cover the entire structure. As a proposed approach, inspection can be limited to regions where the probability of crack presence is higher. In this case, by focusing the high-frequency signal on these areas, the presence and strength of sideband components in the reflected signal can be analyzed, taking into account the propagation speed of the signals within the structure.

Appendix A

The SPHS algorithm

The Sweeping-Phase Homodyne Separation (SPHS) algorithm [38, 39] is a developed In-phase/Quadrature Homodyne Separation (IQHS) algorithm [38, 39] to calculate the amplitude and phase modulation indices when the measured signal has an arbitrary phase shift, as illustrated in Figure A.1. Additionally, this algorithm can separate the modulation indices in the presence of the non-modulated carrier in the measured system response.

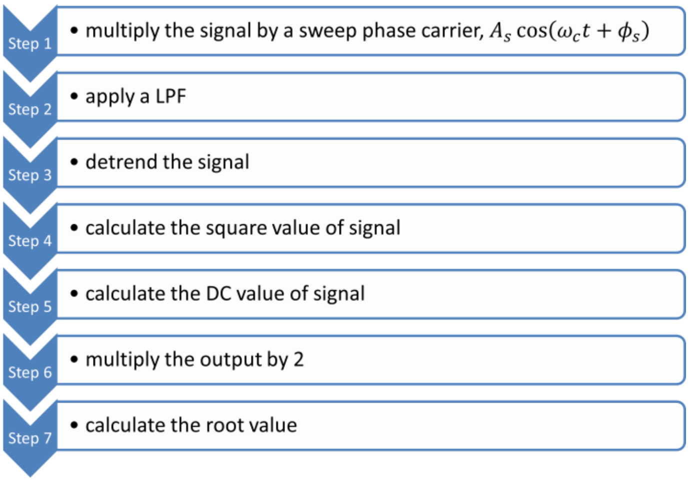

Figure A.1: The SPHS algorithm

Assume that the measured response signal, $y(t)$, can be expanded as Equation A.1, where A_k and A_{nm} represent the amplitude of sidebands and the non-modulated signal part, respectively. The output of every SPHS step is described below:

$$\begin{aligned} y(t) = {} & A_0\, cos(\omega_c t + \phi_c - \phi_0) && \text{a} \\ & +A_{+1}\, cos\left((\omega_c + \omega_d)t + \phi_c + \phi_d - \phi_{M_{+1}}\right) && \text{b} \\ & +A_{-1}\, cos\left((\omega_c - \omega_d)t + \phi_c - \phi_d - \phi_{M_{-1}}\right) && \text{c} \\ & +other\ terms\ (LF\ and\ HF\ harmonics, other\ sidebands) && \text{d} \\ & +A_{nm}\, cos(\omega_c t + \phi_{nm}) && \text{e} \end{aligned} \tag{A.1}$$

- ***Step 1:*** *Multiply the measured signal by* $A_s\, cos(\omega_c t + \phi_s)$

$$y_1(t) = A_s \cos(\omega_c t + \phi_s) \cdot y(t)$$

$$= A_s A_0 \left(\frac{1}{2} cos(2\omega_c t + \phi_s + \phi_c - \phi_0) + \frac{1}{2} cos(\phi_c - \phi_0 - \phi_s)\right)$$

$$+A_s A_{+1} \left(\frac{1}{2} cos\left[(2\omega_c + \omega_d)t + \phi_c + \phi_s + \phi_d - \phi_{M_{+1}}\right] + \frac{1}{2} cos\left(\omega_d t + \phi_c + \phi_d - \phi_{M_{+1}} - \phi_s\right)\right)$$

$$+A_sA_{-1}\left(\frac{1}{2}cos\left[(2\omega_c-\omega_d)t+\phi_c+\phi_s-\phi_d-\phi_{M_{-1}}\right]+\frac{1}{2}cos\left(\omega_d t-\phi_c+\phi_d+\phi_{M_{-1}}+\phi_s\right)\right)$$

$$+Other\ Terms\ with\ frequencies\ (2\omega_c\pm k\omega_d\ ,k\omega_d)$$

- ***Step 2:*** *Filtering the signal using a low-pass filter with ω_d cutoff frequency*

$$y_2=LPF_{\omega_d}\{y_1\}$$

$$=\frac{1}{2}A_sA_0\cos(\phi_c-\phi_0-\phi_s-\phi_{LPF})$$

$$+\frac{1}{2}A_sA_{+1}\cos\left(\omega_d t+\phi_c+\phi_d-\phi_{M_{+1}}-\phi_s-\phi_{LPF}\right)$$

$$+\frac{1}{2}A_sA_{-1}\cos\left(\omega_d t-\phi_c+\phi_d+\phi_{M_{-1}}+\phi_s-\phi_{LPF}\right)$$

- ***Step 3:*** *Detrending the signal (delete the DC value of the signal)*

$$y_3=Detrend\{y_2\}$$

$$=\frac{1}{2}A_sA_{+1}\cos\left(\omega_d t+\phi_c+\phi_d-\phi_{M_{+1}}-\phi_s-\phi_{LPF}\right)$$

$$+\frac{1}{2}A_sA_{-1}\cos\left(\omega_d t-\phi_c+\phi_d+\phi_{M_{-1}}+\phi_s-\phi_{LPF}\right)$$

- ***Step 4:*** *Calculate the square value of the signal*

$$y_4={y_3}^2$$

$$=\left(\frac{1}{2}A_sA_{+1}\right)^2\left(\frac{1}{2}+\frac{1}{2}cos\left(2\omega_d t+2\phi_c+2\phi_d-2\phi_{M_{+1}}-2\phi_s-2\phi_{LPF}\right)\right)$$

$$+\left(\frac{1}{2}A_sA_{-1}\right)^2\left(\frac{1}{2}+\frac{1}{2}cos\left(2\omega_d t-2\phi_c-2\phi_d+2\phi_{M_{-1}}+2\phi_s-2\phi_{LPF}\right)\right)$$

$$+2\left(\frac{1}{2}A_sA_{+1}\right)\left(\frac{1}{2}A_sA_{-1}\right)\left(\frac{1}{2}cos\left(2\phi_c-2\phi_s-\phi_{M_{+1}}-\phi_{M_{-1}}\right)\right)$$

$$+2\left(\frac{1}{2}A_sA_{+1}\right)\left(\frac{1}{2}A_sA_{-1}\right)\left(\frac{1}{2}cos\left(2\omega_d t+2\phi_d-\phi_{M_{+1}}+\phi_{M_{-1}}-2\phi_{LPF}\right)\right)$$

- ***Step 5:*** *Calculate the DC value of the signal*

$$y_5=DC\{y_4\}$$

$$=\frac{1}{2}{A_s}^2\left(\frac{1}{2}A_{+1}\right)^2$$

$$+\frac{1}{2}{A_s}^2\left(\frac{1}{2}A_{-1}\right)^2$$

$$+2\frac{1}{2}{A_s}^2\left(\frac{1}{2}A_{+1}\right)\left(\frac{1}{2}A_{-1}\right)cos\left(2\phi_c-2\phi_s-\phi_{M_{+1}}-\phi_{M_{-1}}\right)$$

- ***Step 6:*** *Multiply the signal by 2*

$$y_6=2y_5$$

$$={A_s}^2\left(\frac{1}{2}A_{+1}\right)^2$$

$$+{A_s}^2\left(\frac{1}{2}A_{-1}\right)^2$$

$$+2{A_s}^2\left(\frac{1}{2}A_{+1}\right)\left(\frac{1}{2}A_{-1}\right)cos\left(2\phi_c-2\phi_s-\phi_{M_{+1}}-\phi_{M_{-1}}\right)$$

- ***Step 7:** Calculate the root value*

$$y_7=\sqrt{y6}$$

$$=A_s\sqrt{\left(\frac{1}{2}A_{+1}\right)^2+\left(\frac{1}{2}A_{-1}\right)^2+2\left(\frac{1}{2}A_{+1}\right)\left(\frac{1}{2}A_{-1}\right)cos\left(2\phi_c-2\phi_s-\phi_{M_{+1}}-\phi_{M_{-1}}\right)} \qquad \text{(A.2)}$$

To evaluate the maximum and minimum values of the final output of the SPHS, as presented in Equation A.2, the following two general cases can be considered:

- *when* $cos\left(2\phi_c-2\phi_s-\phi_{M_{+1}}-\phi_{M_{-1}}\right)=1$

$$SPHS_{max}=A_s\sqrt{\left(\frac{1}{2}A_{+1}\right)^2+\left(\frac{1}{2}A_{-1}\right)^2+2\left(\frac{1}{2}A_{+1}\right)\left(\frac{1}{2}A_{-1}\right)}$$

$$SPHS_{max}=A_s\sqrt{\left(\frac{1}{2}A_{+1}+\frac{1}{2}A_{-1}\right)^2}$$

$$SPHS_{max}=A_s\frac{|A_{+1}+A_{-1}|}{2} \qquad \text{(A.3)}$$

$$\phi_{s_{max}}=\phi_c-\frac{\phi_{M_{+1}}+\phi_{M_{-1}}}{2} \qquad \text{(A.4)}$$

- *when* $cos\left(2\phi_c-2\phi_s-\phi_{M_{+1}}-\phi_{M_{-1}}\right)=-1$

$$SPHS_{min}=A_s\sqrt{\left(\frac{1}{2}A_{+1}\right)^2+\left(\frac{1}{2}A_{-1}\right)^2-2\left(\frac{1}{2}A_{+1}\right)\left(\frac{1}{2}A_{-1}\right)}$$

$$SPHS_{min}=A_s\sqrt{\left(\frac{1}{2}A_{+1}-\frac{1}{2}A_{-1}\right)^2}$$

$$SPHS_{min}=A_s\frac{|A_{+1}-A_{-1}|}{2} \qquad \text{(A.5)}$$

$$\phi_{s_{min}}=-\frac{\pi}{2}+\phi_c-\frac{\phi_{M_{+1}}+\phi_{M_{-1}}}{2} \qquad \text{(A.6)}$$

As evident in the above equations (A.3 and A.5), the maximum and minimum of the SPHS output correspond to the sum and difference of the first sideband amplitudes, respectively, which can be calculated more quickly using the FFT.

Appendix B

The Retavie Sensitivity of DMI and Phase Shifts

The mathematical equations for the relative sensitivity analysis of the Damage Modulation Index (DMI), $DMI(m_a, m_f, m_p)$, and the summation of the first sideband phase shifts, $\Phi(m_a, m_f, m_p)$ in detail are represented here. All required equations for the relative sensitivity previously introduced in Table 2.7 are recalled in Table B.1 for better readability. For simplicity, the value of the initial phase shifts of the HF signal, ϕ_ω, and the LF signal, ϕ_Ω, assumed to be zero in the following relations.

$A_0 = A_\omega\sqrt{(a_0)^2 + (b_0)^2}$	$\theta_0 = -\,tan^{-1}\left(\frac{b_0}{a_0}\right)$	$a_0 = J_0(z)$ $b_0 = -2m_a A_\Omega J_1(z)\,cos(\beta)$
$A_{+1} = A_\omega\sqrt{(a_{+1})^2 + (b_{+1})^2}$	$\theta_{+1} = -\,tan^{-1}\left(\frac{b_{+1}}{a_{+1}}\right)$	$a_{+1} = m_a A_\Omega J_0(z) - m_a A_\Omega J_2(z)\,cos(2\beta) + J_1(z)\,sin(\beta)$ $b_{+1} = -m_a A_\Omega J_2(z)\,sin(2\beta) - J_1(z)\,cos(\beta)$
$A_{-1} = A_\omega\sqrt{(a_{+1})^2 + (b_{+1})^2}$	$\theta_{-1} = -\,tan^{-1}\left(\frac{b_{-1}}{a_{-1}}\right)$	$a_{-1} = m_a A_\Omega J_0(z) - m_a A_\Omega J_2(z)\,cos(2\beta) - J_1(z)\,sin(\beta)$ $b_{-1} = m_a A_\Omega J_2(z)\,sin(2\beta) - J_1(z)\,cos(\beta)$

Table B.1: The amplitude and phase shift of the signal at frequencies ω and $\omega \pm \Omega$ in an AFPM model from Table 2.7, where $z = 2A_\Omega\sqrt{{m_f}^2 + {m_p}^2}$ and $\beta = tan^{-1}\left(\frac{m_f}{m_p}\right)$. ϕ_ω and ϕ_Ω set to zero for simplicity.

B.1 Relative sensitivity of the DMI

The Damage Modulation Index (DMI), introduced in Equation 2.17, is recalled in Equation B.1. Equation B.2 is obtained by substituting the amplitudes listed in Table B.1 into Equation B.1. The relative sensitivity of DMI to each MI is given in Equations B.3 to B.5. Furthermore, the total relative sensitivity of the DMI to MIs is given in Equation B.6. It is noticeable that the full expression of Equations B.4 and B.5 is not shown here, due to the large number of mathematical terms.

$$DMI(m_a, m_f, m_p) = \frac{A_{+1} + A_{-1}}{2A_0} \tag{B.1}$$

$$\begin{aligned} DMI(m_a, m_f, m_p) = &\frac{\sqrt{(m_a A_\Omega)^2 (J_0 - J_2)^2 \cos^2\beta + (m_a A_\Omega (J_0 + J_2)\sin\beta + J_1)^2}}{2\sqrt{J_0^2 + 4\,(m_a A_\Omega)^2 J_1^2 \cos^2\beta}} \\ &+ \frac{\sqrt{(m_a A_\Omega)^2 (J_0 - J_2)^2 \cos^2\beta + (m_a A_\Omega (J_0 + J_2)\sin\beta - J_1)^2}}{2\sqrt{J_0^2 + 4\,(m_a A_\Omega)^2 J_1^2 \cos^2\beta}} \end{aligned} \tag{B.2}$$

$$S_{m_a}^{DMI} = \frac{\partial DMI}{\partial m_a}\frac{m_a}{DMI} = \frac{F_1(m_a, m_f, m_p)}{G_1(m_a, m_f, m_p)} = \frac{F_{11} \times F_{12} + F_{13} \times F_{14}}{G_{11} \times G_{12} \times G_{13} \times (G_{11} + G_{12})} \tag{B.3}$$

$$\begin{aligned} F_{11}(m_a, m_f, m_p) = {} & -2m_a {J_0}^3 J_2 cos(2\beta) - 4{m_a}^2 {J_1}^3 (J_0 + J_2) sin(\beta) cos^2(\beta) \\ & -4m_a {J_1}^4 cos^2(\beta) + {J_0}^2 J_1 (J_0 + J_2) sin(\beta) + m_a {J_0}^2 ({J_0}^2 + {J_2}^2) \end{aligned}$$

$$F_{12}(m_a, m_f, m_p) = \sqrt{-2{m_a}^2 J_0 J_2 cos(2\beta) - 2m_a J_1 (J_0 + J_2) sin(\beta) + {m_a}^2 ({J_0}^2 + {J_2}^2) + {J_1}^2}$$

$$\begin{aligned} F_{13}(m_a, m_f, m_p) = {} & -2m_a {J_0}^3 J_2 cos(2\beta) + 4{m_a}^2 {J_1}^3 (J_0 + J_2) sin(\beta) cos^2(\beta) \\ & -4m_a {J_1}^4 cos^2(\beta) - {J_0}^2 J_1 (J_0 + J_2) sin(\beta) + m_a {J_0}^2 ({J_0}^2 + {J_2}^2) \end{aligned}$$

$$F_{14}(m_a, m_f, m_p) = \sqrt{-2{m_a}^2 J_0 J_2 cos(2\beta) + 2m_a J_1 (J_0 + J_2) sin(\beta) + {m_a}^2 ({J_0}^2 + {J_2}^2) + {J_1}^2}$$

$$G_{11}(m_a, m_f, m_p) = \sqrt{-2{m_a}^2 J_0 J_2 cos(2\beta) + 2m_a J_1 (J_0 + J_2) sin(\beta) + {m_a}^2 ({J_0}^2 + {J_2}^2) + {J_1}^2}$$

$$G_{12}(m_a, m_f, m_p) = \sqrt{-2{m_a}^2 J_0 J_2 cos(2\beta) - 2m_a J_1 (J_0 + J_2) sin(\beta) + {m_a}^2 ({J_0}^2 + {J_2}^2) + {J_1}^2}$$

$$G_{13}(m_a, m_f, m_p) = {J_0}^2 + 4{m_a}^2 {J_1}^2 cos^2(\beta)$$

$$S_{m_f}^{DMI} = \frac{\partial DMI}{\partial m_f}\frac{m_f}{DMI} \tag{B.4}$$

$$S_{m_p}^{DMI} = \frac{\partial DMI}{\partial m_p}\frac{m_p}{DMI} \tag{B.5}$$

$$Relative\ Sensitivity\ of\ DMI\ = \sqrt{\left(\frac{\partial DMI}{\partial m_a}\frac{m_a}{DMI}\right)^2 + \left(\frac{\partial DMI}{\partial m_f}\frac{m_f}{DMI}\right)^2 + \left(\frac{\partial DMI}{\partial m_p}\frac{m_p}{DMI}\right)^2} \tag{B.6}$$

B.2 Relative sensitivity of the Phase Shifts

The summation of the first sideband phase shifts, $\Phi(m_a, m_f, m_p)$, introduced in Equation 3.24, is recalled in Equation B.7. Equation B.8 is obtained by substituting the phase shifts listed in Table B.1 into Equation B.7. The relative sensitivity of $\Phi(m_a, m_f, m_p)$ to each MI is given in Equations B.9 to B.11. Furthermore, the total relative sensitivity of the $\Phi(m_a, m_f, m_p)$ to MIs is given in Equation B.12. It is noticeable that the full expression of Equations B.10 and B.11 is also not shown here, due to the large number of mathematical terms.

$$\Phi(m_a, m_f, m_p) = \theta_{+1} + \theta_{-1} = -\,tan^{-1}\left(\frac{b_{+1}}{a_{+1}}\right) - tan^{-1}\left(\frac{b_{-1}}{a_{-1}}\right) \tag{B.7}$$

$$\begin{aligned} \Phi(m_a, m_f, m_p) = {} & -\,tan^{-1}\left(\frac{-m_a A_\Omega J_2(z)\, sin(2\beta) - J_1(z)\, cos(\beta)}{m_a A_\Omega J_0(z) - m_a A_\Omega J_2(z)\, cos(2\beta) + J_1(z)\, sin(\beta)}\right) \\ & -\,tan^{-1}\left(\frac{m_a A_\Omega J_2(z)\, sin(2\beta) - J_1(z)\, cos(\beta)}{m_a A_\Omega J_0(z) - m_a A_\Omega J_2(z)\, cos(2\beta) - J_1(z)\, sin(\beta)}\right) \end{aligned} \tag{B.8}$$

$$S_{m_a}^{\Phi} = \frac{\partial \Phi}{\partial m_a} \frac{m_a}{\Phi} = \frac{F_2(m_a, m_f, m_p)}{G_2(m_a, m_f, m_p)} = \frac{F_2}{(G_{21} + G_{22}) \times (G_{23} + G_{24})} \tag{B.9}$$

$$\begin{aligned} F_2(m_a, m_f, m_p) = {} & 8{m_a}^3 J_0 J_1 J_2 (J_0 - J_2) cos^3(\beta) \; - 2{m_a}^3 J_1 (J_0 - J_2)(J_0 + J_2)^2 cos(\beta) \\ & -2 m_a {J_1}^3 (J_0 - J_2) cos(\beta) \end{aligned}$$

$$G_{21}(m_a, m_f, m_p) = 16{m_a}^4 {J_0}^2 {J_2}^2 cos^4(\beta) + \left({m_a}^2 (J_0 + J_2)^2 - {J_1}^2\right)^2$$

$$G_{22}(m_a, m_f, m_p) = -8{m_a}^4 J_0 J_2 (J0 + J_2)^2 cos^2(\beta) + 4{m_a}^2 {J_1}^2 ({J_0}^2 + {J_2}^2) cos^2(\beta)$$

$$G_{23}(m_a, m_f, m_p) = tan^{-1}\left(\frac{2J_2 m_a \, sin(\beta)\, cos(\beta) + J_1 \, cos(\beta)}{-2J_2 \, cos^2(\beta)\, m_a + J_1 \, sin(\beta) + m_a (J_0 + J_2)}\right)$$

$$G_{24}(m_a, m_f, m_p) = tan^{-1}\left(\frac{-2J_2 m_a \, sin(\beta)\, cos(\beta) + J_1 \, cos(\beta)}{-2J_2 \, cos^2(\beta)\, m_a - J_1 \, sin(\beta) + m_a (J_0 + J_2)}\right)$$

$$S_{m_f}^{\Phi} = \frac{\partial \Phi}{\partial m_f} \frac{m_f}{\Phi} \tag{B.10}$$

$$S_{m_p}^{\Phi} = \frac{\partial \Phi}{\partial m_p} \frac{m_p}{\Phi} \tag{B.11}$$

$$Relative\ Sensitivity\ of\ \Phi = \sqrt{\left(\frac{\partial \Phi}{\partial m_a} \frac{m_a}{\Phi}\right)^2 + \left(\frac{\partial \Phi}{\partial m_f} \frac{m_f}{\Phi}\right)^2 + \left(\frac{\partial \Phi}{\partial m_p} \frac{m_p}{\Phi}\right)^2} \tag{B.12}$$

Bibliography

1. Donskoy, D., A. Sutin, and A. Ekimov, *Nonlinear acoustic interaction on contact interfaces and its use for nondestructive testing.* NDT & E International, **2001**. *34*(4), p. 231-238. https://doi.org/10.1016/S0963-8695(00)00063-3
2. Klepka, A., W. Staszewski, R. Jenal, M. Szwedo, J. Iwaniec, and T. Uhl, *Nonlinear acoustics for fatigue crack detection – experimental investigations of vibro-acoustic wave modulations.* **2012**. *11*(2), p. 197-211. https://doi.org/10.1177/1475921711414236
3. Sutin, A. and D. Donskoy, *Vibro-acoustic modulation nondestructive evaluation technique*. Non-Destructive Evaluation Techniques for Aging Infrastructure and Manufacturing. Vol. 3397. **1998**: SPIE, https://doi.org/10.1117/12.305057
4. Zhongqing Su , L.Y., *Identification of Damage Using Lamb Waves: From Fundamentals to Applications*. Springer. **2009**, http://dx.doi.org/10.1007/978-1-84882-784-4
5. Van Den Abeele, K.E.A., Johnson, P. A., & Sutin, A., *Nonlinear elastic wave spectroscopy (NEWS) techniques to discern material damage, Part I: Nonlinear wave modulation spectroscopy (NWMS).* Research in Nondestructive Evaluation, **2001**. *12*(1), p. 17–30.
6. Salamone, S., I. Bartoli, R. Phillips, C. Nucera, and F.L. di Scalea, *Health Monitoring of Prestressing Tendons in Posttensioned Concrete Bridges.* **2011**. *2220*(1), p. 21-27. https://journals.sagepub.com/doi/abs/10.3141/2220-03
7. Dutta, D., H. Sohn, K.A. Harries, and P. Rizzo, *A Nonlinear Acoustic Technique for Crack Detection in Metallic Structures.* **2009**. *8*(3), p. 251-262. https://journals.sagepub.com/doi/abs/10.1177/1475921709102105
8. Klepka, A., L. Pieczonka, K. Dziedziech, W.J. Staszewski, F. Aymerich, and T. Uhl, *Structural Damage Detection Based on Nonlinear Acoustics: Application Examples*, in *Nonlinear Ultrasonic and Vibro-Acoustical Techniques for Nondestructive Evaluation*, T. Kundu, Editor. **2019**, Springer International Publishing: Cham. p. 139-174, https://doi.org/10.1007/978-3-319-94476-0_4
9. Broda, D., Klepka, A., Staszewski, W. J., & Scarpa, F., *Nonlinear acoustics in non-destructive testing - from theory to experimental application*, in *Key Engineering Materials.* **2014**. p. 192-201, https://doi.org/10.4028/www.scientific.net/KEM.588.192
10. Ruzzene, M., *Frequency–wavenumber domain filtering for improved damage visualization.* Smart Materials and Structures, **2007**. *16*(6), p. 2116. https://dx.doi.org/10.1088/0964-1726/16/6/014
11. Pieczonka, L., A. Klepka, A. Martowicz, and W. Staszewski, *Nonlinear vibroacoustic wave modulations for structural damage detection: an overview.* **2015**. *55 %J Optical Engineering*(1), p. 011005. https://doi.org/10.1117/1.OE.55.1.011005
12. Van Den Abeele, K.E.A., P.A. Johnson, and A. Sutin, *Nonlinear Elastic Wave Spectroscopy (NEWS) Techniques to Discern Material Damage, Part I: Nonlinear Wave Modulation Spectroscopy (NWMS).* Research in Nondestructive Evaluation, **2000**. *12*(1), p. 17-30. https://doi.org/10.1080/09349840009409646
13. Staszewski, W., *Nonlinear Acoustics for Structural Health Monitoring – Classical vs. Non-classical Approaches. 8th European Workshop on Structural Health Monitoring.* e-Journal of Nondestructive Testing, **2016**. *21*(8), https://www.ndt.net/?id=20129%20
14. Castaings, M. and B. Hosten, *Guided waves propagating in sandwich structures made of anisotropic, viscoelastic, composite materials.* The Journal of the Acoustical Society of America, **2003**. *113*(5), p. 2622-2634. https://doi.org/10.1121/1.1562913
15. Drinkwater, B.W. and P.D. Wilcox, *Ultrasonic arrays for non-destructive evaluation: A review.* NDT & E International, **2006**. *39*(7), p. 525-541. https://doi.org/10.1016/j.ndteint.2006.03.006

16. Van der Auweraer, H. and B. Peeters, *International Research Projects on Structural Health Monitoring: An Overview.* **2003**. *2*(4), p. 341-358., https://journals.sagepub.com/doi/abs/10.1177/147592103039836
17. Cuc, A., V. Giurgiutiu, S. Joshi, and Z. Tidwell, *Structural Health Monitoring with Piezoelectric Wafer Active Sensors for Space Applications.* **2007**. *45*(12), p. 2838-2850. https://arc.aiaa.org/doi/abs/10.2514/1.26141
18. Farrar, C.R. and K. Worden, *An introduction to structural health monitoring.* **2007**. *365*(1851), p. 303-315., https://royalsocietypublishing.org/doi/abs/10.1098/rsta.2006.1928
19. Sohn, H.a.F., C R and Hemez, F M and Czarnecki, J J, *A Review of Structural Health Review of Structural Health Monitoring Literature 1996-2001.* **2002** https://www.osti.gov/biblio/976152
20. Dao, P.B., A. Klepka, Ł. Pieczonka, F. Aymerich, and W.J. Staszewski, *Impact damage detection in smart composites using nonlinear acoustics – cointegration analysis for removal of undesired load effect.* Smart Materials and Structures, **2017**. *26*(3), p. 035012. https://dx.doi.org/10.1088/1361-665X/aa5744
21. Blanloeuil, P., A. Meziane, and C. Bacon, *Nonlinear interaction of ultrasonic waves with a crack of different orientations.* AIP Conference Proceedings, **2013**. *1511*(1), p. 99-106. https://doi.org/10.1063/1.4789036
22. Tian, Y. and Y. Shen. *Improved Nonlinear Ultrasonic Guided Wave Damage Detection Using a Bandgap Meta-Surface*. in *ASME 2018 International Mechanical Engineering Congress and Exposition*. 2018.
23. Jiao, J., Drinkwater, B., & Neild, S., *Contact defect detection in plates using guided wave and vibro-acoustic modulation.* 17th World Conference on Nondestructive Testing (WCNDT 2008), **2008**. 13(11), https://www.ndt.net/?id=6415
24. Donskoy, D. and D. Liu, *Vibro-acoustic modulation baseline-free non-destructive testing.* Journal of Sound and Vibration, **2021**. *492*p. 115808. https://doi.org/10.1016/j.jsv.2020.115808
25. Loi, G., F. Aymerich, and M.C. Porcu, *Influence of Sensor Position and Low-Frequency Modal Shape on the Sensitivity of Vibro-Acoustic Modulation for Impact Damage Detection in Composite Materials.* **2022**. *6*(7), p. 190. https://www.mdpi.com/2504-477X/6/7/190
26. Yang, D., K. Wang, J. Zhang, Y. Yuan, Y. Liu, and F.T.K. Au, *Micro-crack localization for steel strands using nonlinear vibro-acoustic modulation based on modified signal bispectrum analysis.* Measurement, **2024**. *233*p. 114746. https://doi.org/10.1016/j.measurement.2024.114746
27. Zaitsev, V., V. Nazarov, V. Gusev, and B. Castagnede, *Novel nonlinear-modulation acoustic technique for crack detection.* NDT & E International, **2006**. *39*(3), p. 184-194. https://doi.org/10.1016/j.ndteint.2005.07.007
28. Duffour, P., M. Morbidini, and P. Cawley, *A study of the vibro-acoustic modulation technique for the detection of cracks in metals.* The Journal of the Acoustical Society of America, **2006**. *119*(3), p. 1463-1475. https://doi.org/10.1121/1.2161429
29. Zaitsev, V.Y., L.A. Matveev, and A.L. Matveyev, *On the ultimate sensitivity of nonlinear-modulation method of crack detection.* NDT & E International, **2009**. *42*(7), p. 622-629. https://doi.org/10.1016/j.ndteint.2009.05.001
30. Donskoy, D.M., *Nonlinear Acoustic Methods*, in *Encyclopedia of Structural Health Monitoring*. **2009**, https://doi.org/10.1002/9780470061626.shm014
31. Aymerich, F. and W.J. Staszewski, *Experimental Study of Impact-Damage Detection in Composite Laminates using a Cross-Modulation Vibro-Acoustic Technique.* **2010**. *9*(6), p. 541-553. https://journals.sagepub.com/doi/abs/10.1177/1475921710365433
32. Hu, H.F., W.J. Staszewski, N.Q. Hu, R.B. Jenal, and G.J. Qin, *Crack detection using nonlinear acoustics and piezoceramic transducers – instantaneous amplitude and frequency*

analysis. Smart Materials and Structures, **2010**. *19*(6), p. 065017. https://dx.doi.org/10.1088/0964-1726/19/6/065017

33. A. Klepkal, F.A., W.J. Staszewski and T. Uhl, *Nonlinear vibro-acoustic wave modulations for impact damage detection in composites.* 15th European Conference on Composite Materials, **2012**,
34. Klepka, A., W.J. Staszewski, K. Dziedziech, and F. Aymerich, *Non-Linear Vibro-Acoustic Wave Modulations - Analysis of Different Types of Low-Frequency Excitation.* Key Engineering Materials, **2013**. *569-570*p. 924-931. https://www.scientific.net/KEM.569-570.924
35. Klepka, A., L. Pieczonka, W.J. Staszewski, and F. Aymerich, *Impact damage detection in laminated composites by non-linear vibro-acoustic wave modulations.* Composites Part B: Engineering, **2014**. *65*p. 99-108. https://doi.org/10.1016/j.compositesb.2013.11.003
36. Hong, M., Z. Su, Q. Wang, L. Cheng, and X. Qing, *Modeling nonlinearities of ultrasonic waves for fatigue damage characterization: Theory, simulation, and experimental validation.* Ultrasonics, **2014**. *54*(3), p. 770-778. https://doi.org/10.1016/j.ultras.2013.09.023
37. Lim, H.J. and H. Sohn, *Necessary Conditions for Nonlinear Ultrasonic Modulation Generation Given a Localized Fatigue Crack in a Plate-Like Structure.* **2017**. *10*(3), p. 248. https://www.mdpi.com/1996-1944/10/3/248
38. Donskoy, D., B. Golchinfar, M. Ramezani, M. Rutner, and S. Hassiotis, *Vibro-acoustic amplitude and frequency modulations during fatigue damage evolution.* AIP Conference Proceedings, **2019**. *2102*(1), https://doi.org/10.1063/1.5099754
39. Donskoy, D.M. and M. Ramezani, *Separation of amplitude and frequency modulations in Vibro-Acoustic Modulation Nondestructive Testing Method.* Proceedings of Meetings on Acoustics, **2018**. *34*(1), https://doi.org/10.1121/2.0000831
40. Klepka, A., K. Dziedziech, J. Mrówka, and J. Górski, *Experimental investigation of modulation effects for contact-type interfaces in vibro-acoustic modulation tests.* **2021**. *20*(3), p. 917-930. https://journals.sagepub.com/doi/abs/10.1177/1475921719857624
41. Oppermann, P., L. Dorendorf, M. Rutner, and C. Renner, *Nonlinear modulation with low-power sensor networks using undersampling.* **2021**. *20*(6), p. 3252-3264. https://journals.sagepub.com/doi/abs/10.1177/1475921720982885
42. Zhan, Z., F. Wang, Y. Zheng, Z. Wang, S. Huang, X. Li, and S. Wang, *Nonlinear Responds of Lamb Waves in Plate Structure with Micro-Crack Using Frequency-Mixing Technique.* Journal of Physics: Conference Series, **2021**. *1877*(1), p. 012014. https://dx.doi.org/10.1088/1742-6596/1877/1/012014
43. Michaels, J., *Effectiveness of in situ damage localization methods using sparse ultrasonic sensor arrays*. SPIE Smart Structures and Materials + Nondestructive Evaluation and Health Monitoring. Vol. 6935. **2008**: SPIE, https://doi.org/10.1117/12.775788
44. Michaels, J.E., *Detection, localization and characterization of damage in plates with an in situ array of spatially distributed ultrasonic sensors.* Smart Materials and Structures, **2008**. *17*(3), p. 035035. https://dx.doi.org/10.1088/0964-1726/17/3/035035
45. Michaels, J. and T. Michaels, *An integrated strategy for detection and imaging of damage using a spatially distributed array of piezoelectric sensors*. SPIE Smart Structures and Materials + Nondestructive Evaluation and Health Monitoring. Vol. 6532. **2007**: SPIE, https://doi.org/10.1117/12.715438
46. Liu, L. and F.G. Yuan, *Active damage localization for plate-like structures using wireless sensors and a distributed algorithm.* Smart Materials and Structures, **2008**. *17*(5), p. 055022. https://dx.doi.org/10.1088/0964-1726/17/5/055022
47. Ng, C.T. and M. Veidt, *A Lamb-wave-based technique for damage detection in composite laminates.* Smart Materials and Structures, **2009**. *18*(7), p. 074006. https://dx.doi.org/10.1088/0964-1726/18/7/074006

48. Clarke, T. and P. Cawley, *Enhancing the defect localization capability of a guided wave SHM system applied to a complex structure.* **2011**. *10*(3), p. 247-259. https://journals.sagepub.com/doi/abs/10.1177/1475921710373294
49. Michaels, J., S.J. Lee, J. Hall, and T. Michaels, *Multi-mode and multi-frequency guided wave imaging via chirp excitations*. SPIE Smart Structures and Materials + Nondestructive Evaluation and Health Monitoring. Vol. 7984. **2011**: SPIE, https://doi.org/10.1117/12.880963
50. He, J., X. Guan, T. Peng, Y. Liu, A. Saxena, J. Celaya, and K. Goebel, *A multi-feature integration method for fatigue crack detection and crack length estimation in riveted lap joints using Lamb waves.* Smart Materials and Structures, **2013**. *22*(10), p. 105007. https://dx.doi.org/10.1088/0964-1726/22/10/105007
51. Yan, G., *A Bayesian approach for damage localization in plate-like structures using Lamb waves.* Smart Materials and Structures, **2013**. *22*(3), p. 035012. https://dx.doi.org/10.1088/0964-1726/22/3/035012
52. Lu, G., Y. Li, T. Wang, H. Xiao, L. Huo, and G. Song, *A multi-delay-and-sum imaging algorithm for damage detection using piezoceramic transducers.* **2017**. *28*(9), p. 1150-1159. https://journals.sagepub.com/doi/abs/10.1177/1045389X16666184
53. Ebrahimkhanlou, A., B. Dubuc, and S. Salamone, *Damage localization in metallic plate structures using edge-reflected lamb waves.* Smart Materials and Structures, **2016**. *25*(8), p. 085035. https://dx.doi.org/10.1088/0964-1726/25/8/085035
54. Yogesh S. Andhale, F.A.M., Nitesh Yelve, *Localization of Damages in Plain And Riveted Aluminium Specimens using Lamb Waves.* International Journal of Acoustics and Vibration, **2019**. *24*https://doi.org/10.20855/ijav.2019.24.11485
55. Hameed, M.S., Z. Li, J. Chen, and J. Qi, *Lamb-Wave-Based Multistage Damage Detection Method Using an Active PZT Sensor Network for Large Structures.* **2019**. *19*(9), p. 2010. https://www.mdpi.com/1424-8220/19/9/2010
56. Mu, W., J. Sun, G. Liu, and S. Wang, *High-Resolution Crack Localization Approach Based on Diffraction Wave.* **2019**. *19*(8), p. 1951. https://www.mdpi.com/1424-8220/19/8/1951
57. Su, C., M. Jiang, J. Liang, A. Tian, L. Sun, L. Zhang, F. Zhang, and Q. Sui, *Damage Localization of Composites Based on Difference Signal and Lamb Wave Tomography*, in *Materials*. 2020, https://doi.org/10.3390/ma13010218
58. Deng, F. and H. Chen, *A Defects Localization Algorithm Based on the Lamb Wave of Plate Structure.* Journal of Nondestructive Evaluation, Diagnostics and Prognostics of Engineering Systems, **2020**. *4*(2), https://doi.org/10.1115/1.4048379
59. Wang, Z., S. Huang, S. Wang, Q. Wang, and W. Zhao, *A Damage Localization Method With Multimodal Lamb Wave Based on Adaptive Polynomial Chirplet Transform.* IEEE Transactions on Instrumentation and Measurement, **2020**. *69*(10), p. 8076-8087. http://dx.doi.org/10.1109/TIM.2020.2993342
60. Chen, H., Z. Liu, Y. Gong, B. Wu, and C. He, *Evolutionary Strategy-Based Location Algorithm for High-Resolution Lamb Wave Defect Detection With Sparse Array.* IEEE Transactions on Ultrasonics, Ferroelectrics, and Frequency Control, **2021**. *68*(6), p. 2277-2293. http://dx.doi.org/10.1109/TUFFC.2021.3060094
61. Yan, G., L. Zhou, and F.G. Yuan, *Wavelet-based built-in damage detection and identification for composites*. SPIE Smart Structures and Materials + Nondestructive Evaluation and Health Monitoring. Vol. 5765. **2005**: SPIE, https://doi.org/10.1117/12.602435
62. Shan, S., J. Qiu, C. Zhang, H. Ji, and L. Cheng, *Multi-damage localization on large complex structures through an extended delay-and-sum based method.* **2016**. *15*(1), p. 50-64. https://journals.sagepub.com/doi/abs/10.1177/1475921715623358

63. Qiang, W. and Y. Shenfang, *Baseline-free Imaging Method based on New PZT Sensor Arrangements.* **2009**. *20*(14), p. 1663-1673. https://journals.sagepub.com/doi/abs/10.1177/1045389X09105232
64. Quaegebeur, N., P. Masson, D. Langlois-Demers, and P. Micheau, *Dispersion-based imaging for structural health monitoring using sparse and compact arrays.* Smart Materials and Structures, **2011**. *20*(2), p. 025005. https://dx.doi.org/10.1088/0964-1726/20/2/025005
65. Bagheri, A., K. Li, and P. Rizzo, *Reference-free damage detection by means of wavelet transform and empirical mode decomposition applied to Lamb waves.* **2013**. *24*(2), p. 194-208. http://dx.doi.org/10.1177/1045389x12460433
66. Lee, S.J., N. Gandhi, J.S. Hall, J.E. Michaels, B. Xu, T.E. Michaels, and M. Ruzzene, *Baseline-free guided wave imaging via adaptive source removal.* **2012**. *11*(4), p. 472-481. https://journals.sagepub.com/doi/abs/10.1177/1475921711435536
67. Wang, X., J. Cai, and Z. Zhou, *A Lamb wave signal reconstruction method for high-resolution damage imaging.* Chinese Journal of Aeronautics, **2019**. *32*(5), p. 1087-1099. https://doi.org/10.1016/j.cja.2019.03.001
68. Kannusamy, M., S. Kapuria, and S. Sasmal, *Accurate baseline-free damage localization in plates using refined Lamb wave time-reversal method.* Smart Materials and Structures, **2020**. *29*(5), p. 055044. http://dx.doi.org/10.1088/1361-665X/ab8028
69. Li, Z., Z. Wang, L. Xiao, and W. Qu, *Damage detection and locating using tone burst and continuous excitation modulation method*. SPIE Smart Structures and Materials + Nondestructive Evaluation and Health Monitoring. Vol. 9064. **2014**: SPIE, https://doi.org/10.1117/12.2044998
70. Pieczonka, L., L. Zietek, A. Klepka, W.J. Staszewski, F. Aymerich, and T. Uhl, *Damage imaging in composites using nonlinear vibro-acoustic wave modulations.* **2018**. *25*(2), p. e2063. https://doi.org/10.1002/stc.2063
71. Xiao, C., H. Zheng, L. Hu, Y. Wang, and Y. Cao, *Study of micro-crack localization based on vibro-acoustic modulation.* Journal of Physics: Conference Series, **2018**. *1074*(1), p. 012069. https://dx.doi.org/10.1088/1742-6596/1074/1/012069
72. Aslam, M.B., C.R.; Nagarajan, P.; Remanan, *Numerical and Experimental Investigation of Nonlinear Lamb Wave Mixing at Low Frequency.* Journal of Aerospace Engineering, **2020**. *33*(4), https://doi.org/10.1061/(ASCE)AS.1943-5525.0001146
73. Karve, P. and S. Mahadevan, *On the performance of vibro-acoustic-modulation-based diagnosis of breathing cracks in thick, elastic slabs.* **2020**. *27*(3), p. e2470. https://doi.org/10.1002/stc.2470
74. Aslam, M., P. Nagarajan, and M. Remanan, *Defect Localization Using Nonlinear Lamb Wave Mixing Technique.* Journal of Nondestructive Evaluation, **2021**. *40*(1), p. 16. https://doi.org/10.1007/s10921-020-00747-5
75. Wang, J.-S., C.-B. Xu, Y.-X. Zhao, N. Hu, and M.-X. Deng, *Microcrack localization using a collinear Lamb wave frequency-mixing technique in a thin plate.* Chinese Physics B, **2022**. *31*(1), p. 014301. http://dx.doi.org/10.1088/1674-1056/ac0da8
76. Miele, S., P.M. Karve, S. Mahadevan, and V. Agarwal, *Diagnosis of internal cracks in concrete using vibro-acoustic modulation and machine learning.* **2022**. *21*(5), p. 1973-1991. https://journals.sagepub.com/doi/abs/10.1177/14759217211047901
77. Lamb, H., *On waves in an elastic plate.* **1917**. *93*(648), p. 114-128. https://royalsocietypublishing.org/doi/abs/10.1098/rspa.1917.0008
78. Rose, J.L., *Ultrasonic Guided Waves in Solid Media*. **2014**, Cambridge: Cambridge University Press, http://dx.doi.org/10.1017/CBO9781107273610
79. Wilcox, P., M. Lowe, and P. Cawley, *The effect of dispersion on long-range inspection using ultrasonic guided waves.* NDT & E International, **2001**. *34*(1), p. 1-9. https://doi.org/10.1016/S0963-8695(00)00024-4

80. Wilcox, P.D., M.J.S. Lowe, and P. Cawley, *Mode and Transducer Selection for Long Range Lamb Wave Inspection.* **2001**. *12*(8), p. 553-565. https://journals.sagepub.com/doi/abs/10.1177/10453890122145348
81. Giurgiutiu, V., *Structural health monitoring with piezoelectric wafer active sensors – predictive modeling and simulation.*, INCAS Bulletin, **2010**. 2(3), http://dx.doi.org/10.13111/2066-8201.2010.2.3.4
82. Su, Z., L. Ye, and Y. Lu, *Guided Lamb waves for identification of damage in composite structures: A review.* Journal of Sound and Vibration, **2006**. *295*(3), p. 753-780. https://doi.org/10.1016/j.jsv.2006.01.020
83. Zhongqing Su , L.Y., *Identification of Damage Using Lamb Waves*. **2009**: Springer, http://dx.doi.org/10.1007/978-1-84882-784-4
84. Alleyne, D.N. and P. Cawley, *The interaction of Lamb waves with defects.* IEEE Transactions on Ultrasonics, Ferroelectrics, and Frequency Control, **1992**. *39*(3), p. 381-397. http://dx.doi.org/10.1109/58.143172
85. Li, L. and P. Fromme, *Mode conversion of fundamental guided ultrasonic wave modes at part-thickness crack-like defects.* Ultrasonics, **2024**. *142*p. 107399. https://doi.org/10.1016/j.ultras.2024.107399
86. Li, F., Y. Zhao, P. Cao, and N. Hu, *Mixing of ultrasonic Lamb waves in thin plates with quadratic nonlinearity.* Ultrasonics, **2018**. *87*p. 33-43. https://doi.org/10.1016/j.ultras.2018.02.005
87. Banerjee, S., F. Ricci, and A. Mal. *A vibration and wave propagation based methodology for near real-time damage monitoring of composite structures*. in *ASME international mechanical engineering congress and exposition*. 2007.
88. Grahn, T., *Lamb wave scattering from a circular partly through-thickness hole in a plate.* Wave Motion, **2003**. *37*(1), p. 63-80. https://doi.org/10.1016/S0165-2125(02)00051-3
89. Sedaghati, A., F. Honarvar, M. Tabatabaeipour, and A.N. Sinclair, *Investigation of the scattering of Lamb waves from a generalized circular cavity by using Poisson/Mindlin plate theories and numerical simulation.* **2020**. *234*(1), p. 152-170. https://journals.sagepub.com/doi/abs/10.1177/0954406219871073
90. Cesnik, A.C.R.E.S.C.E.S., *Review of Guided-Wave Structural Health Monitoring.* The Shock and Vibration Digest, **2007**. *39*(2), p. 91-114. http://dx.doi.org/10.1177/0583102406075428
91. Michaels, T.E., J.E. Michaels, and M. Ruzzene, *Frequency–wavenumber domain analysis of guided wavefields.* Ultrasonics, **2011**. *51*(4), p. 452-466. https://doi.org/10.1016/j.ultras.2010.11.011
92. Michaels, J.E. and T.E. Michaels, *Detection of structural damage from the local temporal coherence of diffuse ultrasonic signals.* IEEE Transactions on Ultrasonics, Ferroelectrics, and Frequency Control, **2005**. *52*(10), p. 1769-1782. https://doi.org/10.1109/TUFFC.2005.1561631
93. Klepka, A., & Dziedziech, K., *Vibro-acoustic modulation for damage detection -investigation of nonlinear effects for contact-type damage.* International NDT Conference & Exhibition, **2025**, https://doi.org/10.58286/30805
94. Donskoy, D.M. and A.M. Sutin, *Vibro-Acoustic Modulation Nondestructive Evaluation Technique.* **1998**. *9*(9), p. 765-771. https://journals.sagepub.com/doi/abs/10.1177/1045389X9800900909
95. Singh, A.K., B. Chen, V.B.C. Tan, T.E. Tay, and H.P. Lee, *A theoretical and numerical study on the mechanics of vibro-acoustic modulation.* The Journal of the Acoustical Society of America, **2017**. *141*(4), p. 2821-2831. 10.1121/1.4981133 %J The Journal of the Acoustical Society of America
96. Dorendorf, L., N. Lalkovski, and M. Rutner, *Physical explanation for vibro-acoustic modulation due to local and global nonlinearities in a structure and its experimental and*

numerical validation. Journal of Sound and Vibration, **2022**. *528*p. 116885. https://doi.org/10.1016/j.jsv.2022.116885

97. Klepka, A., K. Dziedziech, Ł. Pieczonka, M. Adamczyk, and W.J. Staszewski, *Experimental investigations of contact-type damage nonlinearity.* Journal of Physics: Conference Series, **2017**. *842*(1), p. 012054. https://dx.doi.org/10.1088/1742-6596/842/1/012054
98. Jhang, K.-Y., *Nonlinear ultrasonic techniques for nondestructive assessment of micro damage in material: A review.* International Journal of Precision Engineering and Manufacturing, **2009**. *10*(1), p. 123-135. https://doi.org/10.1007/s12541-009-0019-y
99. Lissenden, C.J., *Nonlinear ultrasonic guided waves—Principles for nondestructive evaluation.* Journal of Applied Physics, **2021**. *129*(2), https://doi.org/10.1063/5.0038340
100. Haykin, *Communication Systems, 4th Edition*. **2006**: Wiley India Pvt. Limited,
101. Lathi, B.P. and Z. Ding, *Modern Digital and Analog Communication Systems*. **2010**,
102. Qiu, J., F. Li, S. Abbas, and Y. Zhu, *A baseline-free damage detection approach based on distance compensation of guided waves.* **2019**. *38*(3-4), p. 1132-1148. https://journals.sagepub.com/doi/abs/10.1177/1461348418813699
103. Lee, Y.F. and Y. Lu, *Identification of fatigue crack under vibration by nonlinear guided waves.* Mechanical Systems and Signal Processing, **2022**. *163*p. 108138. https://doi.org/10.1016/j.ymssp.2021.108138
104. Broda, D., K. Mendrok, V.V. Silberschmidt, L. Pieczonka, and W.J. Staszewski, *The Study of Localized Crack-Induced Effects of Nonlinear Vibro-Acoustic Modulation.* **2023**. *16*(4), p. 1653. https://www.mdpi.com/1996-1944/16/4/1653
105. Van Den Abeele, K.E.A., A. Sutin, J. Carmeliet, and P.A. Johnson, *Micro-damage diagnostics using nonlinear elastic wave spectroscopy (NEWS).* NDT & E International, **2001**. *34*(4), p. 239-248. https://doi.org/10.1016/S0963-8695(00)00064-5
106. Matlack, K.H., J.Y. Kim, L.J. Jacobs, and J. Qu, *Review of Second Harmonic Generation Measurement Techniques for Material State Determination in Metals.* Journal of Nondestructive Evaluation, **2014**. *34*(1), p. 273. https://doi.org/10.1007/s10921-014-0273-5
107. Donskoy, D., A. Zagrai, A. Chudnovsky, E. Golovin, and V. Agarwala, *Nonlinear vibro-acoustic modulation technique for life prediction of aging aircraft components.* Proceedings of the 3rd European Workshop - Structural Health Monitoring 2006, **2006** p. 251-258.
108. Oppenheim, A.V., A.S. Willsky, and S.H. Nawab, *Signals & systems (2nd ed.)*. **1996**: Prentice-Hall, Inc.,
109. Huang, N.E., Z. Shen, S.R. Long, M.C. Wu, H.H. Shih, Q. Zheng, N.-C. Yen, C.C. Tung, and H.H. Liu, *The empirical mode decomposition and the Hilbert spectrum for nonlinear and non-stationary time series analysis.* **1998**. *454*(1971), p. 903-995. https://royalsocietypublishing.org/doi/abs/10.1098/rspa.1998.0193
110. Croxford, A., P. Wilcox, and B. Drinkwater, *Guided wave SHM with a distributed sensor network*. SPIE Smart Structures and Materials + Nondestructive Evaluation and Health Monitoring. Vol. 6935. **2008**: SPIE, https://doi.org/10.1117/12.776355
111. Perrot, V., M. Polichetti, F. Varray, and D. Garcia, *So you think you can DAS? A viewpoint on delay-and-sum beamforming.* Ultrasonics, **2021**. *111*p. 106309. https://doi.org/10.1016/j.ultras.2020.106309
112. Boashash, B., *Time Frequency Analysis and Processing*. **2015**: Elsevier,
113. Oppenheim, A. and R. Schafer, *Discrete-Time Signal Processing, 3rd Edition*. **2014**: Pearson India,
114. Sharif-Khodaei, Z. and M.H. Aliabadi, *Assessment of delay-and-sum algorithms for damage detection in aluminium and composite plates.* Smart Materials and Structures, **2014**. *23*(7), p. 075007. https://dx.doi.org/10.1088/0964-1726/23/7/075007